

ABSTRACT

Title of dissertation: INTERLAYER INTERACTION PHENOMENA
IN NOVEL MATERIALS

Sergii Pershoguba, Doctor of Philosophy, 2014

Dissertation directed by: Professor Victor Yakovenko
Department of physics

Recently, there has been a considerable interest in various novel two-dimensional (2D) materials, such as graphene, topological insulators, etc. These materials host a plethora of exotic phenomena owing to their unconventional electronic structure. Physics of these 2D materials is understood fairly well, so a natural generalization is to assemble these materials into three-dimensional (3D) stacks. In this thesis, we study a number of multilayer systems, where the interlayer interaction plays a salient role.

We commence with studying graphene multilayers coupled via interlayer tunneling amplitude. We calculate the energy spectrum of the system in magnetic field B parallel to the layers. The parallel magnetic field leads to a relative gauge shift of the momentum spaces of the individual 2D layers. When the interlayer tunneling is introduced, we find the Landau levels. We observe two qualitatively distinct domains in the Landau spectrum and analyze them using semiclassical arguments. Then, we include electric field E perpendicular to the layers, and analyze the spectrum in the crossed-field geometry. If the fields are in resonance $E = vB$, where v

is the velocity of carriers in graphene, the wave-functions delocalize in the direction along the field E . We compare this prediction to a tunneling spectroscopy study of a graphite mesa in the parallel magnetic field. Indeed, the tunneling spectrum displays a peak, which grows linearly with the applied magnetic field B , and is, thus, consistent with our theoretical analysis.

Then, we move on to a discussion of Z_2 topological insulators within the Shockley model. We generalize the one dimensional (1D) Shockley model by replacing atomic sites of the original model by the 2D Rashba spin-orbit layers. We analyze surface states of a topological insulator using a construction of vortex lines in the 3D momentum space. We also study a topological insulator in a thin film geometry, where the opposite surface states are coupled by the tunneling amplitude. We calculate the tunneling current between the opposite surfaces and a spin polarization of the current as a function of the in-plane magnetic field.

We conclude with studying a novel chiral order in cuprates. We construct a helical interlayer pattern of loop-currents. The interlayer magnetic coupling and magnetoelectric effect lead to optical gyrotropy.

INTERLAYER INTERACTION PHENOMENA
IN NOVEL MATERIALS

by

Sergii Pershoguba

Dissertation submitted to the Faculty of the Graduate School of the
University of Maryland, College Park in partial fulfillment
of the requirements for the degree of
Doctor of Philosophy
2014

Advisory Committee:
Professor Victor M. Yakovenko, Chair/Advisor
Professor Sankar Das Sarma
Professor Victor Galitski
Assistant Professor Jay Deep Sau
Professor Christopher Jarzynski

© Copyright by
Sergii Pershoguba
2014

Acknowledgments

It seems, I arrived to Maryland only yesterday, or was it five years ago? It is hard to believe that time passed so fast. Is there some bizarre time acceleration phenomenon not explained by Einstein? In any case, graduate school was a very rewarding and tough, at times, experience for me: tough - because you fail a lot until you find something valuable in science, rewarding - for multiple reasons. They are the freedom to do something new every day, opportunity to learn the hottest science and grow personally, the ability to interact with brilliant people.

I think, finding a research advisor is very similar to the Schrodinger's cat experiment: you never know until you work with a person. My "measurement" was great. I worked with Professor Victor Yakovenko. I think, not many advisors spend the amount of time on their graduate students that Victor spent on me. I am indebted to Victor for directing this PhD work and being a great teacher, for engaging discussions about science and writing lessons (the results of which, I hope, propagated into this thesis). I am grateful to Professor Sankar Das Sarma for the opportunity to be a member of CMTC¹, advising me on several occasions and a wonderful coffee machine. I thank Professor Victor Galitski for advising me over the years and sharing his ideas on exotic physics at the group meetings. I would like to thank Professor Leonid Alexandrovich Falkovsky from the Landau Institute and Dr. Yuriy Victorovich Skrypnyk from the Kiev Institute for Metal Physics, with who I did my first works in condensed matter physics. I am grateful to Evgeniy Petrovich Stepko, my high school physics teacher, who always supported and cheered for me.

¹I would like to acknowledge funding from CMTC and CNAM over years at Maryland.

I would like to thank students and postdocs at Maryland: Kostya Kechedzhi, Aydin Keser, Joe Mitchell, Juraj Radić. I am honored to call them my friends and colleagues, and I hope to stay in touch. I would like to thank Dmytro Kashyn and Serge Novikov, who were my roommates and good friends over the years. Separate gratitude goes to my friend Alexey Vedernikov, the most selfless person I know. Thanks for organizing multiple skiing and camping trips! I hope to hang out more often with my PhysTech friends: Pavel Afanasyev, Vladimir Bulatov, Olga Dvoret-skaya, Tim Khodkov, Dmytro Korenkevich, Greg Polshyn.

I would like to express my deep appreciation to my family: Mom, Dad (who would be very proud if I got PhD), and my Sister. I always felt your love and support, and it always helped me.

As I am preparing to leave, I think, I am finally becoming a terp. I shall miss you Maryland!

Sergey Pershoguba, May 2014

Table of Contents

List of Figures	vii
List of Abbreviations	xiv
1 Introduction	1
1.1 Certain low-dimensional models	1
1.1.1 One dimension. Shockley model	1
1.1.2 Two dimensions	4
1.1.2.1 Graphene	5
1.1.2.2 Topological Insulators	7
1.2 In current thesis: multilayer structure of novel 2D materials	11
1.2.1 Graphene multilayer in a parallel magnetic field	12
1.2.2 Graphene multilayer in crossed electric and magnetic fields . .	13
1.2.3 Shockley edge states in topological insulators	14
1.2.4 Thin film of a topological insulator in a parallel magnetic field	15
1.2.5 Chiral structure in the pseudogap phase of cuprates	16
2 Graphene multilayer in a parallel magnetic field	18
2.1 Introduction	18
2.2 Graphene bilayer	20
2.2.1 Model	20
2.2.2 Parallel magnetic field	22
2.3 Graphite	26
2.3.1 Model	26
2.3.2 Parallel magnetic field	27
2.3.2.1 Semiclassical analysis	27
2.3.2.2 Mathieu equation	30
2.3.2.3 Closed orbits	34
2.3.2.4 Open orbits	39
2.4 Conclusions	43

3	Graphene multilayer in crossed electric and magnetic fields	45
3.1	Introduction	45
3.2	Hamiltonian and energy spectrum	46
3.2.1	Hamiltonian	46
3.2.2	Weak coupling limit	47
3.2.3	Exact diagonalization	49
3.3	Experiment and interpretation	51
3.3.1	Experimental results	51
3.3.2	Discussion	52
3.4	Conclusion	54
4	Shockley edge states in topological insulators	55
4.1	Introduction	55
4.2	1D Shockley model	57
4.2.1	The original Shockley model	57
4.2.2	On-site energies in the 1D Shockley model	64
4.3	3D Shockley-like model	66
4.3.1	Generalization to the 3D case	66
4.3.2	Spin-orbit interaction	68
4.3.3	Vortex lines in 3D momentum space	71
4.4	Diamond Model	73
4.4.1	Hamiltonian and surface states	73
4.4.2	3D vortex lines	80
4.5	Shockley model description of Bi_2Se_3	84
4.5.1	General analysis	84
4.5.2	Continuous approximation	87
4.5.2.1	First-order expansion	87
4.5.2.2	Higher-order expansion	89
4.6	Generalized Shockley model	93
4.6.1	Additional tight binding amplitude t_3	93
4.6.2	Arbitrary periodic function $t(k)$	100
4.7	Symmetries	101
4.8	Conclusions	103
5	Thin film of a topological insulator in a parallel magnetic field	105
5.1	Introduction.	105
5.2	Model.	106
5.3	Spectrum in a parallel field.	109
5.4	Tunneling current in a parallel field.	111
5.5	Experimental relevance.	116
5.6	Conclusions.	118

6	Chiral structure in the pseudogap phase of cuprates	120
6.1	Introduction.	120
6.2	Helical order of the anapole moments.	122
6.3	Electrodynamics of gyrotropic media	124
6.4	Magnetoelectric effect in a single CuO_2 plane.	125
6.5	Interlayer coupling and the gyrotropic term.	127
6.6	Experimental relevance.	131
6.7	Conclusion.	132
A	Appendix	134
A.1	Edge states in the original Shockley model	134
A.2	Energy of the edge states in the generalized Shockley model	137
A.3	Tight-binding model of Varma's loop-current order	139
	List of Publications	146
	List of Presentations	147
	Bibliography	149

List of Figures

1.1	(a) One dimensional Shockley model is shown in the bottom. Localized Shockley wave function (1.3) is shown in the top. (b) The continuous approximation of the Shockley model - the Jackiw-Rebbi model (1.4). Continuous function $m(x)$ (shown in blue) models a domain wall. There is a non-trivial eigenstate (1.5) (shown in red) localized in the vicinity of the domain wall.	2
1.2	The number of papers published in Physical Review B and Physical Review Letters containing key words (a) “graphene” and (b) “topological insulator” in the title or abstract during 2004-2013.	4
1.3	(a) Honeycomb lattice of graphene with A (blue) and B (red) sublattices. Projection of the lattice onto the horizontal axis generates monoatomic lattice, and onto the vertical axis - the bipartite Shockley lattice. (b) The energy spectrum of graphene. The dashed line denotes a boundary of the Brillouin zone.	6
1.4	(a) Tight-binding lattice of the Haldane model. (b) Energy spectrum corresponding to pure graphene $t_1 = M = 0$. For reference, the labels K and K' represent the same points in the momentum space as in Fig. 1.3(b). (c) Energy spectrum corresponding to the trivial topological phase $t_1 = 0$, $M = 0.5t$. (d) Energy spectrum corresponding to the non-trivial phase $t_1 = 0.5t$, $M = 0$, $\phi = \pi/2$. In panels (b)-(d), the red curves were obtained in a ribbon geometry with 30 atoms in the y direction and infinite number of atoms in the x direction. The black curves were obtained from the bulk spectrum (1.9). So, the red line not covered by the black line partner corresponds to an edge mode.	8
1.5	A pair of Bernal-stacked graphene layers in the parallel magnetic field \mathbf{B} applied along the y direction. Variables t and t_1 denote the electron intra and interlayer tunneling amplitudes.	13
1.6	Illustration of the 3D Shockley model. The arrows show the staggered direction of the Rashba vector (for a detailed discussion see Section 4.3.	14

1.7	Thin film of a topological insulator of thickness d in a parallel magnetic field B_y . The surface states ψ_1 and ψ_2 shown in red and blue overlap where the thickness d is comparable with the decay length ξ of the surface state.	16
1.8	(a) Loop-current order in a CuO_2 plane has an anapole moment \mathbf{N} . (b) Chiral order on a series of parallel CuO_2 planes is constructed by rotating vector \mathbf{N} from one layer to another.	17
2.1	A pair of Bernal-stacked graphene layers in the parallel magnetic field \mathbf{B} applied along the y direction. t and t_1 are the electron tunneling amplitudes.	20
2.2	(a) The electron spectrum (2.4) of a graphene bilayer in zero magnetic field. (b) The spectrum (2.12) in a nonzero parallel magnetic field. The magnetic field splits the parabolic spectrum into the two Dirac cones. An exaggerated value $q = 5$ of the magnetic field parameter was utilized here.	22
2.3	Spectrum $\varepsilon_1(\mathbf{p}, k)$ (2.19) of Hamiltonian (2.18) for $p_y = 0$. Each curve corresponds to a given value of the out-of-plane momentum k indicated on the right. The axes are given in the adopted dimensionless units (2.9).	28
2.4	Semiclassical electron orbits in the momentum space for the in-plane magnetic field along the y axis. Only the orbits with $p_y = 0$ are shown. They are obtained by intersecting the (p_x, k) plane with the isoenergetic surfaces $\varepsilon_1(\mathbf{p}, k) = \varepsilon$ for (a) $\varepsilon = 0.1$, (b) $\varepsilon = 2$, (c) $\varepsilon = 2.2$. The orbits are (a) closed for $ \varepsilon < 2$ and (c) open for $ \varepsilon > 2$	29
2.5	Domains of the continuous and discrete spectra in the (p_y, ε) plane. The dashed-dotted and dotted curves represent solutions of the equations $\varepsilon^2 - 2 \varepsilon = p_y^2$ and $\varepsilon^2 + 2 \varepsilon = p_y^2$. The spectrum is continuous in the region A defined by Eq. (2.21), discrete in the region B defined by Eq. (2.22), and there are no states in the region C defined by Eq. (2.23).	30
2.6	The plots of $V(k)$ (2.31) for $p_y = 0$. The cases of $\varepsilon = 0.1$ and $\varepsilon = 2.1$ are shown on the panels (a) and (b). The classically permitted region corresponds to $V(k) < 0$, as indicated by the thick horizontal line. Thus, the panels (a) and (b) represent bounded and unbounded motion.	34
2.7	Low-energy levels $\varepsilon_n(p_x, p_y)$ for $q = 0.044$. Panel (a) shows $\varepsilon_n(p_x, 0)$ vs p_x for $p_y = 0$, and panel (b) shows $\varepsilon_n(0, p_y)$ vs p_y for $p_x = 0$. Solid lines represent exact numerical diagonalization of Hamiltonian (2.25). Dashed lines represent the WKB analytical approximation (2.39). All quantities are presented in the adopted dimensionless units (2.9).	36
2.8	Energy levels $\varepsilon_n(0, 0)$ vs the quantum number n at $p_x = 0$ and $p_y = 0$ for $q = 0.044$. The horizontal axis shows the combination $q(n + 1/2)$. The circles represent solutions of the WKB equation (2.39), and the small points inside the circles represent numerical data. The quadratic approximation (2.41) is shown by the solid line. All quantities are presented in the adopted dimensionless units (2.9).	37

2.9	The absolute values of the wave functions $ \psi_j^A $ and $ \psi_j^B $ on the sublattices A and B vs the layer number j for $q = 0.044$, $p_x = q/2$, and $p_y = 0$. The variable n denotes the energy level number.	38
2.10	Energy spectrum $\varepsilon_n(p_x, 0)$ vs p_x at $p_y = 0$ and $q = 0.044$ for the system with a finite number of layers N . The dashed-dotted, dashed, and solid lines correspond to $N = 7, 21$, and ∞ . All quantities are presented in the adopted dimensionless units (2.9).	39
2.11	Energy spectrum around $\varepsilon = 2$ for $q = 0.044$ and $p_y = 0$. The solid lines are obtained by numerical diagonalization of Hamiltonian (2.25). The dashed lines, obtained from Eq. (2.39), are labeled by the integer n shown on the right. The dashed-dotted lines, obtained from Eq. (2.44), are labeled by the integer \tilde{n} shown at the top. This plot illustrates a transition from discrete to continuous spectrum. All quantities are presented in the dimensionless units (2.9).	41
2.12	The absolute value of the wave function $ \psi_j $ vs the layer number j for a state from the domain of continuous spectrum. The parameters of the plot are $\tilde{n} = -250$, $\varepsilon_{\tilde{n}} = 10.98$, $p_x = p_y = 0$, and $q = 0.044$. The solid and dashed lines represent exact numerical diagonalization of Hamiltonian (2.25) and the approximate analytical formula (2.50), respectively.	43
3.1	Schematic view of two graphene layers and the directions of the applied electric and magnetic field.	46
3.2	Schematic energy spectrum of graphite in the crossed magnetic and electric fields (represented by q and u) in the limit $t_1 \rightarrow 0$ at different values of u . (a) The Dirac cones have the same energy for zero electric field at $u = 0$. (b) With an increase of u , the Dirac cones shift vertically. (c) When the resonant condition $u = vq$ is met, the R-branches of the Dirac cones align and become degenerate.	47
3.3	Numerically calculated energy spectrum and wave functions for a finite system of 150 layers. The top panels show the energy spectrum, whereas the bottom panels show the wave functions corresponding to the states marked with the “*” and “x” symbols in the top panels. The left and right columns correspond to the non-resonant $2u = qv = 0.2t_1$ and resonant $u = qv = 0.2t_1$ cases, respectively. The unit of energy scale corresponds to tunneling amplitude t_1	50
3.4	A schematic view of the mesa-type structure.	52
3.5	(a) Interlayer tunneling spectra of graphite mesa-structure at various in-plane magnetic fields (the magnitude of the field for each curve is indicated on the right). (b) Dependence of the position of the tunneling conductance peak on the in-plane magnetic field B	53

4.1	Panel (a): 1D chain of atoms with alternating tunneling amplitudes t_1 and t_2 representing the Shockley model, Eq. (4.1). Panel (b): The bulk energy spectrum of the system, Eq. (4.8), with a non-zero gap for $ t_1 \neq t_2 $. Panel (c): The exponentially decaying edge state, Eq. (4.18), for $ t_1 / t_2 < 1$ with the penetration depth $\xi = 1/\ln t_2/t_1 $.	58
4.2	Topological formulation of the Shockley criterion (4.19). Panels (a) and (b) compare the two cases, where the root q_0 (the red dot) lies inside or outside the unit circle $C = \{q = e^{ik}, k \in (0, 2\pi)\}$. An edge state exists for $ q_0 < 1$, panel (a), and does not exist for $ q_0 > 1$, panel (b). An alternative formulation in terms of the winding number (4.20) is illustrated in panels (c) and (d). The edge state exists if the winding number is non-zero, panel (c), and does not exist if the winding number is zero, panel (d).	63
4.3	3D generalization of the Shockley model described by Hamiltonian (4.30) with $h(\mathbf{p})$ defined by Eq. (4.33). The arrows show the staggered direction of the Rashba vector \mathbf{n} .	67
4.4	Energy spectrum of the 3D Shockley model described by Hamiltonian (4.30) in the vicinity of $\mathbf{p} = 0$. The spectrum of the bulk states, Eq. (4.35), is shown by the solid parabolas in both panels. According to the Shockley criterion, surface states exist if $ t_1 < t_2 $, panel (a), and do not exist otherwise, panel (b). The surface states have the linear dispersion, Eq. (4.34), shown by the transparent Dirac cone in panel (b).	69
4.5	The thick blue curve is a vortex line in the 3D momentum space defined by Eq. (4.36). Its projection onto the 2D momentum space \mathbf{p} defines the boundary of the shaded area, where the surface states exist.	70
4.6	Illustration of the diamond crystal structure and the tight-binding model described by Hamiltonian (4.41). The lattice has two atoms in a unit cell shown by the red (A) and blue (B) spheres.	73
4.7	Lines of constant value for the graphene spectrum function $ t_1(\mathbf{p}) / t_1 = C$, for $C = 0.5, 1, 2$, within the Brillouin zone (BZ), denoted by the dashed lines. The contour lines degenerate to points at the BZ corners (K and K' points) at $C = 0$ and at the BZ center at $C = 3$. The thick red dots denote the time-reversal-invariant momenta points (4.47).	75
4.8	The plot of the particle-hole symmetric spectrum $E_0(\mathbf{p})$, Eq. (4.46), induced by the spin-orbit Hamiltonian $h(\mathbf{p})$ (4.45). In the vicinity of the time reversal invariant points, shown with the thick red dots, the Hamiltonian (4.45) becomes linear in momentum. The dashed line denotes the boundary of the BZ.	76

- 4.9 Vortex lines in the 3D momentum space defined by Eq. (4.56), and shown for different values of the parameters: (a) $|t_1| > |t_2|$, (b) $|t_1| = |t_2|$, and (c) $|t_1| < |t_2| < 3|t_1|$. The vortex lines are shown by the thick lines with the arrows representing vorticity. The thin lines show projections of the vortex lines, which encircle the shaded area in the 2D momentum space \mathbf{p} , where the Shockley criterion (4.54) is satisfied and the surface states exist. The dashed lines show the boundaries of the BZ. The part of the vortex lines residing in the first BZ is highlighted in red in panel (b). The three panels show the evolution of the vortex lines with the change of the parameters of the Hamiltonian. At $|t_1| = |t_2|$, the vortex lines reconnect at the TRIM points and change their topology from spirals for $|t_1| > |t_2|$ to the loop for $|t_1| < |t_2|$. The change of the vortex lines topology is responsible for a transition from the “weak” to “strong” TI phase in the Hamiltonian (4.41). 81
- 4.10 The crystal of Bi_2Se_3 is formed by quintuple layers, schematically shown by the blue boxes. Each quintuplet consists of the alternating layers Se-Bi-Se-Bi-Se. The tight-binding tunneling amplitudes t_1 and t_2 connect the orbitals of the outermost edges of the quintuplets. Then, depending on whether t_2 or t_1 is broken at the surface, as shown by the red line in panels (a) and (b), surface states occur in different regions of the 2D momentum space, as shown in Panels (c) and (d). 85
- 4.11 Plot of the function $t(k)$ in the complex plane of $(\text{Re } t, \text{Im } t)$. The second-order expansion for $t(k)$, given by Eq. (4.79) is plotted by the solid line for $-\pi/2 < k < \pi/2$. The function $t(k)$ in the Shockley model, given by Eq. (4.65) with the parameters t_1 and t_2 from Eq. (4.63), is plotted by the dashed line. The Shockley contour winds around the origin, which guarantees existence of the surface state. . . 90
- 4.12 An illustration of the generalized Hamiltonian (4.82). The Hamiltonian describes a tight-binding model with the elementary cell comprised of the A and B sites, which are connected via the complex tight-binding amplitudes t_1 , t_2 and t_3 94
- 4.13 Topological formulation of the Shockley criterion. The roots $q_{1,2}$ of Eq. (4.85) are shown in panels (a) and (b) by red dots. An edge state exists if the roots are on the same side of the unit circle $C = \{q = e^{ik}, k \in (0, 2\pi)\}$, as shown in panel (a). No edge state exists if the roots are on the opposite sides of the unit circle, as shown in panel (b). The thick black dot at the origin is the pole of Eq. (4.85). An alternative formulation in terms of the winding number (4.97) is shown in panels (c) and (d). An edge state exists if the contour $C' = \{t(k), k \in (0, 2\pi)\}$ winds around the origin, as shown in panel (c). No edge state exists if the contour C' does not wind around the origin, as shown in panel (d). 99

5.1	Thin film of a topological insulator of thickness d in a parallel magnetic field B_y . The surface states ψ_1 and ψ_2 shown in red and blue overlap and couple when the thickness d is comparable with the decay length ξ of the surface state.	107
5.2	The spectrum (5.7) of Hamiltonian (5.6) for different values of magnetic shift: (a) $q = 0$, (b) $q = 2t$, (c) $q = 4t$	109
5.3	Electronic spectrum (5.8) of the thin film consists of the two Dirac cones spin-polarized in the opposite directions as shown with circulating arrows. The Dirac cones are shifted by q_x due to the parallel magnetic field B_y . Tunneling between the Dirac cones is dominated by the electrons with momenta \mathbf{p}_1 and \mathbf{p}_2 where the shifted Fermi circles $ \mathbf{p} \pm \mathbf{q}/2 = p_F$ intersect.	111
5.4	(a) The tunneling conductances for spin-unpolarized $G_0^{(1)}$, Eq. (5.13), and spin-polarized $G_0^{(2)}$, Eq. (5.14), Fermi circles are shown by the dashed and solid black lines, respectively. The latter curve $G_0^{(2)}$ corresponds to the negative magnetoresistance. The red curve is the spin polarization (5.16) of the tunneling current, and the right vertical axis shows its value, where 1 corresponds to 100% spin polarization. (b) Schematic views of the shifted Fermi circles $ \mathbf{p} \pm \mathbf{q}/2 = p_F$ for the corresponding values of q . The tunneling is allowed for the momenta \mathbf{p}_1 and \mathbf{p}_2 where the Fermi circles intersect, also shown in Fig. 5.3. The spin polarizations for these momenta are shown by the blue and red arrows corresponding to the ψ_1 and ψ_2 surfaces. The vector sum of the arrows of the same color defines the net spin polarization of the tunneling current, which grows with the increase of q as illustrated in the bottom of panel (b).	114
6.1	(a) Loop-current order in a CuO_2 plane. Black arrows show directions of microscopic persistent currents between copper and oxygen atoms. Green arrow shows the anapole moment \mathbf{N} . (b) Chiral order constructed on a series of parallel CuO_2 planes. The vector \mathbf{N} rotates by the angle $\pi/2$ from one layer to another, and the period of the structure is fourfold. The blue and red curves are the two magnetic field lines that intertwine in a double helix.	121
6.2	(a) Left: Feynman diagram for the effective action of electromagnetic fields (wavy lines), obtained by integrating out the electron field (solid lines with arrows). Right: The magnetoelectric term in the effective action, Eq. (6.5), where the double line represents the anapole moment \mathbf{N} . (b) Coupling between the magnetoelectric terms at the neighboring layers produces the effective action for the electric field in Eq. (6.9). The dashed wavy line represents the magnetic field propagator, and the double solid line represents the interlayer correlator of the anapole moments in Eq. (6.2).	126

6.3	Schematic illustration of the rotation of electric polarization for the chiral state shown in Fig. 6.1(b). The electric field $\mathbf{E}^{(n)}$ at the bottom layer induces the magnetization $\mathbf{M}^{(n)}$, which couples to the top layer and induces the electric polarization $\mathbf{P}^{(n+1)} \perp \mathbf{E}^{(n)}$ because of the twist in the anapole moments $\mathbf{N}^{(n)} \perp \mathbf{N}^{(n+1)}$	130
A.1	Tight-binding model of the loop-current order in a CuO_2 plane. The phase χ describes the alternating magnetic fluxes triangles.	140
A.2	Electronic spectrum (A.38) of Hamiltonian (A.29) for various values of parameter χ : (a) $\chi = 0$, (b) $\chi = \pi/3$, (c) $\chi = \pi/2$, (d) $\chi = \pi$. The energy axis ε is given in eV, whereas the momenta run across the Brillouin zone, i.e. $ p_x < \pi$ and $ p_y < \pi$	144

List of Abbreviations

1D	one-dimensional
2D	two-dimensional
3D	three-dimensional
TI	topological insulator
2DEG	two-dimensional electron gas
AMRO	angular magnetoresistance oscillations
QHE	quantum Hall effect
AHE	anomalous Hall effect
LL	Landau levels
WKB	Wentzel Kramers Brillouin approximation
BZ	Brillouin zone
CMTC	Condensed Matter Theory Center
CNAM	Center for Nanophysics and Advanced Materials

Chapter 1: Introduction

1.1 Certain low-dimensional models

Low-dimensional physics is one of the key areas in the modern condensed matter research. It covers a large number of diverse physical phenomena, which occur in spatial dimensions less than three. The low dimensionality intricately impacts the physics and often gives rise to exotic phenomena, which are not available in three dimensions (3D). Let us review a few basic low-dimensional systems and models that have been of interest recently.

1.1.1 One dimension. Shockley model

Let us begin with an important model introduced by Shockley [1] to study edge states in one-dimensional (1D) periodic lattices. In the tight-binding description [2, 3], the unit cell of the lattice consists of two atoms labeled as A and B, which are connected via alternating nearest-neighbor tight-binding amplitudes t_1 and t_2 as shown in Fig. 1.1(a). In the momentum k space, the Bloch Hamiltonian of the model

$$H(k) = \begin{pmatrix} 0 & t_1 + t_2 e^{ik} \\ t_1 + t_2 e^{-ik} & 0 \end{pmatrix} \quad (1.1)$$

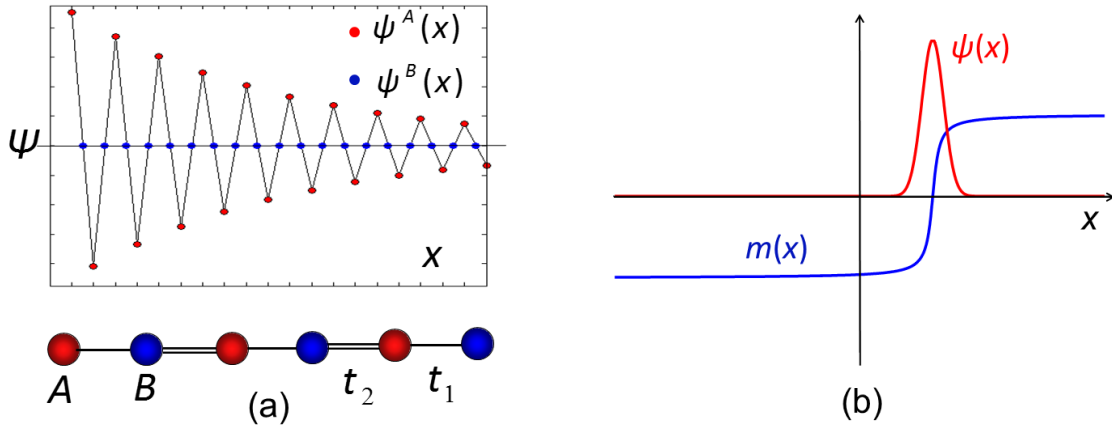


Figure 1.1: (a) One dimensional Shockley model is shown in the bottom. Localized Shockley wave function (1.3) is shown in the top. (b) The continuous approximation of the Shockley model - the Jackiw-Rebbi model (1.4). Continuous function $m(x)$ (shown in blue) models a domain wall. There is a non-trivial eigenstate (1.5) (shown in red) localized in the vicinity of the domain wall.

acts in a sublattice space

$$\Psi(k) = \begin{bmatrix} \psi^A(k) \\ \psi^B(k) \end{bmatrix}.$$

The energy spectrum of the Hamiltonian, which is given by the absolute value of the off-diagonal element of Eq. (1.1)

$$\varepsilon(k) = \pm |t_1 + t_2 e^{ik}|, \quad (1.2)$$

is gapped unless the tight-binding amplitudes are of equal magnitude $|t_1| = |t_2|$. The eigenvectors of Eq. (1.1), which correspond to spectrum (1.2), are the delocalized Bloch states propagating through the entire system as plane waves e^{ikx} . Besides the delocalized states, the system may have edge states in case of open boundary

conditions. If the bond t_2 is broken at the boundary as shown in Fig. 1.1(a), one finds a zero-energy Shockley eigenstate

$$\Psi(x) = \begin{bmatrix} (-t_1/t_2)^x \\ 0 \end{bmatrix}. \quad (1.3)$$

If $t_1 > t_2$, the solution (1.3) grows for $x > 0$ and is, thus, spurious. If $t_2 > t_1$, the solution is physical since it decays for $x > 0$, as shown in Fig. 1.1(a). In such a way, the Shockley criterion can be formulated intuitively: *The 1D bipartite lattice has an edge state if the stronger bond is broken at the edge.*

Let us also mention an important continuous version of the Shockley model - the Jackiw-Rebbi model [4]. Let us fix the second Shockley amplitude $t_2 = -t$ and assume that the first Shockley amplitude t_1 is a continuous function of x , i.e. $t_1(x) = t + m(x)$. Here, the function $m(x)$ is referred to as the “mass term” in the high-energy literature. The profile of the function $m(x)$ changing sign from left to right, as shown in Fig. 1.1(b), is called the domain wall. We expand the Hamiltonian (1.1) for small k , substitute $k = -i\partial_x$ and obtain

$$H = \begin{pmatrix} 0 & m(x) - t\partial_x \\ m(x) + t\partial_x & 0 \end{pmatrix}. \quad (1.4)$$

The Hamiltonian has a non-trivial zero-energy eigenstate [5, 6]

$$\Psi(x) = \begin{pmatrix} \exp\left[-\int_0^x \frac{m(x)}{t} dx\right] \\ 0 \end{pmatrix}. \quad (1.5)$$

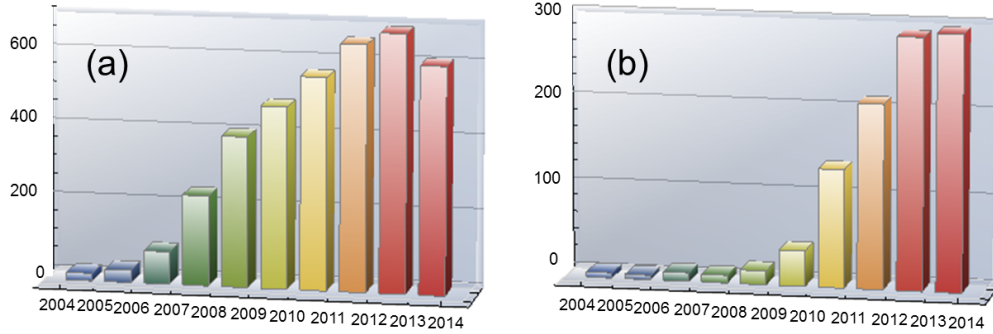


Figure 1.2: The number of papers published in Physical Review B and Physical Review Letters containing key words (a) “graphene” and (b) “topological insulator” in the title or abstract during 2004-2013.

Note, that for a profile of the function $m(x)$ shown in Fig. 1.1, this eigenstate decays at infinity $|x| \rightarrow \infty$ and is localized predominantly in the vicinity of the domain wall, where the function $m(x)$ changes sign.

Despite conceptual simplicity, the Shockley model is very universal and provides a basis for studying edge states for a wide variety of systems. To name a few, the Shockley model describes the edges states in polyacetylene [7], graphene [8], topological insulators [9] and topological superconductors [10, 11].

1.1.2 Two dimensions

Let us proceed to a discussion of a few important two-dimensional (2D) systems. Recently, there has been an outburst of research activity in graphene and topological insulators as evidenced from Fig. 1.2. Let us briefly review these two topics

1.1.2.1 Graphene

Graphene is a monoatomic layer of Carbon atoms arranged in a honeycomb lattice as shown in Fig. 1.3(a). It was synthesized using a famous Scotch tape method in 2004 [12, 13]. Although monoatomic layers were originally believed thermodynamically unstable, graphene proved to be a robust 2D system, where experiment and theory meet in a good agreement. Graphene displays outstanding physical properties surpassing those of other materials. For instance, unique electronic properties of graphene [14] stem from an unusual electronic energy spectrum, which we are going to address briefly. The electronic Hamiltonian can be modeled reasonably well within a tight-binding approximation, where an elementary cell contains two equivalent atoms denoted as A and B connected via a nearest-neighbor hopping t . If we denote the elementary translation vectors as $a_1 = a(1/2, \sqrt{3}/2)$ and $a_2 = a(-1/2, \sqrt{3}/2)$, the momentum space $\mathbf{p} = (p_x, p_y)$ Hamiltonian is

$$H(\mathbf{p}) = \begin{pmatrix} 0 & t(\mathbf{p}) \\ t^*(\mathbf{p}) & 0 \end{pmatrix}, \quad \text{where } t(\mathbf{p}) = 1 + e^{i\mathbf{p}a_1} + e^{i\mathbf{p}a_2}. \quad (1.6)$$

The energy spectrum of the Hamiltonian has two bands $\varepsilon(\mathbf{p}) = \pm|t(\mathbf{p})|$ plotted in Fig. 1.3. In the vicinity of the corners of the Brillouin zone denoted as K and K' in Fig. 1.3(b), the off-diagonal element of Hamiltonian (1.6) can be expanded as $t(\mathbf{p}) = v(\mp p_x - ip_y)$, where $v = \frac{at\sqrt{3}}{2}$. As a result, the electronic spectrum becomes linear in momentum

$$\varepsilon(\mathbf{p}) = \pm|t(\mathbf{p})| \approx \pm vp. \quad (1.7)$$

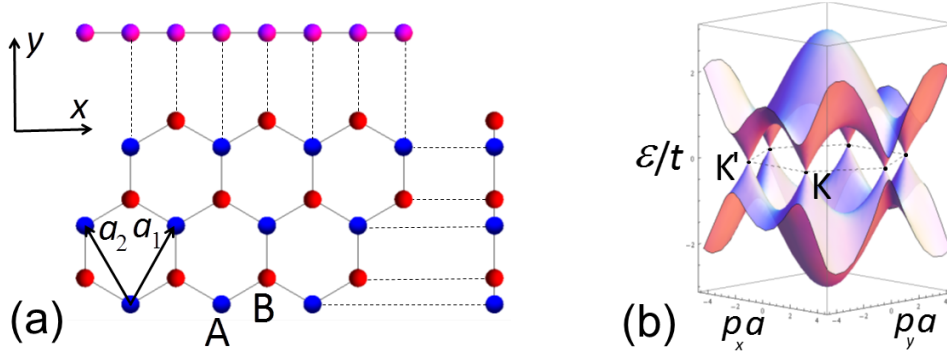


Figure 1.3: (a) Honeycomb lattice of graphene with A (blue) and B (red) sublattices. Projection of the lattice onto the horizontal axis generates monoatomic lattice, and onto the vertical axis - the bipartite Shockley lattice. (b) The energy spectrum of graphene. The dashed line denotes a boundary of the Brillouin zone.

This linear dispersion, which is often referred to as the Dirac cone, is at the heart of the unusual electronic properties of graphene. To list a few, graphene exhibits remarkable electronic transport [15], fascinating optical properties [16], unusual quantization of the Landau Levels (LL) $\epsilon_n = \pm\sqrt{2evBn}$ in the strong magnetic field B that leads to unconventional quantum Hall effect (QHE) [17] observable at room temperature, etc. Graphene triggered a search of other Dirac materials, i.e. the materials with linear electronic dispersion (e.g. topological insulators, Weyl semimetals, etc.).

In passing, let us note a curious resemblance of the graphene lattice to the Shockley model. In Fig. 1.3(a), we project the graphene lattice onto horizontal and vertical axes. While projecting onto the vertical axis, all A atoms collapse on the “blue” Shockley sites, whereas B - on the “red”. In contrast, the projection onto the horizontal axis yields a trivial lattice with a single atom per unit cell. Based on this

intuition, we expect that the Shockley edge states (do not) exist on the (armchair) zigzag boundary of graphene samples, which is confirmed by explicit calculations [8].

1.1.2.2 Topological Insulators

After the experimental observation of QHE in 1980, a new paradigm of topological order emerged in the condensed matter community. It was suggested that apart from symmetry classification, some phases of matter should be classified according to their topological properties. Recent interest in topological insulators (TI) lies in a theoretical prediction [18–29] and subsequent experimental realization [30–32] of the so-called Z_2 TIs (we leave the discussion of other exotic topological orders outside of the scope of this thesis). These are the materials with strong spin-orbit coupling, where the topological properties guarantee the existence of surface states with the spin-polarized Dirac-like dispersion.

We study the surface states of the Z_2 TIs using the Shockley formalism in Chapter 4. Below, let us review the famous Haldane model [33], which is a precursor of modern theory of TIs. This phase represents a gapped insulator exhibiting the anomalous Hall effect (AHE). Incidentally, the tight-binding model of the Haldane phase was formulated on graphene lattice. In addition to the nearest tight-binding amplitude t , the Haldane model includes complex next-nearest-neighbor hopping $t_1 e^{i\phi}$ as well as alternating on-site potentials $\pm M$ on the A and B sublattices as shown in Fig. 1.4(a). As in previous Section 1.1.2.1, we write the Bloch Hamiltonian

$$H(\mathbf{p}) = t_0(\mathbf{p})I + \mathbf{t}(\mathbf{p}) \cdot \boldsymbol{\tau}, \quad (1.8)$$

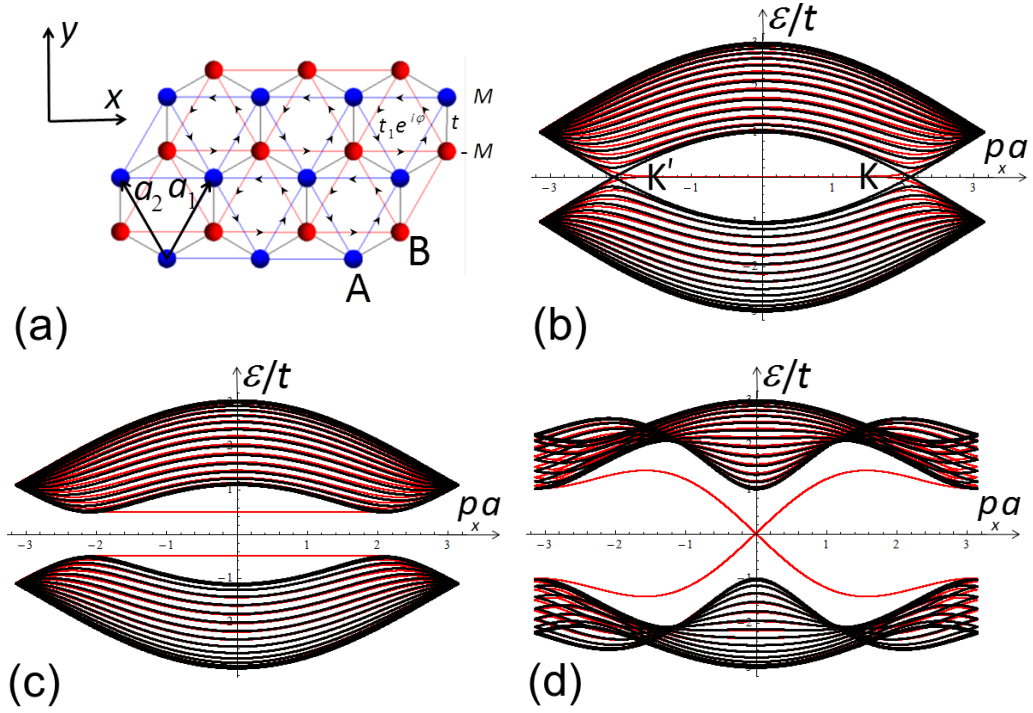


Figure 1.4: (a) Tight-binding lattice of the Haldane model. (b) Energy spectrum corresponding to pure graphene $t_1 = M = 0$. For reference, the labels K and K' represent the same points in the momentum space as in Fig. 1.3(b). (c) Energy spectrum corresponding to the trivial topological phase $t_1 = 0$, $M = 0.5t$. (d) Energy spectrum corresponding to the non-trivial phase $t_1 = 0.5t$, $M = 0$, $\phi = \pi/2$. In panels (b)-(d), the red curves were obtained in a ribbon geometry with 30 atoms in the y direction and infinite number of atoms in the x direction. The black curves were obtained from the bulk spectrum (1.9). So, the red line not covered by the black line partner corresponds to an edge mode.

where the 2-by-2 Pauli $\boldsymbol{\tau} = (\tau_x, \tau_y, \tau_z)$ and identity \mathbf{I} matrices act in the space of spinors $\Psi(\mathbf{p}) = [\psi^A(\mathbf{p}) \psi^B(\mathbf{p})]^T$, and the coefficients $\mathbf{h}(\mathbf{p})$ depend on the tight-binding parameters and the 2D momentum $\mathbf{p} = (p_x, p_y)$ ¹. The energy spectrum of the Haldane Hamiltonian

$$\varepsilon(\mathbf{p}) = t_0(\mathbf{p}) \pm |\mathbf{t}(\mathbf{p})| \quad (1.9)$$

is gapped unless $|M| = 3\sqrt{3}t_1 \sin \phi$. Notice, that the off-diagonal elements of the graphene Hamiltonian (1.6) and the Haldane Hamiltonian coincide, since $t(\mathbf{p}) = t_x(\mathbf{p}) + it_y(\mathbf{p})$. The only difference appears in the diagonal terms determined by $t_z(\mathbf{p})$ and $t_0(\mathbf{p})$. The effect of the term $t_z(\mathbf{p})$ is crucial: it gappes out the Dirac cones at the points K and K' and, so, introduces a mass (in the terminology of the Jackiw-Rebbi model). The masses at the two non-equivalent Dirac points are $m_K = M + 3\sqrt{3}t_1 \sin \phi$ and $m_{K'} = M - 3\sqrt{3}t_1 \sin \phi$. If the signs of the two masses coincide, i.e. $m_K m_{K'} > 0$ (or equivalently $|M| > 3\sqrt{3}|t_1 \sin \phi|$), we call such a case topologically trivial. However, if the signs of the masses are opposite, i.e. $m_K m_{K'} < 0$ (or equivalently $|M| < 3\sqrt{3}|t_1 \sin \phi|$), we call such a case topologically non-trivial. Now, let us imagine the entire 2D space is divided into two regions: one - topologically trivial, and another - topologically non-trivial. Then, when passing from one region to another, one will change the sign of at least one Jackiw-Rebbi

1

$$\begin{aligned} t_x(\mathbf{p}) &= \text{Re } t(\mathbf{p}) = t(1 + \cos \mathbf{p}\mathbf{a}_1 + \cos \mathbf{p}\mathbf{a}_2), \\ t_y(\mathbf{p}) &= \text{Im } t(\mathbf{p}) = t(\sin \mathbf{p}\mathbf{a}_1 + \sin \mathbf{p}\mathbf{a}_2), \\ t_z(\mathbf{p}) &= M + 2t_1 \sin \phi [\sin \mathbf{p}\mathbf{a}_1 - \sin \mathbf{p}\mathbf{a}_2 - \sin \mathbf{p}(\mathbf{a}_1 - \mathbf{a}_2)], \\ t_0(\mathbf{p}) &= 2t_1 \cos \phi [\cos \mathbf{p}\mathbf{a}_1 + \cos \mathbf{p}\mathbf{a}_2 + \cos \mathbf{p}(\mathbf{a}_1 - \mathbf{a}_2)]. \end{aligned}$$

mass. According to the discussion in Section 1.1.1, the mass domain wall between the two regions will generate the Jackiw-Rebbi edge state.

Indeed, exact numerical diagonalization finds such edge states. In Fig. 1.4(b)-(d), we plot the spectrum of the Haldane Hamiltonian in a ribbon geometry. The width of the ribbon is 30 atoms in the y direction. The ribbon is infinite in the x direction, and p_x is a corresponding momentum. For each momentum p_x , we effectively have a 1D tight-binding Hamiltonian with open boundary conditions, which we diagonalize and obtain 30 eigenvalues. These eigenvalues trace out the red curves as p_x goes through the Brillouin zone in Fig. 1.4. For reference, the spectrum of the Hamiltonian with the periodic boundary conditions is plotted in black. So, the red lines not covered by the black lines correspond to the edge states. In Fig. 1.4(b), we show a spectrum of the graphene ribbon without the Haldane currents, i.e. $t_1 = M = 0$. Compare the Dirac points K and K' for the graphene layer in Fig. 1.3(b) with the graphene ribbon in Fig. 1.4(b). In consistency with the intuition discussed in the end of Sec. 1.1.2.1, we indeed find the Shockley edge modes at the zigzag edges shown with the thin red line. In fact, the line is double degenerate, where the degeneracy corresponds to the two states localized at the opposite edges. Next, in a case of the trivial Haldane phase ($t_1 = 0$ and $M = 0.5t$) shown in Fig. 1.4(c), the degeneracy of edges states is lifted, and the spectrum becomes gapped. In the case of the non-trivial Haldane phase ($t_1 = 0.5t, M = 0t$, and $\phi = \pi/2$), there are two chiral edge modes traversing the gap. They have opposite velocities and are localized at the opposite edges of the system. In the topologically non-trivial regime, the existence of the edge states is protected by

topology. In contrast, in the topologically trivial case, the existence of the edge states strongly depends on the boundary conditions. Let us also note that the two phases of the Haldane model can be distinguished by the Chern number. The Chern number C is a topological index, which is defined as the integral over the 2D Brillouin zone using the eigenstates $\Psi(\mathbf{p})$ of Eq. (1.8)

$$C = \frac{i}{2\pi} \int d^2p \langle \partial_{p_x} \Psi(\mathbf{p}) | \partial_{p_y} \Psi(\mathbf{p}) \rangle = \frac{1}{4\pi} \int d^2p [\hat{\mathbf{t}} \cdot (\partial_{p_x} \hat{\mathbf{t}} \times \partial_{p_y} \hat{\mathbf{t}})], \quad (1.10)$$

where $\mathbf{t} = \frac{\mathbf{t}(\mathbf{p})}{|\mathbf{t}(\mathbf{p})|}$ is a unit vector. The Chern number is an integer Z valued quantity and becomes 0 and ± 1 for the topologically trivial and non-trivial cases. The Haldane order has the quantized Hall conductance $\sigma_{xy} = Ce^2/h$. The value of the Haldane's proposal is that it was the first topological order exhibiting quantized AHE in the absence of external magnetic field. There are reports that AHE has been observed experimentally [34].

1.2 In current thesis: multilayer structure of novel 2D materials

So, there has been a considerable amount of effort in studying the aforementioned 2D materials, and they are now fairly well understood. A new step in research is to combine these novel 2D layers into 3D stacks (just like a 2D layer consists of a family of 1D chains glued together). This concept is not purely abstract. Recently, there has been a number of proposals to study stacks of novel 2D materials; let us list a few examples. It was suggested to assemble the van der Waals heterostructures with tailored properties using diverse library of available atom-thick materials

(including graphene) [35]. For example, graphene stacked on Boron Nitride substrate displays a Moire pattern, which has a dramatic effect on electronic spectrum of graphene [36]. The topological insulator film coated by ferromagnet produces the AHE state [34]. Multilayer structure of magnetically doped topological insulator and ordinary insulator films realizes the Weyl semimetal phase [37]. It was suggested how to engineer 3D topological insulators using Rashba-type spin-orbit coupled heterostructures [38]. The salient feature of all these proposals is that the interlayer coupling is crucial for the new physics.

So, the main focus of current thesis is studying stacks of novel 2D materials. We emphasize how interlayer interaction is responsible for emergent physics in 3D stacks. We discuss layered structures of the Dirac materials such as graphene and topological insulators in Chapters (2)-(5). In these chapters, the interlayer coupling produces curious electronic energy spectra. We also address transport phenomena associated with these spectra. We elucidate a role of an in-plane magnetic and out-of-plane electric field as spectroscopic tools in these materials. In Chapter (6), we propose a novel helical order in multilayer cuprate superconductors. The interlayer magnetic interaction produces optical gyrotropy, which was recently observed experimentally. Now, let us briefly discuss the content of each chapter.

1.2.1 Graphene multilayer in a parallel magnetic field

We begin with a study of graphene bilayer and multilayers in a strong in-plane magnetic field as shown in Fig. 1.5. Within a minimal coupling model, we calculate

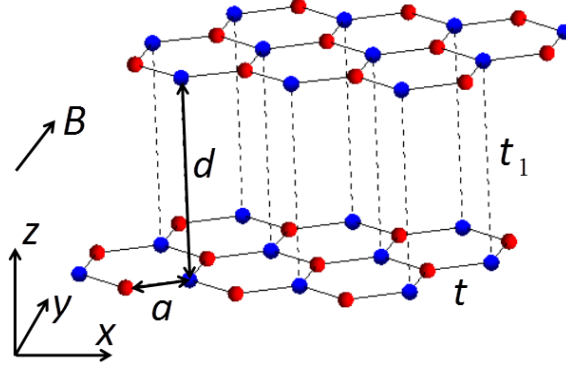


Figure 1.5: A pair of Bernal-stacked graphene layers in the parallel magnetic field \mathbf{B} applied along the y direction. Variables t and t_1 denote the electron intra and interlayer tunneling amplitudes.

the energy spectrum of the Bernal-stacked graphene bilayer and multilayer, including graphite. Using the semiclassical analytical approximation and exact numerical diagonalization, we find that the energy spectrum consists of two domains. In the low- and high-energy domains, the semiclassical electron orbits are closed and open, so the spectra are discrete and continuous, correspondingly. The discrete energy levels are the analogs of the Landau levels. In both domains, the electron wave functions are localized on a finite number of graphene layers, so the results can be applied to graphene multilayers of a finite thickness.

1.2.2 Graphene multilayer in crossed electric and magnetic fields

In Chapter 3, we study the graphene multilayer in both in-plane magnetic B and out-of-plane electric E fields. We calculate the electronic energy spectrum and show that the problem is equivalent to the Wannier-Stark ladder. Similar to the case studied in Chapter 2, we find that the wave functions are localized on a

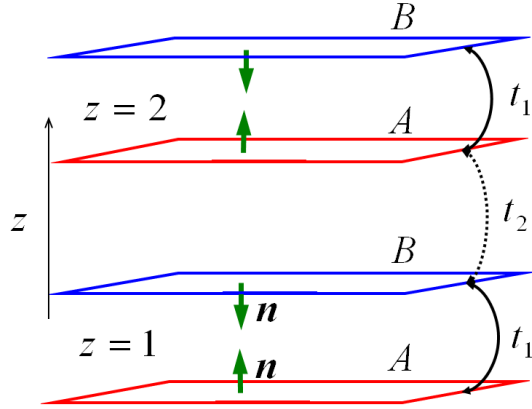


Figure 1.6: Illustration of the 3D Shockley model. The arrows show the staggered direction of the Rashba vector (for a detailed discussion see Section 4.3).

finite number of layers. We find that the spectrum undergoes a dramatic change, where the resonant condition $E = vB$ is achieved (here v is the velocity of the Dirac carriers in graphene). We discuss an experimental study of graphite mesa in the strong in-plane magnetic field $B < 55$ T. The tunneling spectrum $dI/dV(V)$ shows a pronounced peak at finite voltage V_0 which grows linearly with B . We explain the experiment within the developed theoretical framework and attribute the observed tunneling peak to a resonant delocalization of the wave functions.

1.2.3 Shockley edge states in topological insulators

In Chapter 4, we turn to a study of a new family of layered Dirac materials - topological insulators. We study the surface states in these materials within the Shockley model. We generalize the 1D model to 3D case representing a sequence of coupled Shockley layers as illustrated in Fig. 1.6. The Hamiltonian of the 3D

Shockley model is a 2×2 matrix with the off-diagonal element $t(k, \mathbf{p})$ depending also on the out-of-plane momentum k . We show that the existence of the surface states depends on the complex function $t(k, \mathbf{p})$. The surface states exist for those in-plane momenta \mathbf{p} where the winding number of the function $t(k, \mathbf{p})$ is non-zero when k is changed from 0 to 2π . The sign of the winding number determines the sublattice on which the surface states are localized. The equation $t(k, \mathbf{p}) = 0$ defines a vortex line in the three-dimensional momentum space. Projection of the vortex line onto the space of the two-dimensional momentum \mathbf{p} encircles the domain where the surface states exist. We illustrate how this approach works for a well-known model of a topological insulator on the diamond lattice. We find that different configurations of the vortex lines are responsible for the “weak” and “strong” topological insulator phases. A topological transition occurs when the vortex lines reconnect from spiral to circular form. We apply the Shockley model to Bi_2Se_3 and discuss applicability of a continuous Jackiw-Rebbi approximation for the description of the surface states. We conclude that the tight-binding model gives a better description of the surface states.

1.2.4 Thin film of a topological insulator in a parallel magnetic field

In Chapter 5, we consider a topological insulator in a thin film geometry illustrated in Fig. 1.7. In this case, the bulk degrees of freedom can be integrated out, and one can focus on studying the topological edge states localized at the opposite surfaces of the film. In an ultra-thin limit, the surface states are coupled

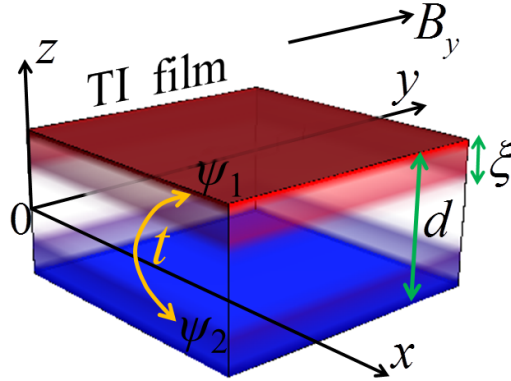


Figure 1.7: Thin film of a topological insulator of thickness d in a parallel magnetic field B_y . The surface states ψ_1 and ψ_2 shown in red and blue overlap where the thickness d is comparable with the decay length ξ of the surface state.

by a finite tunneling amplitude t . Similar to a setting of Chapters 2 and 3, we study a thin-film in the crossed electric and magnetic fields. The parallel magnetic field produces a relative shift of the in-plane momenta of the two surface states. An overlap between the shifted Fermi circles and spinor wave functions result in an unusual dependence of the tunneling conductance on the magnetic field. Because spin orientation of the electronic surface states in topological insulators is locked to momentum, spin polarization of the tunneling current can be controlled by the magnetic field.

1.2.5 Chiral structure in the pseudogap phase of cuprates

In Chapter 6, we study yet another family of novel layered materials - the copper oxide compounds (also known as cuprates). Formally, they do not belong

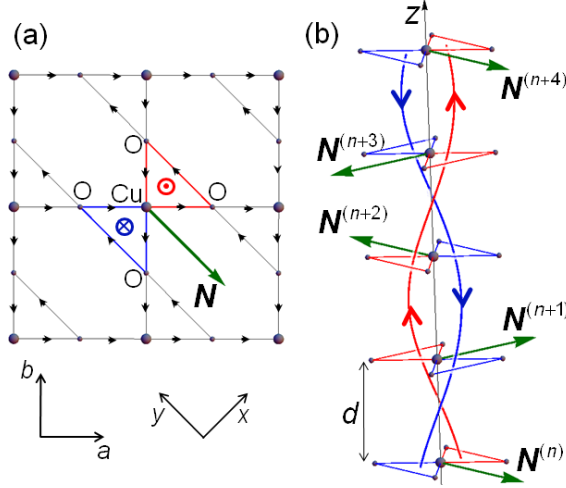


Figure 1.8: (a) Loop-current order in a CuO_2 plane has an anapole moment \mathbf{N} . (b) Chiral order on a series of parallel CuO_2 planes is constructed by rotating vector \mathbf{N} from one layer to another.

to the Dirac materials family, but the model of a single layer does have Dirac cones as explained in Appendix (A.3). For a long time, it was believed that essential physics of cuprate superconductors is confined to 2D CuO_2 layers. However, the new experimental evidence suggests that the interlayer coupling may also be important. Our order is based on the loop-current model by Varma shown in Fig. 1.8, which is characterized by the in-plane anapole moment \mathbf{N} and exhibits the magnetoelectric effect. We propose a helical structure where the vector $\mathbf{N}^{(n)}$ in the layer n is twisted by the angle $\pi/2$ relative to $\mathbf{N}^{(n-1)}$ shown in Fig. 1.8(b). We show that coupling between magnetoelectric terms in the neighboring layers for this structure produces optical gyrotropy.

Chapter 2: Graphene multilayer in a parallel magnetic field

2.1 Introduction

A remarkable manifestation of the Dirac dispersion is the unusual spectrum of the Landau levels in a perpendicular magnetic field, resulting in the anomalous quantum Hall effect (QHE) [13, 17, 39–41]. These results stimulated further investigations of the QHE in the derivatives of graphene. The unusual Landau levels and the QHE were obtained for a graphene bilayer in Ref. [42]. Although the Landau levels in graphite were investigated a long time ago [43, 44], recent studies [45–50] of graphene multilayers with a moderate number of layers found interesting features in the Landau spectrum. Namely, the spectrum consists of the two families of levels, whose energies scale as B and \sqrt{B} , thus indicating the presence of both massive and massless Dirac fermions in the system [45]. The Landau levels for different stacking orders of graphene multilayers were studied in Ref. [51].

On the other hand, much less attention was paid to the orbital effect of a magnetic field parallel to the graphene layers. The Shubnikov-de Haas oscillations were extensively studied in graphite in a tilted magnetic field, but they tend to disappear when the field is parallel to the layers. Ref. [52, 53] studied the influence of a parallel magnetic field on the putative ferromagnetic, superconducting,

and metal-insulator transitions in graphite. In Ref. [54], the angular magnetoresistance oscillations (AMRO) were observed in the stage 2 intercalated graphite (in addition to the Shubnikov-de Haas oscillations) for magnetic fields close to the parallel orientation. AMRO were first discovered in layered organic conductors [55, 56] and subsequently observed in many other layered materials: see, e.g., Ref. [57] and references therein.

In this Chapter, we calculate the electron spectrum of two or many coupled graphene layers in a strong parallel magnetic field. To simplify the problem, we consider only the minimal model with the electron tunneling amplitudes between the nearest sites in the plane (t) and out of the plane (t_1). Our results should be valid for the energies greater than the energies of the neglected higher-order tunneling amplitudes and can be verified by tunneling or optical spectroscopy. We focus only on the orbital effect of the magnetic field and disregard possible spin effects [58]. We find some mathematical similarities between the electron spectrum of graphene multilayers in a parallel magnetic field and that of quasi-one-dimensional [59, 60] and quasi-two-dimensional [61] organic conductors.

We start with the analysis of a graphene bilayer in a parallel magnetic field (Sec. 2.2) and then proceed to the infinite number of layers (Sec. 2.3). We investigate both the quasiclassical electron orbits in momentum space (Sec. 2.3.2.1) and the exact equation for the energy eigenfunctions, which reduces to the Mathieu equation (Sec. 2.3.2.2). We employ both the analytical WKB method and exact numerical diagonalization to find the energy eigenvalues and eigenfunctions. We identify the low-energy domain characterized by closed orbits and discrete spectrum

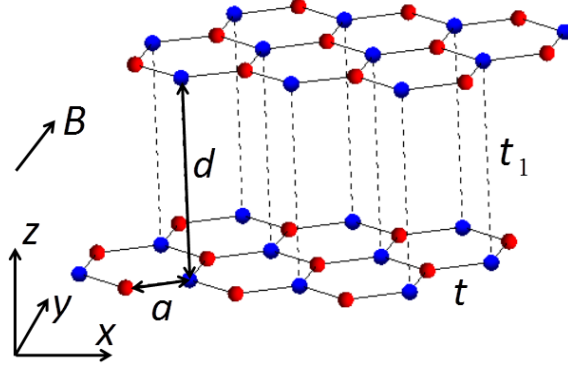


Figure 2.1: A pair of Bernal-stacked graphene layers in the parallel magnetic field \mathbf{B} applied along the y direction. t and t_1 are the electron tunneling amplitudes.

(Sec. 2.3.2.3) and the high-energy domain with open orbits and continuous spectrum (Sec. 2.3.2.4). The case of a finite number of layers is analyzed at the end of Sec. 2.3.2.3.

2.2 Graphene bilayer

2.2.1 Model

First, we consider a graphene bilayer and then generalize the problem to many layers. The crystal lattice of the Bernal-stacked graphene bilayer is shown in Fig. 2.1. The distance between the nearest atoms in graphene is $a = 1.4 \text{ \AA}$, and the distance between the layers is $d = 3.3 \text{ \AA}$. We restrict our analysis to the minimal tight-binding model [50] with the intra- and inter-layer tunneling amplitudes $t = 3.16 \text{ eV}$ and $t_1 = 0.38 \text{ eV}$.

There are two sublattices on each graphene layer. Thus, the electron wave

function is the vector

$$\Psi = (\psi_1^A, \psi_1^B, \psi_2^A, \psi_2^B), \quad (2.1)$$

where the subscripts 1 and 2 enumerate the layers, and the superscripts A and B denote sublattices on each layer. Sublattices can be selected in various ways. It is convenient for us to assign the atoms connected by the interlayer tunneling t_1 in the Bernal stack to sublattice A and other atoms to sublattice B, as shown in Fig. 2.1.

In the vicinity of the K point in the Brillouin zone, the electron Hamiltonian has the form

$$H = \begin{pmatrix} v_F(\mathbf{p} \cdot \boldsymbol{\sigma}) & t_1 I^A \\ t_1 I^A & v_F(\mathbf{p} \cdot \boldsymbol{\sigma}^*) \end{pmatrix}. \quad (2.2)$$

Hamiltonian (2.2) acts on the vector (2.1). Correspondingly, $\boldsymbol{\sigma} = (\sigma_x, \sigma_y)$ are the Pauli matrices acting in the sublattice space; $\mathbf{p} = p_x \hat{\mathbf{x}} + p_y \hat{\mathbf{y}}$ is the in-plane momentum measured from the K point; $v_F = (3/2\hbar)ta \approx 10^8$ cm/s is the electron velocity in graphene. The terms $v_F(\mathbf{p} \cdot \boldsymbol{\sigma})$ and $v_F(\mathbf{p} \cdot \boldsymbol{\sigma}^*)$ describe the in-plane Hamiltonians of the graphene layers. Our choice of the A and B sublattices results in the diagonal elements having both $\boldsymbol{\sigma}$ and $\boldsymbol{\sigma}^*$ (complex-conjugated) terms. The term $t_1 I^A$ represents the interlayer tunneling, where the matrix

$$I^A = \frac{1}{2}(I + \sigma_z) = \begin{pmatrix} 1 & 0 \\ 0 & 0 \end{pmatrix} \quad (2.3)$$

connects sublattices A of the adjacent graphene layers.

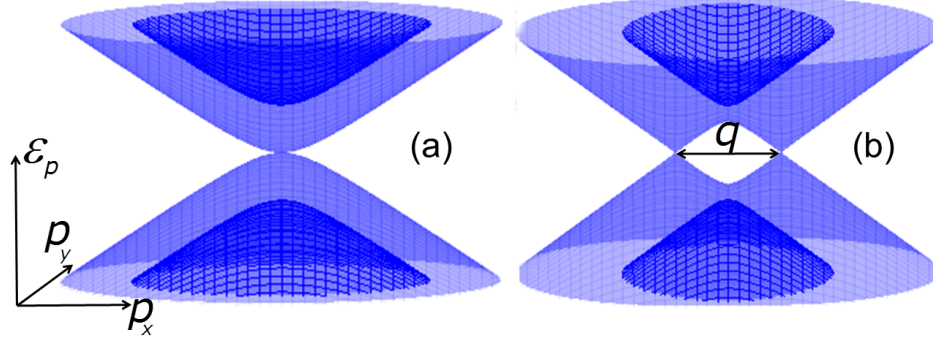


Figure 2.2: (a) The electron spectrum (2.4) of a graphene bilayer in zero magnetic field. (b) The spectrum (2.12) in a nonzero parallel magnetic field. The magnetic field splits the parabolic spectrum into the two Dirac cones. An exaggerated value $q = 5$ of the magnetic field parameter was utilized here.

Hamiltonian (2.2) has four eigenvalues

$$\varepsilon(\mathbf{p}) = \pm \frac{t_1}{2} \pm \sqrt{\frac{t_1^2}{4} + v_F^2 p^2}. \quad (2.4)$$

The well-known spectrum (2.4) is shown in Fig. 2.2(a). The spectrum consists of the four bands with the parabolic dispersion for small p .

2.2.2 Parallel magnetic field

Now let us introduce the in-plane magnetic field $\mathbf{B} = \hat{y}B$ applied along the y axis. We choose the gauge $\mathbf{A} = \hat{x}Bz$ and use the Peierls substitution

$$\mathbf{p} \rightarrow \mathbf{p} + e\mathbf{A}. \quad (2.5)$$

Here, we took into account the negative sign of the electron charge, so e corresponds to its absolute value. If the layer number is denoted by j , the in-plane electron momentum on the j -th layer changes to

$$\mathbf{p}_j = \mathbf{p} + j \Delta p \hat{\mathbf{x}}, \quad (2.6)$$

where Δp is

$$\Delta p = eBd, \quad \frac{\Delta p}{\hbar B} = 5 \times 10^3 \text{ cm}^{-1} \text{ T}^{-1}. \quad (2.7)$$

The momentum change Δp has the following physical meaning. When an electron tunnels between the layers, the Lorentz force $\mathbf{F} = -e[\mathbf{v} \times \mathbf{B}]$ changes the in-plane momentum by

$$\Delta p_x = \int F_x dt = eB_y \int v_z dt = eBd. \quad (2.8)$$

The change in the in-plane momentum results in the relative shift of the Dirac points on the different layers in the momentum space.

To simplify equations below, it is convenient to switch to the dimensionless variables

$$\frac{v_F \mathbf{p}}{t_1} \rightarrow \mathbf{p}, \quad \frac{v_F \Delta p}{t_1} \rightarrow q, \quad \frac{\varepsilon}{t_1} \rightarrow \varepsilon. \quad (2.9)$$

Here the parameter q is the dimensionless ratio of the ‘‘magnetic shift’’ $v_F \Delta p$ and

the interlayer tunneling amplitude t_1

$$q = \frac{v_F \Delta p}{t_1} = \frac{v_F}{t_1} (eBd) = 0.88 \times 10^{-3} B[\text{T}]. \quad (2.10)$$

The parameter q describes the orbital effect of the magnetic field in our model and will be frequently referred to as the magnetic field for shortness. It is worth noting that even for a strong magnetic field this parameter is small $q \ll 1$, e.g., $q = 0.044$ for $B = 50$ T.

Applying the Peierls substitution (2.6) to Hamiltonian (2.2) and switching to the dimensionless variables (2.9), we obtain

$$H = \begin{pmatrix} ((\mathbf{p} - \mathbf{q}) \cdot \boldsymbol{\sigma}) & I^A \\ I^A & (\mathbf{p} \cdot \boldsymbol{\sigma}^*) \end{pmatrix}. \quad (2.11)$$

Hamiltonian (2.11) has the following spectrum:

$$\varepsilon(\mathbf{p}) = \pm \frac{1}{\sqrt{2}} \sqrt{\mathbf{p}^2 + (\mathbf{p} - \mathbf{q})^2 + 1 \pm W}, \quad (2.12)$$

where

$$W = \sqrt{[(\mathbf{p} - \mathbf{q})^2 - \mathbf{p}^2]^2 + 2\mathbf{p}^2 + 2(\mathbf{p} - \mathbf{q})^2 + 1}. \quad (2.13)$$

In contrast to the parabolic dispersion (2.4), the spectrum (2.12) has two Dirac points separated by the magnetic shift q with a saddle point in between, as shown

in Fig. 2.2(b). Expanding Eq. (2.12) around one of the Dirac points

$$\varepsilon(\mathbf{p}) \approx \pm \frac{q}{\sqrt{1+q^2}} p, \quad (2.14)$$

we find that the slope of the Dirac cones is controlled by the magnetic field and is greatly reduced for $q \ll 1$.

A dispersion similar to Eq. (2.12) was found for the twisted graphene layers in Ref. [62], where the relative displacement of the two Dirac cones in the momentum space results from the spatial rotation of the layers

$$\Delta p_{\text{rot}}/\hbar = K_0 \Delta\phi = 6 \times 10^6 \text{ cm}^{-1}. \quad (2.15)$$

Here $\Delta\phi = 2^\circ$ is the twist angle, and $K_0 = 4\pi/3\sqrt{3}a$ is the distance between the Γ and K points in the reciprocal space. The saddle point between the two Dirac points results in the Van Hove singularity in the density of states, which was observed experimentally in electron tunneling in Ref. [63]. Comparing Eq. (2.7) with Eq. (2.15), we observe that the magnetic field effect is much weaker than the effect of twisting. Even for $B = 50 \text{ T}$, the magnetic shift is $\Delta p/\hbar = 2.5 \times 10^5 \text{ cm}^{-1}$ is much smaller than the rotational shift $\Delta p_{\text{rot}}/\hbar$.

2.3 Graphite

2.3.1 Model

Now we proceed to the discussion of graphene multilayers. First, we solve the problem for an infinite number of layers, i.e., for graphite, and then briefly mention the effect of a finite number of layers.

By analogy with the bilayer Hamiltonian (2.2), the Hamiltonian of graphite without magnetic field reads in the adopted units (2.9)

$$H = \begin{pmatrix} \ddots & & & & & & \\ & (\mathbf{p} \cdot \boldsymbol{\sigma}) & I^A & & & & \\ & I^A & (\mathbf{p} \cdot \boldsymbol{\sigma}^*) & I^A & & & \\ & & I^A & (\mathbf{p} \cdot \boldsymbol{\sigma}) & & & \\ & & & & \ddots & & \end{pmatrix}. \quad (2.16)$$

It acts on the vector

$$\Psi = (\cdots \tilde{\psi}_{j-1} \tilde{\psi}_j \tilde{\psi}_{j+1} \cdots), \quad \tilde{\psi}_j = (\psi_j^A \psi_j^B), \quad (2.17)$$

where the subscript j denotes the layer number, and the superscripts A and B denote sublattices.

Using the momentum representation in the z direction and introducing the corresponding momentum k (in addition to the in-plane momentum \mathbf{p}), we transform

Hamiltonian (2.16) into a 4×4 matrix similar to the graphene bilayer Hamiltonian

(2.2)

$$H = \begin{pmatrix} (\mathbf{p} \cdot \boldsymbol{\sigma}) & 2I^A \cos k \\ 2I^A \cos k & (\mathbf{p} \cdot \boldsymbol{\sigma}^*) \end{pmatrix}. \quad (2.18)$$

Hamiltonian (2.18) has the following spectrum

$$\varepsilon_{1,2}(\mathbf{p}, k) = \pm \cos k + \sqrt{\cos^2 k + p^2}, \quad (2.19)$$

$$\varepsilon_{3,4}(\mathbf{p}, k) = \pm \cos k - \sqrt{\cos^2 k + p^2}. \quad (2.20)$$

The subscripts (1,2) and (3,4) denote positive and negative energies, whereas the subscripts (1,3) and (2,4) correspond to the terms $\pm \cos k$. Because the spectrum has the electron-hole symmetry, we consider only the positive energies $\varepsilon_{1,2}$. The branches 1 and 2 are equivalent, in the sense that $\varepsilon_1(\mathbf{p}, k + \pi) = \varepsilon_2(\mathbf{p}, k)$. Thus, it is sufficient to consider only one branch ε_1 , which is plotted in Fig. 2.3. Since the off-diagonal elements of Hamiltonian (2.18) vanish for $k = \pi/2$, the dispersion has the Dirac-type form $\varepsilon_1(\mathbf{p}, \pi/2) = p$ for $k = \pi/2$, as shown in Fig. 2.3.

2.3.2 Parallel magnetic field

2.3.2.1 Semiclassical analysis

In the presence of a magnetic field, electrons move along the isoenergetic surfaces in the momentum space. For the field $\mathbf{B} = \hat{y}B$ along the y direction, the electron orbits lie on the intersections of the isoenergetic surfaces of the disper-

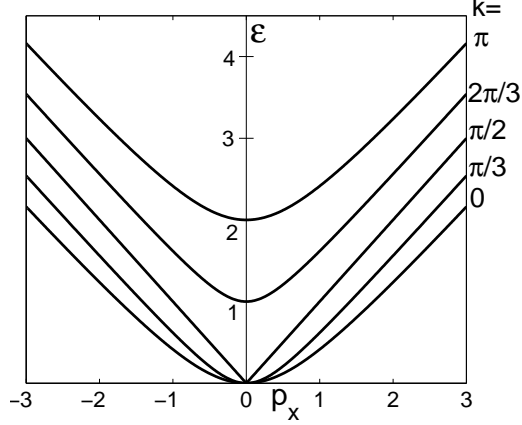


Figure 2.3: Spectrum $\varepsilon_1(\mathbf{p}, k)$ (2.19) of Hamiltonian (2.18) for $p_y = 0$. Each curve corresponds to a given value of the out-of-plane momentum k indicated on the right. The axes are given in the adopted dimensionless units (2.9).

sion (2.19) and the planes parallel to the (p_x, k) plane. The cross-sections of the isoenergetic surfaces $\varepsilon_1(\mathbf{p}, k) = \varepsilon = \text{const}$ with the (p_x, k) plane at $p_y = 0$ are shown in Fig. 2.4. The arrows indicate the direction of electron motion.

Topology of the electron orbits changes with the increase of the energy ε . The isoenergetic surfaces for the dispersion (2.19) are closed for $0 < \varepsilon < 2$, so the orbits are closed too, see Fig. 2.4(a). Thus, based on the Onsager quantization rule [64], the spectrum is discrete for this energy interval. However, at the critical energy $\varepsilon = 2$, the isoenergetic surfaces reconnect, as shown in Fig. 2.4(b), and become open for $\varepsilon > 2$, resulting in the open orbits shown in Fig. 2.4(c). Open semiclassical orbits lead to a continuous energy spectrum.

Fig. 2.4 shows only the electron orbits for $p_y = 0$ and $\varepsilon > 0$. We can find the topology of the electron orbits and the character of the spectrum for an arbitrary p_y , which is a good quantum number for the magnetic field along the y direction.

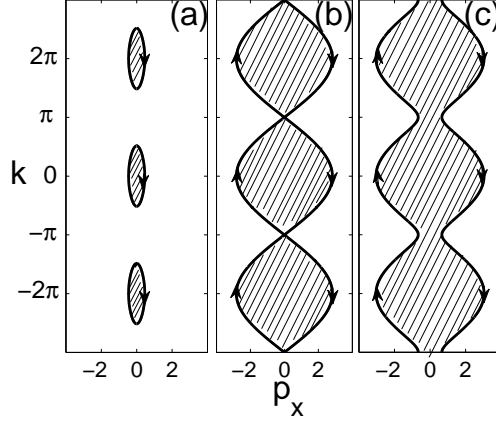


Figure 2.4: Semiclassical electron orbits in the momentum space for the in-plane magnetic field along the y axis. Only the orbits with $p_y = 0$ are shown. They are obtained by intersecting the (p_x, k) plane with the isoenergetic surfaces $\varepsilon_1(\mathbf{p}, k) = \varepsilon$ for (a) $\varepsilon = 0.1$, (b) $\varepsilon = 2$, (c) $\varepsilon = 2.2$. The orbits are (a) closed for $|\varepsilon| < 2$ and (c) open for $|\varepsilon| > 2$.

The orbits are open, so the spectrum is continuous in p_x for

$$\varepsilon^2 - 2|\varepsilon| > p_y^2. \quad (2.21)$$

The orbits are closed, so the spectrum is discrete and degenerate in p_x for

$$\varepsilon^2 - 2|\varepsilon| < p_y^2 < \varepsilon^2 + 2|\varepsilon|. \quad (2.22)$$

There are no orbits and no states for

$$p_y^2 > \varepsilon^2 + 2|\varepsilon|. \quad (2.23)$$

The domains of the continuous and discrete spectra, defined by the inequalities

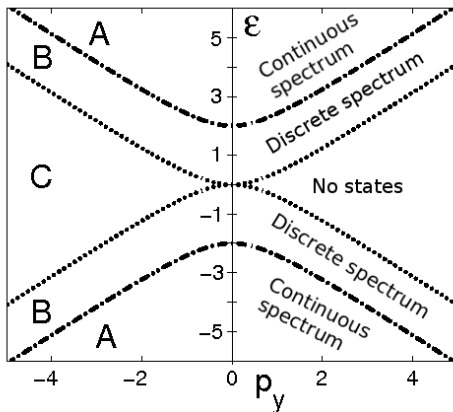


Figure 2.5: Domains of the continuous and discrete spectra in the (p_y, ε) plane. The dashed-dotted and dotted curves represent solutions of the equations $\varepsilon^2 - 2|\varepsilon| = p_y^2$ and $\varepsilon^2 + 2|\varepsilon| = p_y^2$. The spectrum is continuous in the region A defined by Eq. (2.21), discrete in the region B defined by Eq. (2.22), and there are no states in the region C defined by Eq. (2.23).

(2.21), (2.22), and (2.23), are shown in Fig. 2.5 in the (p_y, ε) plane.

2.3.2.2 Mathieu equation

Now we present a more formal and exact analysis of the electron spectrum in a parallel magnetic field. Applying the Peierls substitution (2.6) in the dimensionless units

$$\mathbf{p}_j = \mathbf{p} + j\mathbf{q}, \quad \mathbf{q} = \hat{x}q \quad (2.24)$$

to Hamiltonian (2.16), we obtain

$$H = \begin{pmatrix} \ddots & & & & & \\ & (\mathbf{p}_{j-1} \cdot \boldsymbol{\sigma}) & I^A & & & \\ & I^A & (\mathbf{p}_j \cdot \boldsymbol{\sigma}^*) & I^A & & \\ & & I^A & (\mathbf{p}_{j+1} \cdot \boldsymbol{\sigma}) & & \\ & & & & \ddots & \end{pmatrix}. \quad (2.25)$$

The eigenvalue problem $H\Psi = \varepsilon\Psi$ for H (2.25) and Ψ (2.17) reads in components

$$I^A(\tilde{\psi}_{j-1} + \tilde{\psi}_{j+1}) + [\boldsymbol{\sigma}^{(*)} \cdot (\mathbf{p} + j\mathbf{q}) - \varepsilon] \tilde{\psi}_j = 0. \quad (2.26)$$

Here, $\boldsymbol{\sigma}^{(*)}$ denotes $\boldsymbol{\sigma}$ for even j and $\boldsymbol{\sigma}^*$ for odd j . The matrix equation (2.26) represents a set of two equations. One of them relates ψ_j^B and ψ_j^A on the same layer and has the simple form

$$\psi_j^B = \frac{p_x \pm ip_y + jq}{\varepsilon} \psi_j^A, \quad (2.27)$$

where the signs \pm correspond to even and odd j . Using Eq. (2.27), we algebraically eliminate ψ_j^B components in Eq. (2.26) and reduce it to the simpler equation

$$\psi_{j+1}^A + \psi_{j-1}^A = \left(\varepsilon - \frac{(\mathbf{p} + j\mathbf{q})^2}{\varepsilon} \right) \psi_j^A, \quad (2.28)$$

which has the same form for even and odd j . From now on we drop the superscripts

A. In the Fourier representation

$$\psi_j = \int_0^{2\pi} \psi(k) e^{ikj} dk, \quad (2.29)$$

Eq. (2.28) becomes

$$\left(\frac{d}{dk} - i \frac{p_x}{q} \right)^2 \psi(k) - V(k) \psi(k) = 0, \quad (2.30)$$

where

$$V(k) = \frac{2\varepsilon}{q^2} \cos k - \frac{\varepsilon^2 - p_y^2}{q^2}. \quad (2.31)$$

Here, $\psi(k)$ is a 2π -periodic, twice-differentiable function $\psi(k) = \psi(k + 2\pi)$. To further simplify Eq. (2.30), we introduce the function $\phi(k)$

$$\psi(k) = e^{ik(p_x/q)} \phi(k), \quad (2.32)$$

which eliminates the term ip_x/q from Eq. (2.30) and reduces it to the angular Mathieu equation for $\phi(k)$

$$\frac{d^2 \phi(k)}{dk^2} - V(k) \phi(k) = 0. \quad (2.33)$$

Eq. (2.33) is equivalent to the Schrödinger equation for a particle moving in the 1D potential $V(k)$ (2.31). The variables ε and p_y are the parameters that control $V(k)$.

Since $V(k)$ is periodic in k , the Bloch theorem can be applied, so the solutions

of Eq. (2.33) have the form

$$\phi_\kappa(k) = e^{ik\kappa} u_\kappa(k). \quad (2.34)$$

Here, κ is the quasimomentum in the space reciprocal to the k space, and $u_\kappa(k)$ is a 2π -periodic function in k . From Eqs. (2.32) and (2.34) and the periodicity requirement for $\psi(k)$, we select the solutions of Eq. (2.33) with $\kappa = -p_x/q$. Since the solutions of Eq. (2.33) are periodic in the quasimomentum $\phi_{\kappa+1}(k) = \phi_\kappa(k)$, the parameter ε in Eq. (2.30) must be periodic in p_x : $\varepsilon(p_x) = \varepsilon(p_x + q)$. Therefore, the magnetic field effectively introduces the magnetic Brillouin zone in p_x with the period q .

We have reduced the original eigenvalue problem (2.28) to the convenient differential equation (2.33). Different regimes for its solutions are controlled by the parameters p_y and ε . If the criterion (2.22) is satisfied, the 1D classical motion is bounded by the barriers of $V(k)$, as shown in Fig. 2.6(a) for $\varepsilon = 0.1$ and $p_y = 0$. Then the energy spectrum is discrete. On the other hand, if the criterion (2.21) is satisfied, the potential is negative $V(k) < 0$ for any k , as shown in Fig. 2.6(b) for $\varepsilon = 2.1$ and $p_y = 0$. Then the motion of a particle is unbounded, and the spectrum is continuous in p_x . The first regime corresponds to the closed orbits in Fig. 2.4(a), and the second regime to the open orbits in Fig. 2.4(c). In the following sections, we use the approaches of both Sec. 2.3.2.1 and this section to obtain and interpret the results.

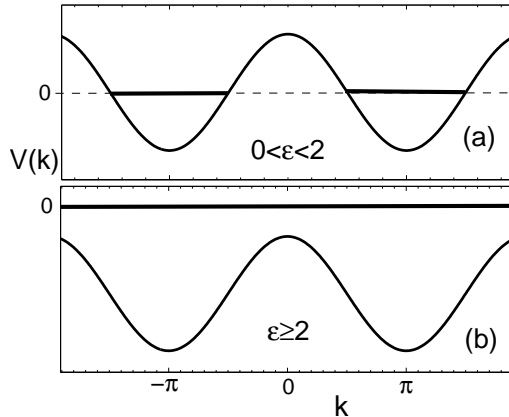


Figure 2.6: The plots of $V(k)$ (2.31) for $p_y = 0$. The cases of $\varepsilon = 0.1$ and $\varepsilon = 2.1$ are shown on the panels (a) and (b). The classically permitted region corresponds to $V(k) < 0$, as indicated by the thick horizontal line. Thus, the panels (a) and (b) represent bounded and unbounded motion.

2.3.2.3 Closed orbits

In this section, we study the electron spectrum in the domain of the (p_y, ε) plane defined by the criterion (2.22) and labeled by the letter B in Fig. 2.5. In this case, the classical motion of a particle in the 1D potential (2.31) is restricted to the potential wells separated by the barriers, as shown in Fig. 2.6(a). The height of the barriers is

$$h(p_y, \varepsilon) = \max[V(k)] = \frac{\varepsilon(2 - \varepsilon) + p_y^2}{q^2}. \quad (2.35)$$

The barriers $h(p_y, \varepsilon) \gg 1$ are high everywhere, except at the boundary of the domain (2.22). Thus, we can neglect tunneling and use the WKB quantization rule

for a single well of $V(k)$

$$4 \int_{\arccos a}^{\pi} \sqrt{-2\varepsilon \cos k + \varepsilon^2 - p_y^2} dk = 2\pi \left(n + \frac{1}{2} \right) q, \quad (2.36)$$

where

$$a = \frac{\varepsilon^2 - p_y^2}{2\varepsilon}. \quad (2.37)$$

The integral on the left-hand side of Eq. (2.36) is proportional to the area enclosed by the electron orbit in momentum space, see Fig. 2.4(a). Thus, Eq. (2.36) is equivalent to the Onsager quantization rule in a magnetic field [64]. Using the incomplete elliptic function of the second kind

$$E(\phi, m) = \int_0^{\phi} \sqrt{1 - m^2 \sin^2 \alpha} d\alpha, \quad (2.38)$$

Eq. (2.36) can be written as

$$\begin{aligned} & 8\sqrt{2\varepsilon}\sqrt{1+a} E \left(\frac{\pi + 2 \arcsin a}{4}, \sqrt{\frac{2}{1+a}} \right) \\ &= 2\pi \left(n + \frac{1}{2} \right) q. \end{aligned} \quad (2.39)$$

Eqs. (2.39) and (2.37) implicitly define $\varepsilon_n(p_x, p_y)$ as a function of p_y and n for a given magnetic field q , and the spectrum is degenerate in p_x .

To check validity of the WKB approximation, we diagonalize of the original Hamiltonian (2.25) numerically and compare results with the solutions of Eq. (2.39). Momentum dependences of $\varepsilon_n(p_x, 0)$ and $\varepsilon_n(0, p_y)$ are shown in Figs. 2.7(a) and (b)

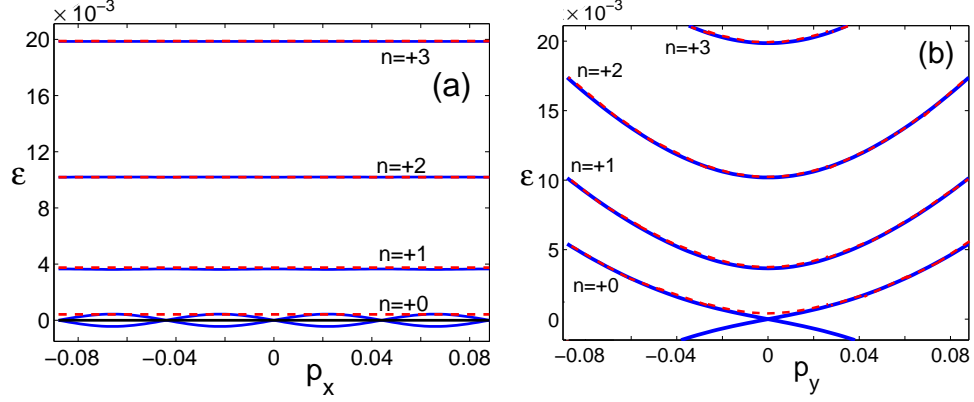


Figure 2.7: Low-energy levels $\varepsilon_n(p_x, p_y)$ for $q = 0.044$. Panel (a) shows $\varepsilon_n(p_x, 0)$ vs p_x for $p_y = 0$, and panel (b) shows $\varepsilon_n(0, p_y)$ vs p_y for $p_x = 0$. Solid lines represent exact numerical diagonalization of Hamiltonian (2.25). Dashed lines represent the WKB analytical approximation (2.39). All quantities are presented in the adopted dimensionless units (2.9).

for a few lowest energy levels at $q = 0.044$. The analytical approximation (2.39) agrees well with the numerical results for $n \neq 0$. The discrete energy levels shown in Fig. 2.7(a) are degenerate in p_x and represent the Landau levels in a parallel magnetic field. However, the $n = 0$ level has a remarkable dispersion in p_x . Similarly to the spectrum of the graphene bilayer in Fig. 2.2(b), the $n = 0$ level consists of a series of the Dirac cones shifted by the vector q . This dispersion cannot be obtained from the approximate WKB equation (2.39), because of the divergence at $\varepsilon = 0$ in the original equations (2.27) and (2.28).

Fig. 2.7(b) shows that the energy levels $\varepsilon_n(0, p_y)$ have a quadratic dispersion in p_y , except for the $n = 0$ level. Given the degeneracy in p_x , the energy levels $\varepsilon_n(p_x, p_y)$ form one-dimensional bands in p_y , so the density of states diverges at the bottom points $\varepsilon_n(p_x, 0)$ of the bands. These singularities in the density of state can be detected experimentally by electron tunneling or optical spectroscopy. The

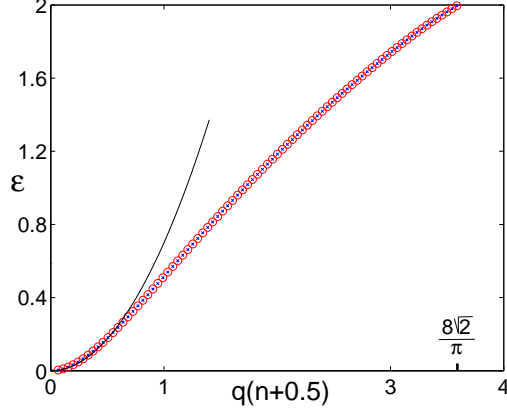


Figure 2.8: Energy levels $\varepsilon_n(0,0)$ vs the quantum number n at $p_x = 0$ and $p_y = 0$ for $q = 0.044$. The horizontal axis shows the combination $q(n + 1/2)$. The circles represent solutions of the WKB equation (2.39), and the small points inside the circles represent numerical data. The quadratic approximation (2.41) is shown by the solid line. All quantities are presented in the adopted dimensionless units (2.9).

energies $\varepsilon_n(0,0)$ are plotted in Fig. 2.8 in the interval $0 < \varepsilon < 2$ vs the combination $q(n + 1/2)$ appearing in Eq. (2.39). Depending on the magnetic field q , a different number n_{\max} of the discrete levels fills the curve. By setting $\varepsilon = 2$ in Eq. (2.36), we obtain

$$n_{\max} + \frac{1}{2} = \frac{8\sqrt{2}}{\pi q} = \frac{3.6}{q}. \quad (2.40)$$

For example, for $q = 0.044$, we have $n_{\max} = 81$ levels, which are depicted by circles in Fig. 2.8.

For small ε and $p_y = 0$, we find from Eq. (2.39)

$$\varepsilon_n = \frac{\pi^2}{32E^2 \left(\frac{\pi}{4}, \sqrt{2}\right)} q^2 \left(n + \frac{1}{2}\right)^2 = 0.7 q^2 \left(n + \frac{1}{2}\right)^2. \quad (2.41)$$

We observe that the energies (2.41) depend quadratically on the level number n

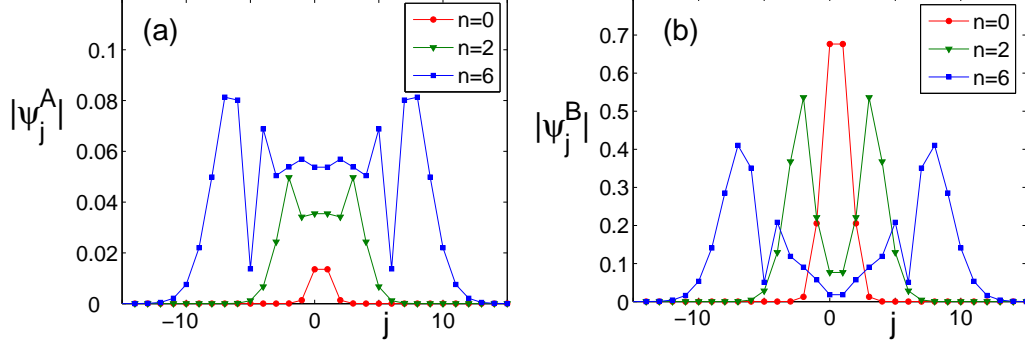


Figure 2.9: The absolute values of the wave functions $|\psi_j^A|$ and $|\psi_j^B|$ on the sublattices A and B vs the layer number j for $q = 0.044$, $p_x = q/2$, and $p_y = 0$. The variable n denotes the energy level number.

and the magnetic field q . This dependence is different from the usual Landau level dependence, where the energies are linear in the field and in the quantum number. The reason for the unusual dependence in our case is the following. For small ε , the semiclassical orbit in Fig. 2.4(a) shrinks to a thin ellipsoid of the length π in the k direction and the width $\sqrt{2\varepsilon}$ in the p_x direction. Thus, the area enclosed by the semiclassical orbit is proportional to $\sqrt{\varepsilon}$, so the Onsager quantization rule gives quadratic dependence of the energy on the magnetic field and the level number n . The quadratic approximation (2.41) is shown by the solid line in Fig. 2.8 and works well in the region $\varepsilon < 0.1$.

Fig. 2.9 shows the plots of $|\psi_j^A|$ and $|\psi_j^B|$ vs the layer number j for several energy levels n . We observe that the magnetic field causes localization of the wave function on a finite number of layers. According to Eq. (2.27), the wave functions for the low energy levels ε_n are localized predominantly on the sublattice B. The magnitudes of $|\psi_j^A|$ and $|\psi_j^B|$ are shown by different vertical scales in panels (a) and

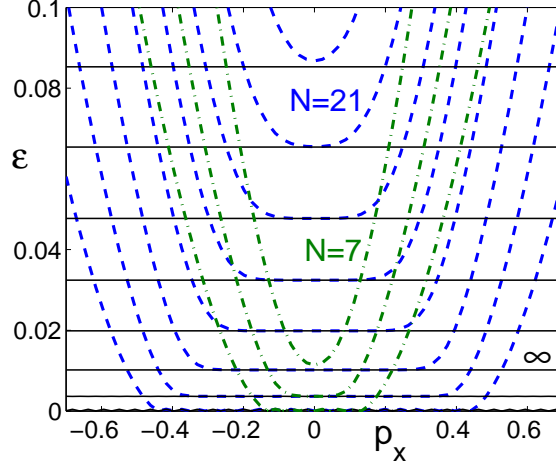


Figure 2.10: Energy spectrum $\varepsilon_n(p_x, 0)$ vs p_x at $p_y = 0$ and $q = 0.044$ for the system with a finite number of layers N . The dashed-dotted, dashed, and solid lines correspond to $N = 7, 21,$ and ∞ . All quantities are presented in the adopted dimensionless units (2.9).

(b) of Fig. 2.9.

Now let us briefly discuss the spectrum of a finite system with the total number of layers N . Fig. 2.10 shows $\varepsilon_n(p_x, 0)$ for $N = 7, 21,$ and ∞ . The degeneracy in p_x is lifted for a finite number of layers, but, with increasing N , the spectrum approaches to that of the infinite system with $N = \infty$. Indeed, if the localization length for a particular energy level is shorter than the size of the system, the energy of the level is the same as for $N = \infty$. Thus, the results obtained for $N = \infty$ are applicable to a finite system with a sufficient large N .

2.3.2.4 Open orbits

Now we study the energy spectrum in the domain defined by Eq. (2.21) and labeled by the letter A in Fig. 2.5. It corresponds to the open electron orbits in

Fig. 2.4(c). In the Mathieu equation (2.33), the potential $V(k) < 0$ is negative for any k , so the motion is unbounded, as shown in Fig. 2.6(b). Then, the WKB solutions of Eq. (2.33) are

$$\phi(k) = e^{\pm iS(k)}, \quad S(k) = \int_0^k \sqrt{|V(k)|} dk, \quad (2.42)$$

where the signs \pm correspond to the direction of motion. Because of the periodicity requirement for $\psi(k)$ and Eq. (2.32), the phase accumulation in Eq. (2.42) over the period 2π must be equal to $-2\pi p_x/q$ plus an integer multiple of 2π . Thus we obtain the following quantization condition for the open orbits

$$qS(2\pi) = 2 \int_0^\pi \sqrt{-2\varepsilon \cos k + \varepsilon^2 - p_y^2} dk = \mp 2\pi(p_x + \tilde{n}q). \quad (2.43)$$

Here the integer \tilde{n} is different from the integer n in Eq. (2.36) and takes both negative and positive values. The sign of $p_x + \tilde{n}q$ corresponds to the two solutions in Eq. (2.42). Eq. (2.43) can be represented in terms of the elliptic integral (2.38)

$$4\sqrt{2\varepsilon}\sqrt{1+a} E\left(\frac{\pi}{2}, \sqrt{\frac{2}{1+a}}\right) = \mp 2\pi(p_x + \tilde{n}q), \quad (2.44)$$

where the parameter a is given by Eq. (2.37). In contrast to Eq. (2.39), Eq. (2.44) contains p_x , so the energy levels $\varepsilon_n(p_x, p_y)$ continuously depend on p_x .

The energy spectra obtained from Eqs. (2.39) and (2.44) are compared in Fig. 2.11 with the results of numerical diagonalization of Hamiltonian (2.25) around the critical energy $\varepsilon = 2$ for $p_y = 0$. For $\varepsilon < 2$, the spectrum consists of the energy

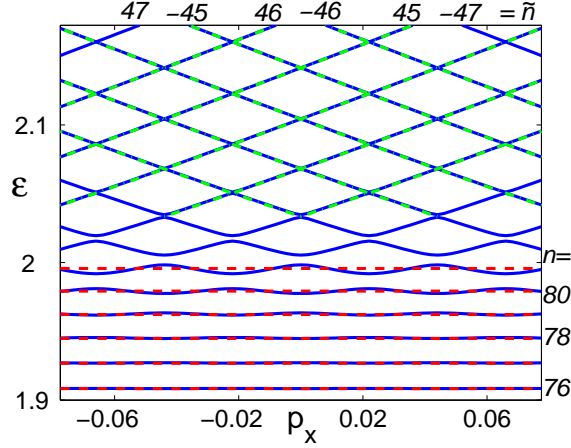


Figure 2.11: Energy spectrum around $\varepsilon = 2$ for $q = 0.044$ and $p_y = 0$. The solid lines are obtained by numerical diagonalization of Hamiltonian (2.25). The dashed lines, obtained from Eq. (2.39), are labeled by the integer n shown on the right. The dashed-dotted lines, obtained from Eq. (2.44), are labeled by the integer \tilde{n} shown at the top. This plot illustrates a transition from discrete to continuous spectrum. All quantities are presented in the dimensionless units (2.9).

levels degenerate in p_x , which are well described by the analytical approximation (2.39) for closed orbits. The corresponding level number n is shown on the right in Fig. 2.11. At the energy $\varepsilon = 2$, the spectrum undergoes a transition to the regime of continuous dispersion in p_x . For $\varepsilon > 2$, the spectrum consists of the two families of lines with the opposite slopes. This spectrum is well described by the analytical approximation (2.44) for open orbits. The corresponding number \tilde{n} labels the dispersion lines and takes both positive and negative values shown at the top in Fig. 2.11. Because the left-hand sides of Eqs. (2.39) and (2.44) differ by the factor of 2 at $\varepsilon = 2$ and $p_x = 0$, the numbers n and \tilde{n} are connected as $n \approx 2|\tilde{n}|$. The approximations (2.39) and (2.44) stop working in the vicinity of the critical energy $\varepsilon = 2$.

For a high energy ε , when the parameter a (2.37) is large, we can obtain the spectrum explicitly by expanding the square root in Eq. (2.42) for $S(k)$ in powers of $1/a$

$$S(k) = \frac{\sqrt{\varepsilon^2 - p_y^2}}{q} k - \frac{\varepsilon \sin k}{q\sqrt{\varepsilon^2 - p_y^2}}. \quad (2.45)$$

Then the quantization condition (2.43) gives

$$\sqrt{\varepsilon^2 - p_y^2} = \mp(p_x + \tilde{n}q), \quad (2.46)$$

which can be written as

$$\varepsilon_{\tilde{n}}^2 = (p_x + \tilde{n}q)^2 + p_y^2. \quad (2.47)$$

The spectrum Eq. (2.47) is the same as for decoupled graphene layers with the Peierls substitution (2.24).

Substituting the square root expression from Eq. (2.46) into Eq. (2.45), we obtain the approximate WKB wave functions (2.42) for $\varepsilon > 0$

$$\phi(k) = \exp \left(-i \frac{p_x + \tilde{n}q}{q} k + i \frac{\sqrt{(p_x + \tilde{n}q)^2 + p_y^2}}{q(p_x + \tilde{n}q)} \sin k \right). \quad (2.48)$$

Then, using Eq. (2.32), we calculate the Fourier transform (2.29) and find the wave function ψ_j in the direct space

$$\psi_j = J_{\tilde{n}-j} \left(\frac{\sqrt{(p_x + \tilde{n}q)^2 + p_y^2}}{q(p_x + \tilde{n}q)} \right). \quad (2.49)$$

Here $J_m(x)$ is the Bessel function of the m -th order of the first kind. For $p_y = 0$,

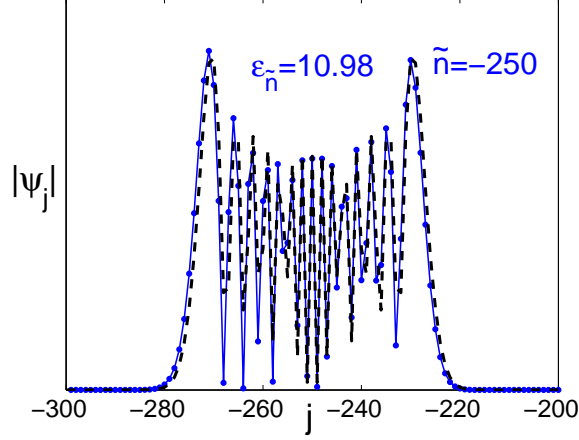


Figure 2.12: The absolute value of the wave function $|\psi_j|$ vs the layer number j for a state from the domain of continuous spectrum. The parameters of the plot are $\tilde{n} = -250$, $\varepsilon_{\tilde{n}} = 10.98$, $p_x = p_y = 0$, and $q = 0.044$. The solid and dashed lines represent exact numerical diagonalization of Hamiltonian (2.25) and the approximate analytical formula (2.50), respectively.

Eq. (2.49) simplifies to

$$\psi_j = J_{\tilde{n}-j} \left(\frac{\text{sign}(p_x + \tilde{n}q)}{q} \right). \quad (2.50)$$

The wave function (2.50) is centered at $j = \tilde{n}$, as shown in Fig. 2.12. We observe that, even though Eq. (2.47) coincides with the spectrum of effectively decoupled graphene layers, the corresponding wave function (2.50) is localized on a large number of layers proportional to $1/q$. Similar wave functions are known for the quasi-one-dimensional conductors in a magnetic field [59, 60].

2.4 Conclusions

In this Chapter, we have studied the orbital effect of a strong magnetic field applied in the y direction parallel to the layers of the graphene bilayer and multi-

layers. For the former, the magnetic field splits the parabolic bilayer dispersion into the two Dirac cones in the momentum space with the spacing proportional to the magnetic field. For the latter, we have found two domains in the parameter space with distinct energy spectra. In the low-energy domain, the semiclassical electron orbits are closed, so the spectrum is discrete and degenerate in p_x . The energy levels depends quadratically on p_y , thus forming a series of one-dimensional bands in p_y . The discrete energies of the bottoms of the bands are the analogs of the Landau levels but depend quadratically on the energy level number n and the magnetic field B . The $n = 0$ energy level around zero energy has unusual properties and consists of a series of shifted Dirac cones, similarly to the bilayer case. In the high-energy domain, the semiclassical electron orbits are open, so the spectrum is continuous in p_x , thus forming two-dimensional bands in p_x and p_y . For high enough energies, these bands evolve into the Dirac cones originating from different layers and shifted in the momentum space due to the applied magnetic field. In both regimes, the wave functions are localized on a finite number of layers. Mathematically, the problem reduces to the Mathieu equation. The WKB approximation for the semiclassical electron orbits in the momentum space in the magnetic field agrees well with exact numerical diagonalization, except for a few special cases, where the WKB approach is not applicable.

Chapter 3: Graphene multilayer in crossed electric and magnetic fields

3.1 Introduction

Now, let us generalize results of previous Chapter and study graphene multilayer in crossed electric and magnetic fields in the geometry shown in Fig. 3.1. The magnetic field $\mathbf{B} = B\hat{\mathbf{y}}$ is parallel to the layers, while the electric field $\mathbf{E} = E\hat{\mathbf{z}}$ is perpendicular, and the distance between the layers is d . We shall demonstrate that, when the resonance condition for the fields

$$E = vB \tag{3.1}$$

is achieved, the electronic wave functions become delocalized in the z direction. As before, parameter $v = 10^6$ m/s is the velocity of the two-dimensional Dirac electrons in graphene.

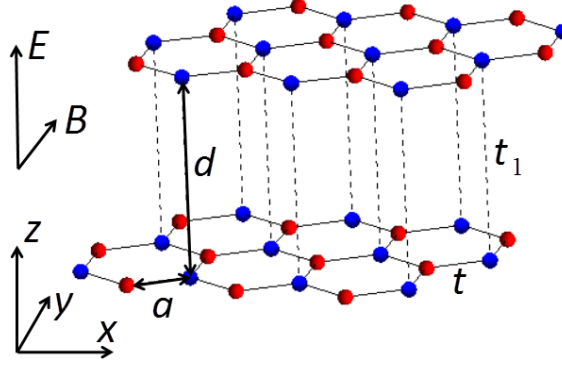


Figure 3.1: Schematic view of two graphene layers and the directions of the applied electric and magnetic field.

3.2 Hamiltonian and energy spectrum

3.2.1 Hamiltonian

We remind that the Lorentz force, due to the in-plane magnetic field B , induces a shift of the in-plane momentum on the n -th graphene layer by $p_x \rightarrow p_x - qn$, where $q = eBd$. If the electric field is uniform, it changes the potential energy on the n -th layer by un , where $u = eEd$. Thus, using Eq. (2.26) of previous Chapter, the Schrodinger equation of graphite in the crossed electric and magnetic fields is

$$v\sigma_x(p_x - qn)\Psi_n + t_1 I^A (\Psi_{n-1} + \Psi_{n+1}) = (\varepsilon - un)\Psi_n. \quad (3.2)$$

We remind that, σ_x acts on the spinor wave function $\Psi_n = (\psi_n^A \ \psi_n^B)^T$, which has components on both A and B sublattices of the n -th graphene layer. The matrix $I^A = (1 + \sigma_z)/2$ and the amplitude $t_1 = 0.4$ eV describe the interlayer coupling between the carbon atoms which lie on top of each other in the Bernal stacked

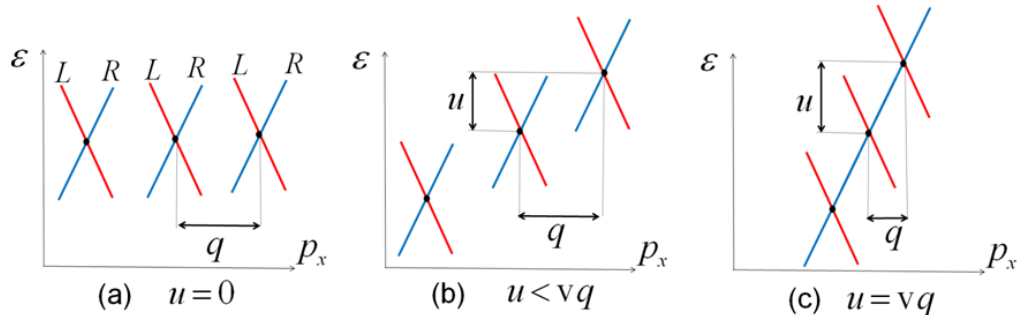


Figure 3.2: Schematic energy spectrum of graphite in the crossed magnetic and electric fields (represented by q and u) in the limit $t_1 \rightarrow 0$ at different values of u . (a) The Dirac cones have the same energy for zero electric field at $u = 0$. (b) With an increase of u , the Dirac cones shift vertically. (c) When the resonant condition $u = vq$ is met, the R-branches of the Dirac cones align and become degenerate.

graphite lattice. For simplicity, we set the y component of the in-plane momentum equal to zero $p_y = 0$, however all calculations can be easily generalized to the $p_y \neq 0$ case.

3.2.2 Weak coupling limit

In the limit of zero interlayer coupling $t_1 \rightarrow 0$, the spectrum is given by a series of Dirac cones

$$\varepsilon_m = \pm v(p_x - qm) + um, \quad (3.3)$$

which correspond to the wave functions localized on m -th graphene layer. The evolution of spectrum (3.3) with the increase of electric field is qualitatively illustrated in Fig. 3.2. Each Dirac cone consists of two branches corresponding to the left-moving and right-moving electrons, referred to as the L-movers and R-movers and

labeled in Fig. 3.2(a). For $u = 0$, the Dirac cones are shifted horizontally by q , as shown in Fig. 3.2(a). For $u \neq 0$, the Dirac cones also shift vertically as shown in Fig. 3.2(b). When fields E and H satisfy the resonant condition $u = qv$, which is equivalent to Eq. (3.1), the right-moving branches of the spectra align and become degenerate as shown in Fig. 3.2(c).

Next, let us perform a unitary transformation $\Psi_n = e^{-\frac{i\sigma_y\pi}{4}}\Psi'_n$ to the basis of the L and R movers $\Psi'_n = (\psi_n^R \ \psi_n^L)$. Then, the Schrodinger equation (3.2) becomes

$$v\sigma_z(p_x - qn)\Psi'_n + \frac{t_1}{2}(1 - \sigma_x)(\Psi'_{n-1} + \Psi'_{n+1}) = (\varepsilon - un)\Psi'_n. \quad (3.4)$$

Let us temporary neglect matrix σ_x , then Eq. (3.4) decouples for the R and L modes:

$$[vp_x + n(u - qv)]\psi_n^R + \frac{t_1}{2}(\psi_{n-1}^R + \psi_{n+1}^R) = \varepsilon\psi_n^R, \quad (3.5)$$

$$[vp_x + n(u + qv)]\psi_n^L + \frac{t_1}{2}(\psi_{n-1}^L + \psi_{n+1}^L) = \varepsilon\psi_n^L. \quad (3.6)$$

Solutions of Eqs. (3.5) and (3.6) can be enumerated by integer m , so that the eigenvalues are given by Eq. (3.3) and the eigenfunctions are

$$\psi_n^{R,L} = J_{n-m} \left(\frac{-t_1}{u \mp qv} \right), \quad (3.7)$$

where $J_m(x)$ is the Bessel function. The spectrum (3.3) is given by the two sets of curves $\varepsilon_m^R = vp_x + m(qv - u)$ and $\varepsilon_m^L = -vp_x + m(qv + u)$, which have linear dispersion in p_x . Notice that the R and L modes “feel” the effect of electric and

magnetic fields differently. The combination of electric and Lorentz forces shifts the linear dispersion by $(u - qv)$ for the R-movers and by $(u + qv)$ for the L-movers. This results not only in different spacing between the R and L modes in Eq. (3.3), but also in the different localization properties of the corresponding wave functions. The wave functions (3.7) are localized in the z direction on a finite number of layers of the order of $t_1/|u \mp qv|$. So, with an increase of electric field the L (R) movers become more (less) localized. At the resonance condition $u = qv$, which is equivalent to Eq. (3.1), the R-movers “feel” zero net force and become delocalized with their spectrum

$$\varepsilon^R = vp_x + t_1 \cos(k_z), \quad (3.8)$$

where the out-of-plane momentum k_z is a good quantum number.

3.2.3 Exact diagonalization

The numerically calculated spectrum of full Eq. (3.4) is shown in Fig. 3.3(a) and (b), whereas the corresponding wave functions are shown in Fig. 3.3(c) and (d). Although the detailed structure of the spectrum differs from the simple description given in Eq. (3.3), the general structure remains similar. For the case $u = 0$, $q \neq 0$ studied in Chapter , the spectrum was found to consist of discrete Landau levels within a window of energy $|\varepsilon| < 2t_1$ and a quasi-continuous spectrum outside this window $|\varepsilon| > 2t_1$. When a finite but non-resonant electric field $2u = qv = 0.2t_1$ is applied, the discrete Landau levels acquire dispersion in p_x as shown in Fig. 3.3(a). The quasi-continuous spectrum consists of a series of parallel lines corresponding to

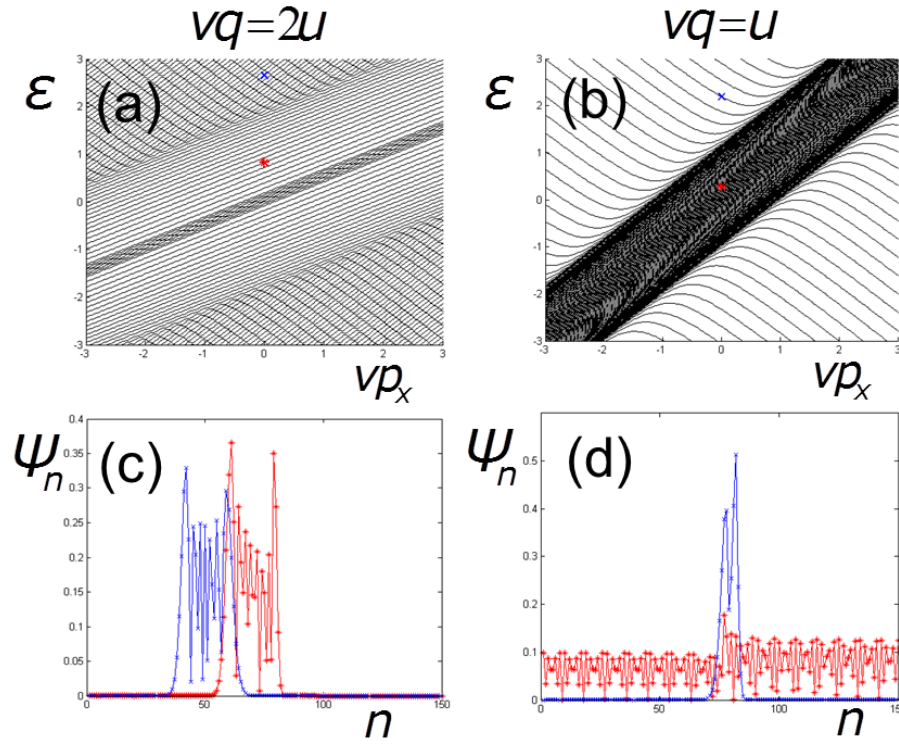


Figure 3.3: Numerically calculated energy spectrum and wave functions for a finite system of 150 layers. The top panels show the energy spectrum, whereas the bottom panels show the wave functions corresponding to the states marked with the “*” and “x” symbols in the top panels. The left and right columns correspond to the non-resonant $2u = qv = 0.2t_1$ and resonant $u = qv = 0.2t_1$ cases, respectively. The unit of energy scale corresponds to tunneling amplitude t_1 .

the L and R modes, well described by Eq. (3.3). The wave functions are localized in the z direction both for the discrete Landau levels and the quasi-continuous spectrum as shown in Fig. 3.3(c). However, when the resonance between the fields is achieved $u = qv = 0.2t_1$, the spectrum reconstructs dramatically, as shown in Fig. 3.3(b). A continuous band of the R-movers corresponding to spectrum (3.8) is formed and the eigenstates are delocalized as shown in Fig. 3.3(d). However, the L-movers remain well-localized.

3.3 Experiment and interpretation

3.3.1 Experimental results

Over the last decade, the interlayer tunneling spectroscopy was developed to measure the energy gap in high-temperature superconductors and charge-density wave materials [65, 66]. It was also used to study a magnetic field induced charge-density wave in NbSe₃ and graphite [67]. This effect has orbital origin and exists generally for fields oriented perpendicular to the highly conducting layers. In contrast, the interlayer tunneling in parallel magnetic field allows to extract the in-plane energy spectrum of the carriers in layers [68]. The tunneling experiments between two graphene sheets in the graphene/insulator/graphene heterostructure recently began [69, 70]. Let us briefly discuss a tunneling spectroscopy study of graphite mesa in a strong in-plane magnetic field done by a group of Professor Latyshev.

Mesa-type structures were fabricated by etching thin graphite flakes with a focused ion beam [71]. Mesa is shown schematically in Fig. 3.4. Current flows

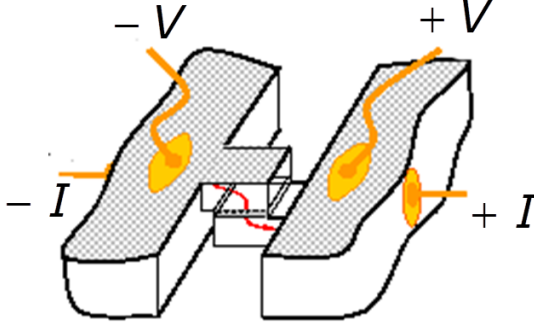


Figure 3.4: A schematic view of the mesa-type structure.

between the different sides of the crystal as shown in the figure. Owing to a high interlayer conductivity anisotropy ($\sigma_{\perp}/\sigma_{\parallel} \approx 10^4$ at low temperatures), the applied voltage drops mostly on the mesa. Mesa is typically of 1 micron size and contains a few tens of graphene layers. The experiment was performed in pulsed magnetic fields in National Laboratory of High Magnetic Fields in Toulouse. Figure 3.5(a) shows a set of $dI/dV(V)$ spectra for various in-plane magnetic fields. For magnetic field greater than 20 T, local maxima develop symmetrically for both polarities of the bias voltage. Both the magnitude and voltage V_0 of the peaks grow with the magnetic field H . Figure 3.5(b) shows that the dependence V_0 vs B is close to linear.

3.3.2 Discussion

We believe that the mechanism of the resonant delocalization of the wave functions in the crossed electric and magnetic field, discussed in Sec. 3.2, is responsible for the peaks in the differential conductance observed in the experiment. According to Eq. (3.1), the position of the conductance peak is proportional to the magnetic

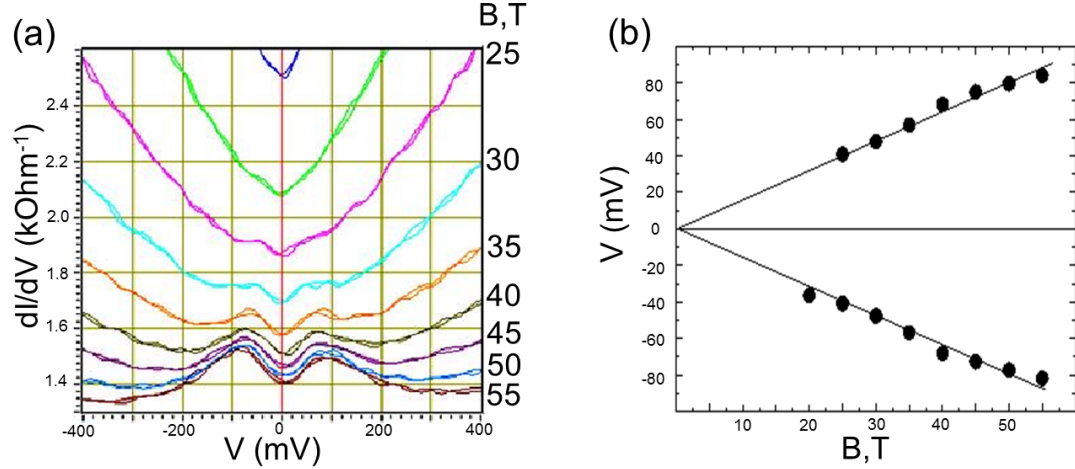


Figure 3.5: (a) Interlayer tunneling spectra of graphite mesa-structure at various in-plane magnetic fields (the magnitude of the field for each curve is indicated on the right). (b) Dependence of the position of the tunneling conductance peak on the in-plane magnetic field B .

field

$$E = V_0/l = vB, \quad (3.9)$$

where l is the effective length over which the applied voltage V_0 drops. Equation (3.9) is consistent with the experiment. Using Eq. (3.9) and the experimental data shown in Fig. 3.5(b), we extract $l = 1.2$ nm, which is about three times longer than the interlayer distance in graphite. This probably indicates that decoupling of the interlayer Bernal correlation occurs in 2 – 3 intrinsic tunnel junctions. In NbSe₃ mesas, it was demonstrated that charge density wave decoupling can occur within two intrinsic tunnel junctions of the mesa [71]. Although our theoretical model is developed for a large number of graphene layers, the resonant condition (3.1) is expected to be valid even for a few layers.

3.4 Conclusion

Interlayer tunneling spectra on graphite mesas at strong in-plane magnetic field B have a peak at voltage V_0 , which is proportional to the magnetic field B . The experimental result is consistent with a theoretical picture. Because of the 2D Dirac nature of electrons in graphene layers, the wave functions delocalize in the out-of-plane direction when the resonant condition between the fields $E = vB$ is achieved .

Chapter 4: Shockley edge states in topological insulators

4.1 Introduction

Theory of topological surface states has been studied in a number of works both in the tight-binding [9, 72] and continuous models [73–77]. Many papers focused on the bulk-boundary correspondence, i.e., on proving that a sample with non-trivial topological numbers in the bulk should possess gapless excitations on the surface. The method of topological invariants, although being very powerful, is often not physically transparent and not intuitive about the exact mechanism by which the topological numbers are related to the surface states.

In this Chapter, we show that the surface states in TIs can be understood based on the Shockley model also discussed in Chapter 1.1.1. The Shockley model was also applied to surface states in topological superconductors [11]; however, we focus only on surface states in semiconductors. In Sec. 4.2, we review once more the 1D Shockley model and show how the Shockley criterion can be formulated in terms of a topological winding number for the off-diagonal matrix element of the bulk Hamiltonian, thus connecting bulk properties with the surface states as discussed in Refs. [8, 9, 78–81]. In Sec. 4.3.1, we generalize the model to 3D by replacing atoms by the 2D layers parallel to the xy plane and assigning the in-

plane momentum dependence $\mathbf{p} = (p_x, p_y)$ to the interlayer tunneling amplitudes t_1 and t_2 . In Sec. 4.3.3, we study vortex lines in the 3D momentum space [82, 83], where the off-diagonal matrix element of the bulk Hamiltonian vanishes. We show that the projection of the 3D vortex lines onto the 2D in-plane momentum space encircles the domain where the surface states exist. We observe that the tight-binding TI Hamiltonians studied in Refs. [19, 20, 22, 72] have the Shockley-model structure and can be understood using our approach. In Sec. 4.4.1, we illustrate the Shockley mechanism for the Fu-Kane-Mele model on the diamond lattice [20]. We show how the surface states evolve when the parameters of the Hamiltonian vary. In Sec. 4.4.2, we show that reconnection of the vortex lines represents a phase transition in the TI Hamiltonian. The spiral vortex lines correspond to a phase with an even number of Dirac cones (the “weak” TI phase), while the circular vortex lines correspond to a phase with an odd number of Dirac cones (the “strong” TI phase). In Sec. 4.5, we apply the Shockley model to describe the surface states in Bi_2Se_3 , which is formed by the quintuple layers of Bi and Se [73, 74, 84–87]. The electronic structure of this material near the Fermi level can be well described by the hybridized p_z orbitals located near the outer layers of the quintuplets [74, 84]. Thus, the Shockley model with the intra-quintuplet and inter-quintuplet tunneling amplitudes t_1 and t_2 gives a plausible description of this material. Surface states have complementary properties depending on how the crystal is terminated [84]. Breaking the t_2 amplitude introduces a cut between the quintuplets. In this case, the surface states have a Dirac cone in the Brillouin zone (BZ) center [85, 86]. Breaking t_1 introduces a cut inside the quintuplet. In this case, the Shockley model predicts the

surface states with the Dirac cones on the boundary of the BZ. The similar effect was considered for the $\text{Bi}_{1-x}\text{Sb}_x$ alloy in Ref. [88]. In Sec. 4.5.2, we discuss whether a continuous approximation for the TI Hamiltonian gives a good description of the surface states. We conclude that the tight-binding models are better suitable for the description of the surface states. Then, in Sec. 4.6, we generalize the Shockley model by including additional tight-binding amplitudes. For all these models, we find that the edge state is always localized on one sublattice, which is rarely mentioned in the TI literature.

4.2 1D Shockley model

4.2.1 The original Shockley model

In this section, we briefly review the Shockley model [1, 3] and its properties. Let us consider a 1D linear chain of atoms shown in Fig 4.1(a). The unit cell contains two atoms labeled as A and B, which are connected via the alternating nearest-neighbor complex tight-binding amplitudes t_1 and t_2 . So, the Hamiltonian of the model is

$$H = \sum_z \Psi^\dagger(z) [U\Psi(z) + V\Psi(z-1) + V^\dagger\Psi(z+1)], \quad (4.1)$$

$$U = \begin{pmatrix} 0 & t_1^* \\ t_1 & 0 \end{pmatrix}, \quad V = \begin{pmatrix} 0 & t_2^* \\ 0 & 0 \end{pmatrix}. \quad (4.2)$$

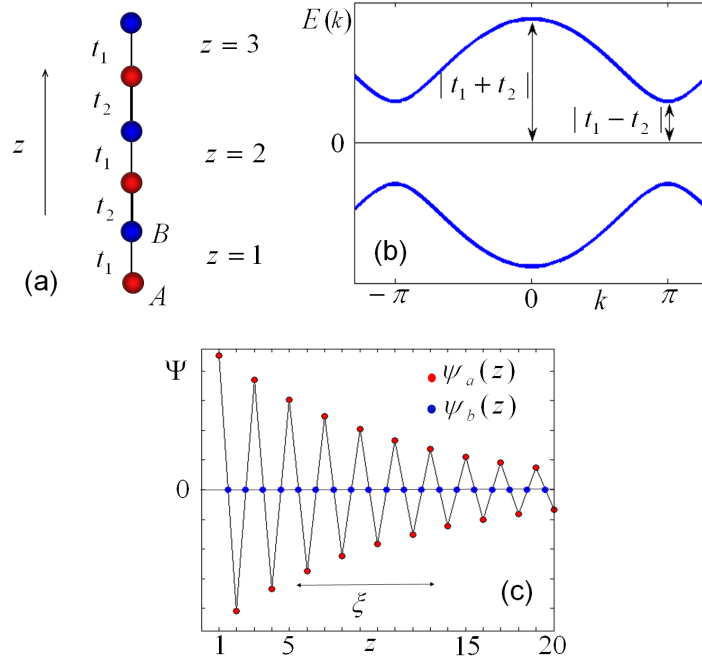


Figure 4.1: Panel (a): 1D chain of atoms with alternating tunneling amplitudes t_1 and t_2 representing the Shockley model, Eq. (4.1). Panel (b): The bulk energy spectrum of the system, Eq. (4.8), with a non-zero gap for $|t_1| \neq |t_2|$. Panel (c): The exponentially decaying edge state, Eq. (4.18), for $|t_1|/|t_2| < 1$ with the penetration depth $\xi = 1/\ln|t_2/t_1|$.

Here, z is the integer coordinate of the unit cell, t_1 and t_2 are the intra-cell and the inter-cell tunneling amplitudes, and $\Psi(z)$ is the spinor

$$\Psi(z) = \begin{pmatrix} \psi_a(z) \\ \psi_b(z) \end{pmatrix}, \quad (4.3)$$

where $\psi_a(z)$ and $\psi_b(z)$ are the wave functions on the sites A and B . In the Fourier representation $\Psi(z) = \int_0^{2\pi} \frac{dk}{2\pi} e^{ikz} \Psi(k)$, the Hamiltonian is

$$H = \int_0^{2\pi} \frac{dk}{2\pi} \Psi^\dagger(k) H(k) \Psi(k), \quad (4.4)$$

where

$$H(k) = U + V e^{-ik} + V^\dagger e^{ik} = \begin{pmatrix} 0 & t^*(k) \\ t(k) & 0 \end{pmatrix} \quad (4.5)$$

is a 2×2 matrix acting in the AB sublattice space, and

$$t(k) = t_1 + t_2 e^{ik} = t_1 + t_2 q, \quad q = e^{ik}. \quad (4.6)$$

Then, the Schrödinger equation

$$\begin{pmatrix} 0 & t^*(k) \\ t(k) & 0 \end{pmatrix} \begin{pmatrix} \psi_a \\ \psi_b \end{pmatrix} = E \begin{pmatrix} \psi_a \\ \psi_b \end{pmatrix} \quad (4.7)$$

gives two particle-hole symmetric energy bands with the eigenvalues $E(k)$ and eigenfunctions $\Psi(k)$

$$E(k) = \pm |t(k)|, \quad (4.8)$$

$$\Psi(k) = \frac{1}{\sqrt{2}} \begin{pmatrix} e^{i \arg[t(k)]} \\ \pm 1 \end{pmatrix}. \quad (4.9)$$

The energy spectrum has a gap if $|t_1| \neq |t_2|$, as illustrated in Fig. 4.1(b) for real t_1 and t_2 . Notice that the bulk wave function (4.9) has equal probabilities on both sublattices. In contrast, as we shall see below, the wave function of an edge state is localized only on one sublattice.

A boundary to the 1D lattice can be introduced by cutting either t_1 or t_2 link. Let us consider a half-infinite system for $z \geq 1$, $z = 1, 2, 3, \dots$, corresponding to the cut of the t_2 link. In this case, the atom A is exposed on the edge, as shown in Fig. 4.1(a). Mathematically, the boundary condition is introduced by requiring that the wave function vanishes at the fictitious site $z = 0$ and at infinity

$$\psi_a(0) = 0, \quad \psi_b(0) = 0, \quad (4.10)$$

$$\psi_a(+\infty) = 0, \quad \psi_b(+\infty) = 0. \quad (4.11)$$

It is shown in Appendix A.1 that the edge state can exist only for $E = 0$. So, we substitute $E = 0$ into Eq. (4.7) and find that the wave functions on the A and B

sublattices decouple

$$t(k) \psi_a = (t_1 + t_2 e^{ik}) \psi_a = 0, \quad (4.12)$$

$$t^*(k) \psi_b = (t_1^* + t_2^* e^{-ik}) \psi_b = 0, \quad (4.13)$$

where k is now a complex wave-number, so $t^*(k)$ is not a complex conjugate of $t(k)$.

In the real space, Eq. (4.13) can be written as a recursion relation

$$\psi_b(z) t_1^* + \psi_b(z-1) t_2^* = 0 \quad (4.14)$$

for $z \geq 1$. Using this recursion relation and the boundary condition $\psi_b(0) = 0$, we find that $\psi_b(z)$ vanishes for $z \geq 1$. In contrast, the real-space representation of Eq. (4.12)

$$\psi_a(z) t_1 + \psi_a(z+1) t_2 = 0 \quad (4.15)$$

for $z \geq 1$ does not involve $\psi_a(0)$ from Eq. (4.10). So, the solution on the A sublattice is

$$\psi_a(z) = q_0^{z-1}, \quad (4.16)$$

where, q_0 is obtained by solving the equation $t(k_0) = 0$, following from Eq. (4.12) for a complex wave-number k_0

$$q_0 = e^{ik_0} = -\frac{t_1}{t_2}. \quad (4.17)$$

Depending on whether $|q_0| < 1$ or $|q_0| > 1$, the solution in Eq. (4.16) either satisfies

the condition (4.11) at infinity or not. If $|t_2| > |t_1|$, then $|q_0| < 1$, as shown in Fig. 4.2(a), and the wave function (4.16) exponentially decays at $z \rightarrow +\infty$, as shown in Fig. 4.1(c), so the edge state exists. In contrast, if $|t_1| > |t_2|$, then $|q_0| > 1$, as shown in Fig. 4.2(b), and the wave function (4.16) exponentially grows at $z \rightarrow +\infty$, so an edge state does not exist. To summarize, by solving Eqs. (4.12) and (4.13) with the appropriate boundary conditions (4.10) and (4.11), we obtain the zero-energy edge state

$$\Psi_0(z) = \begin{pmatrix} 1 \\ 0 \end{pmatrix} q_0^{z-1}, \quad E_0 = 0, \quad (4.18)$$

which exists only if

$$|q_0| = \frac{|t_1|}{|t_2|} < 1. \quad (4.19)$$

Equation (4.19) constitutes the Shockley Criterion: *In the 1D tight-binding model with alternating tunneling amplitudes given by Hamiltonian (4.1), the edge state exists if the bond of the greater magnitude is broken at the boundary.*

Let us now consider an alternative formulation of the Shockley criterion (4.19) in terms of the winding number

$$W = \frac{1}{2\pi i} \int_0^{2\pi} dk \frac{d}{dk} \ln t(k). \quad (4.20)$$

The winding number W represents the phase change of the complex function $t(k)$ when the real variable k changes from 0 to 2π . The function $t(k)$ also defines a closed contour

$$C' = \{t(k) = t_1 + t_2 e^{ik}, k \in (0, 2\pi)\} \quad (4.21)$$

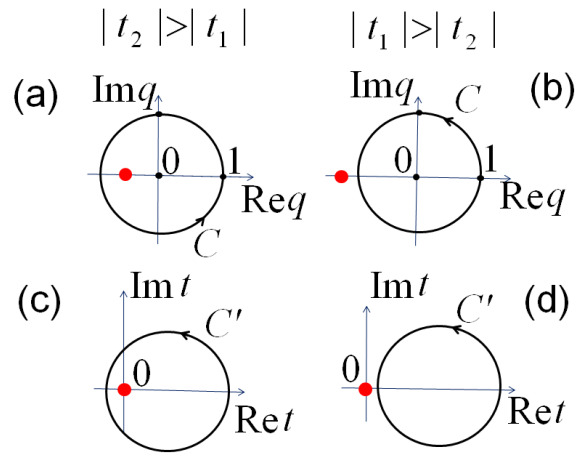


Figure 4.2: Topological formulation of the Shockley criterion (4.19). Panels (a) and (b) compare the two cases, where the root q_0 (the red dot) lies inside or outside the unit circle $C = \{q = e^{ik}, k \in (0, 2\pi)\}$. An edge state exists for $|q_0| < 1$, panel (a), and does not exist for $|q_0| > 1$, panel (b). An alternative formulation in terms of the winding number (4.20) is illustrated in panels (c) and (d). The edge state exists if the winding number is non-zero, panel (c), and does not exist if the winding number is zero, panel (d).

in the 2D plane of $(\text{Re } t, \text{Im } t)$, as shown in Fig. 4.2, panels (c) and (d). If $|q_0| < 1$, or equivalently $|t_2| > |t_1|$, the contour C' winds around the origin (red dot), as shown in panel (c). If $|q_0| > 1$, or equivalently $|t_1| > |t_2|$, the contour C' does not wind around the origin, as shown in panel (d). So, the Shockley criterion (4.19) can be formulated in terms of the winding number

$$W = \begin{cases} 1, & \text{edge state exists,} \\ 0, & \text{edge state does not exist.} \end{cases} \quad (4.22)$$

This formulation was discussed in a number of papers [8, 9, 80, 81]. While the winding number (4.20) is calculated using the off-diagonal element $t(k)$ of the Hamiltonian (4.5), it can be equivalently expressed through the eigenfunctions $\Psi(k)$ defined in Eq. (4.9)

$$W_Z = \frac{1}{\pi i} \int_0^{2\pi} dk \Psi^\dagger(k) \partial_k \Psi(k). \quad (4.23)$$

This expression is called the Zak phase [8] (up to π in the denominator and related to the Berry phase) and is an alternative representation of the winding number (4.20).

4.2.2 On-site energies in the 1D Shockley model

Let us further generalize the model and include on-site energies ε_a and ε_b in Hamiltonian (4.5)

$$H(k) = \begin{pmatrix} \varepsilon_a & t^*(k) \\ t(k) & \varepsilon_b \end{pmatrix}, \quad (4.24)$$

As shown in Eq. (4.18) for $\varepsilon_a = \varepsilon_b = 0$, the edge state solution is localized on the A sublattice. Therefore, adding the on-site energy ε_a simply shifts the energy of the edge state without changing its wave function irrespective of ε_b . So, if criterion (4.19) is satisfied, the edge state is localized on the A sublattice and has the energy

$$E_0 = \varepsilon_a. \quad (4.25)$$

It is also convenient to transform the Hamiltonian to the symmetrized form H

$$H(k) = \frac{\varepsilon_a + \varepsilon_b}{2} + \begin{pmatrix} h & t^*(k) \\ t(k) & -h \end{pmatrix}, \quad h = \frac{\varepsilon_a - \varepsilon_b}{2}. \quad (4.26)$$

The offset $(\varepsilon_a + \varepsilon_b)/2$ just uniformly shifts all energies and will be omitted below, so the Hamiltonian becomes

$$H(k) = \begin{pmatrix} h & t^*(k) \\ t(k) & -h \end{pmatrix}. \quad (4.27)$$

The bulk spectrum of the Hamiltonian (4.27) is generally gapped

$$E(k) = \pm \sqrt{h^2 + |t(k)|^2}. \quad (4.28)$$

By denoting the Pauli matrices acting in the AB sublattice space as $\boldsymbol{\tau} =$

(τ_x, τ_y, τ_z) , Hamiltonian (4.27) can be written as

$$H(k) = \boldsymbol{\tau} \cdot \mathbf{d}(k), \quad \mathbf{d}(k) = [\text{Ret}(k), \text{Imt}(k), h]. \quad (4.29)$$

When k changes from 0 to 2π , the vector $\mathbf{d}(k)$ traces a closed contour Γ in the corresponding 3D space. The criterion (4.22) is equivalent to the following statement: The edge state exists if the projection of the contour Γ onto the xy plane encloses the origin [9]. Note that the Zak phase (4.23) is equal to $W_Z = \Omega/2\pi$, where Ω is the solid angle of the contour Γ viewed from the origin. For $h = 0$, the contour Γ lies in the xy plane, so $\Omega = 2\pi$ and $W_Z = 1$. However, for $h \neq 0$, the contour Γ lies off the xy plane, and Ω is a fraction of 2π . So, in general, the Zak phase W_Z is fractional and does not give a number of the edge states, whereas the criterion (4.22) remains applicable.

4.3 3D Shockley-like model

4.3.1 Generalization to the 3D case

Let us generalize Hamiltonian (4.27) to the 3D case. Instead of alternating atomic sites, let us consider a sequence of alternating layers A and B perpendicular to the z direction, as shown on Fig. 4.3. Now, all parameters of Hamiltonian (4.27)

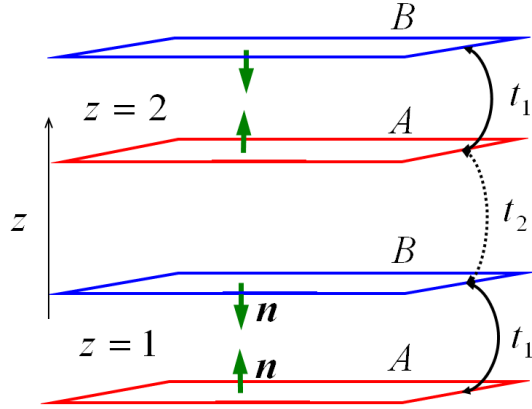


Figure 4.3: 3D generalization of the Shockley model described by Hamiltonian (4.30) with $h(\mathbf{p})$ defined by Eq. (4.33). The arrows show the staggered direction of the Rashba vector \mathbf{n} .

acquire dependence on the in-plane momentum $\mathbf{p} = (p_x, p_y)$

$$H = \begin{pmatrix} h(\mathbf{p}) & t^*(k, \mathbf{p}) \\ t(k, \mathbf{p}) & -h(\mathbf{p}) \end{pmatrix}. \quad (4.30)$$

The off-diagonal matrix element

$$t(k, \mathbf{p}) = t_1(\mathbf{p}) + t_2(\mathbf{p})e^{ik} \quad (4.31)$$

describes the \mathbf{p} -dependent inter-layer tunneling amplitudes, while $h(\mathbf{p})$ represents the intra-layer Hamiltonian. We denote the in-plane momentum as $\mathbf{p} = (p_x, p_y)$ and the out-of-plane momentum in the z direction as k ¹.

For a fixed value of the in-plane momentum \mathbf{p} , Hamiltonian (4.30) reduces to

¹Note that this notation is different from the $(\mathbf{k} \cdot \mathbf{p})$ method in the literature.

the 1D model (4.27), for which the edge state was studied in Sec. 4.2. The surface states exist for those in-plane momenta \mathbf{p} where criterion (4.19) is satisfied. The surface states are localized on the A sublattice, and the energy spectrum $E_0(\mathbf{p})$ of the surface states is determined by the in-plane Hamiltonian $h(\mathbf{p})$

$$E_0(\mathbf{p}) = h(\mathbf{p}). \quad (4.32)$$

In our construction of the generalized Shockley model, we put a restriction that the diagonal element $h(\mathbf{p})$ does not depend on k . Physically, it means that tunneling amplitudes connect only different sublattices A and B, but not A to A or B to B. Thus, Hamiltonian (4.30) is not the most general 3D Hamiltonian, however it applies to many models in the literature.

4.3.2 Spin-orbit interaction

So far, we have not considered spin of the electron. After including the spin variable in Hamiltonian (4.30), the terms $h(\mathbf{p})$ and $t(k, \mathbf{p})$ become 2×2 matrices acting in the spin-1/2 space, and the full Hamiltonian becomes a 4×4 matrix. We assume that $t(k, \mathbf{p})$ is proportional to the unit 2×2 matrix, but $h(\mathbf{p})$ may include the Pauli matrices $\boldsymbol{\sigma}$ acting on the spin variable. In vicinity of the time-reversal-invariant momentum point $\mathbf{p} = 0$, the Hamiltonian $h(\mathbf{p})$ must be bilinear in \mathbf{p} and the spin-Pauli matrices $\boldsymbol{\sigma}$. For example, $h(\mathbf{p})$ can have the Rashba spin-orbit coupling form

$$h(\mathbf{p}) = v(\sigma_x p_y - \sigma_y p_x) = v(\boldsymbol{\sigma} \times \mathbf{p}) \cdot \hat{z}, \quad (4.33)$$

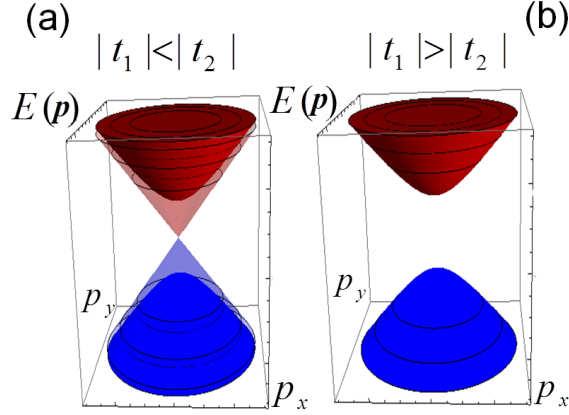


Figure 4.4: Energy spectrum of the 3D Shockley model described by Hamiltonian (4.30) in the vicinity of $\mathbf{p} = 0$. The spectrum of the bulk states, Eq. (4.35), is shown by the solid parabolas in both panels. According to the Shockley criterion, surface states exist if $|t_1| < |t_2|$, panel (a), and do not exist otherwise, panel (b). The surface states have the linear dispersion, Eq. (4.34), shown by the transparent Dirac cone in panel (b).

where v has the dimension of velocity. Notice that the diagonal term $\pm h(\mathbf{p})$ in Hamiltonian (4.30) has opposite signs on the A and B sublattices. This corresponds to staggered direction of the Rashba vector $\mathbf{n} = \pm \hat{z}$ on different layers for the spin-orbit coupling $v\mathbf{n}(\boldsymbol{\sigma} \times \mathbf{p})$ as shown in Fig. 4.3. In the vicinity of $\mathbf{p} = 0$, let us also approximate $t_1(\mathbf{p}) \approx t_1(0)$ and $t_2(\mathbf{p}) \approx t_2(0)$ and assume that $|t_1(0)| \neq |t_2(0)|$. Then, the surface states exist only if $|t_1(0)| < |t_2(0)|$, and the spectrum of the surface states has linear dependence on $|\mathbf{p}|$

$$E_0(\mathbf{p}) = \pm v|\mathbf{p}|, \quad (4.34)$$

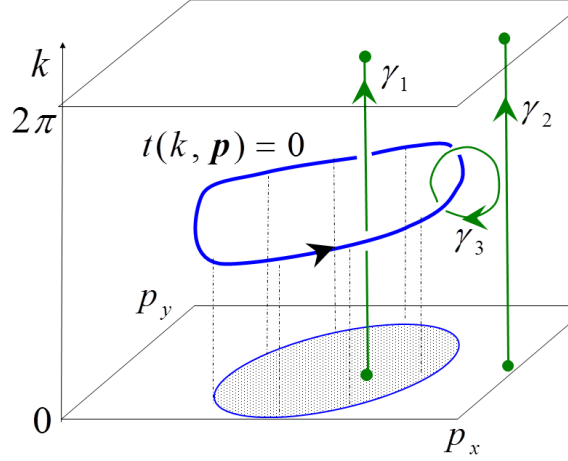


Figure 4.5: The thick blue curve is a vortex line in the 3D momentum space defined by Eq. (4.36). Its projection onto the 2D momentum space \mathbf{p} defines the boundary of the shaded area, where the surface states exist.

which is illustrated by the Dirac cone in panel (a) of Fig. 4.4. The wave functions of the surface states have in-plane spin-polarization perpendicular to the momentum \mathbf{p} . On the other hand, the bulk spectrum is parabolic in the vicinity of $\mathbf{p} = 0$

$$E^2(k, \mathbf{p}) = |t(k, 0)|^2 + v^2 \mathbf{p}^2, \quad (4.35)$$

as shown in both panels of Fig. 4.4 by solid colors. Note that, because of the assumption $|t_1(0)| \neq |t_2(0)|$, the off-diagonal element $t(k, \mathbf{p})$ is non-zero in the vicinity of $\mathbf{p} = 0$ and so the bulk spectrum (4.35) is gapped. On the other hand, if $|t_1(0)| = |t_2(0)|$, the bulk spectrum is gapless, and the Hamiltonian undergoes the topological phase transition, as will be shown in Sec. 4.4.

4.3.3 Vortex lines in 3D momentum space

In principle, the tunneling amplitudes $t_1(\mathbf{p})$ and $t_2(\mathbf{p})$ may depend on the in-plane momentum \mathbf{p} . So, the surface state existence criterion can only be satisfied in a certain domain of the 2D momentum space \mathbf{p} . In this section, we discuss how to identify this domain for the Hamiltonian (4.30).

Let us consider the equation

$$t(k, \mathbf{p}) = 0 \tag{4.36}$$

for the complex function $t(k, \mathbf{p})$ in Eq. (4.31). It is equivalent to two equations $\text{Re } t(k, \mathbf{p}) = 0$ and $\text{Im } t(k, \mathbf{p}) = 0$, which define a line in the 3D momentum space (k, \mathbf{p}) . In general, the complex-valued function $t(k, \mathbf{p})$ has a phase circulation around the line where it vanishes, i.e. Eq. (4.36) defines a vortex line in the 3D momentum space [78, 82, 83]. As an example, such a vortex line and its projection on the 2D momentum space \mathbf{p} are shown in Fig. 4.5. Phase winding of the function $t(k, \mathbf{p})$ along an arbitrary contour γ can be calculated as

$$W(\gamma) = \frac{1}{2\pi i} \oint_{\gamma} d\mathbf{l} \frac{d}{d\mathbf{l}} \ln t(k, \mathbf{p}), \tag{4.37}$$

where the notation $\mathbf{l} = (k, \mathbf{p})$ is used for brevity. For instance, the phase winding along the contour γ_3 around the vortex line in Fig. 4.5 is non-zero

$$W(\gamma_3) = 1. \tag{4.38}$$

Because the BZ is periodic in k , we can also define a closed contour by varying $0 < k < 2\pi$ for a fixed value of the in-plane momentum \mathbf{p} . Such contours γ_1 and γ_2 are shown in Fig. 4.5, and the phase windings (4.37) are well defined for these contours. The contours γ_1 and $-\gamma_2$ can be merged into the contour γ_3 . So, the following equation holds

$$W(\gamma_3) = W(\gamma_1) - W(\gamma_2). \quad (4.39)$$

Given Eq. (4.38) and the condition (4.22) that $W(\gamma_{1,2}) \geq 0$, we find that the winding numbers are $W(\gamma_1) = 1$ and $W(\gamma_2) = 0$. Since a non-zero winding number is required for existence of the surface states according to Eq. (4.22), we conclude that the surface states exist for the 2D momenta \mathbf{p} in the shaded area of Fig. 4.5 and do not exist outside. Thus, we have shown that the projection of the vortex line (4.36) onto the 2D momentum space \mathbf{p} defines the domain where the surface states exist.

While the main focus of this work is the 3D systems, let us comment on the 2D case $\mathbf{l} = (k, p_x)$, where p_x and k are the momenta parallel and perpendicular to the edge of the 2D system. The 2D case can also be viewed as a slice of 3D momentum space shown in Fig. 4.5 at a fixed momentum p_y . Then, the solution of the equation $t(k, p_x) = 0$ generally defines a set of vortex points in the 2D momentum space \mathbf{l} . Similarly to the 3D case, a projection of the vortex points onto the p_x momentum space identifies a domain in p_x for which the edge states exist. This method was used in Ref. [8] to find the edge states in graphene ribbons.

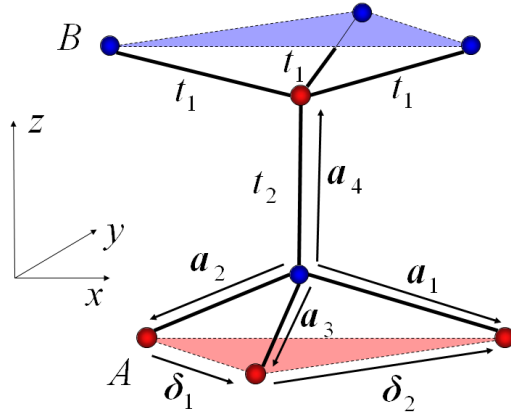


Figure 4.6: Illustration of the diamond crystal structure and the tight-binding model described by Hamiltonian (4.41). The lattice has two atoms in a unit cell shown by the red (A) and blue (B) spheres.

4.4 Diamond Model

4.4.1 Hamiltonian and surface states

In this section, we illustrate how the Shockley model can be applied to study the surface states for a particular TI model of Ref. [20]. However similar approach can be applied to other models [19, 22, 72].

Let us consider a tight-binding model on the diamond lattice shown in Fig. 4.6. The diamond lattice has two equivalent atom positions denoted by A (red) and B (blue). Atoms of each type form 2D triangular lattices, so that the A and B layers alternate along the z direction similarly to Fig. 4.3. The nearest A and B layers form a distorted graphene lattice. So, when viewed along the z direction, the structure looks like the ABC-stacked graphite lattice. We define the nearest-neighbor vectors

\mathbf{a}_n , $n = 1, 2, 3, 4$, as shown in Fig. 4.6, as well as the vectors

$$\begin{aligned}\boldsymbol{\delta}_1 &= \mathbf{a}_3 - \mathbf{a}_2 = (1/2, -\sqrt{3}/2), \\ \boldsymbol{\delta}_2 &= \mathbf{a}_1 - \mathbf{a}_3 = (1/2, \sqrt{3}/2), \\ \boldsymbol{\delta}_3 &= \mathbf{a}_2 - \mathbf{a}_1 = (-1, 0),\end{aligned}\tag{4.40}$$

which are the in-plane elementary translation vectors of the unit length $|\boldsymbol{\delta}_n| = 1$.

The Hamiltonian of the model has the form of Eq. (4.30)

$$H = \begin{pmatrix} h(\mathbf{p}) & t^*(k, \mathbf{p}) \\ t(k, \mathbf{p}) & -h(\mathbf{p}) \end{pmatrix},\tag{4.41}$$

where the unit cell consists of the A and B atoms connected by the vector \mathbf{a}_3 . The off-diagonal part

$$t(k, \mathbf{p}) = t_1(\mathbf{p}) + t_2 e^{ik},\tag{4.42}$$

$$t_1(\mathbf{p}) = t_1(1 + e^{-i\mathbf{p}\boldsymbol{\delta}_1} + e^{i\mathbf{p}\boldsymbol{\delta}_2}),\tag{4.43}$$

describes the nearest-neighbor tunneling between the A and B sublattices with the amplitude t_1 along the vectors \mathbf{a}_n , $n = 1, 2, 3$, and the amplitude t_2 along the vector \mathbf{a}_4 ². In Eqs. (4.42) and (4.43), we distinguish between the in-plane-momentum-dependent function $t_1(\mathbf{p})$ and the tight-binding amplitude t_1 . Equation (4.43) de-

²For the diamond model, the variable k is the momentum along the translation vector $\mathbf{a}_4 - \mathbf{a}_3$.

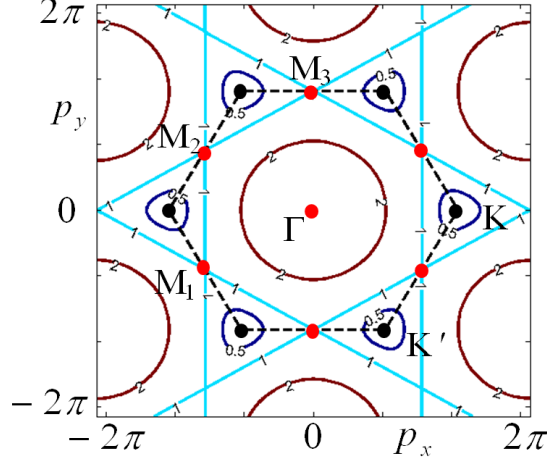


Figure 4.7: Lines of constant value for the graphene spectrum function $|t_1(\mathbf{p})|/|t_1| = C$, for $C = 0.5, 1, 2$, within the Brillouin zone (BZ), denoted by the dashed lines. The contour lines degenerate to points at the BZ corners (K and K' points) at $C = 0$ and at the BZ center at $C = 3$. The thick red dots denote the time-reversal-invariant momenta points (4.47).

describes the well-known tight-binding spectrum of graphene [14]

$$|t_1(\mathbf{p})|/|t_1| = \sqrt{3 + 2 \cos(\mathbf{p}\delta_1) + 2 \cos(\mathbf{p}\delta_2) + 2 \cos(\mathbf{p}\delta_3)} \quad (4.44)$$

The contour plots of $|t_1(\mathbf{p})|/|t_1| = C$, for $C = 0.5, 1, 2$, are shown in Fig. 4.7.

Note that $t_1(\mathbf{p})$ has the linear Dirac-like dependence on the momentum \mathbf{p} at the BZ corners, K and K' points in Fig. 4.7.

The diagonal term $h(\mathbf{p})$ in Hamiltonian (4.41) describes the spin-orbit interaction [20]

$$h(\mathbf{p}) = \frac{2\sqrt{2}}{3} \Lambda_{\text{SO}} \sum_{i,j,l=1,2,3} \epsilon_{ijl} (\boldsymbol{\sigma} \cdot [\mathbf{a}_i \times \mathbf{a}_j]) \sin(\mathbf{p}\delta_l), \quad (4.45)$$

where Λ_{SO} is the strength of the spin-orbit coupling, and ϵ_{ijl} is the antisymmetric

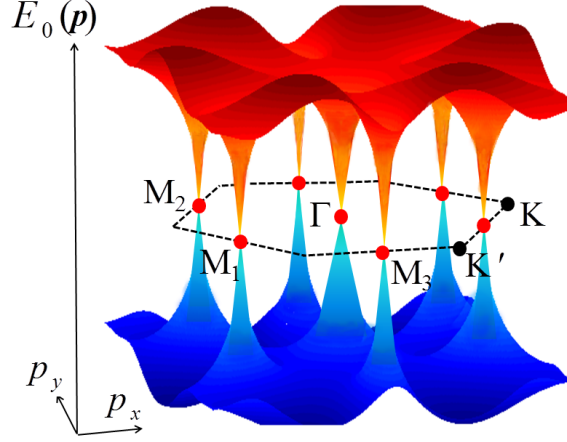


Figure 4.8: The plot of the particle-hole symmetric spectrum $E_0(\mathbf{p})$, Eq. (4.46), induced by the spin-orbit Hamiltonian $h(\mathbf{p})$ (4.45). In the vicinity of the time reversal invariant points, shown with the thick red dots, the Hamiltonian (4.45) becomes linear in momentum. The dashed line denotes the boundary of the BZ.

tensor. For simplicity, we do not include the inter-layer spin-orbit coupling involving the vector \mathbf{a}_4 in Hamiltonian (4.45), unlike in Ref. [20]. Hamiltonian (4.45) has a gapless particle-hole symmetric spectrum $E_0(\mathbf{p}) = \pm\sqrt{h^2(\mathbf{p})}$,

$$\begin{aligned}
 E_0^2(\mathbf{p})/\Lambda_{\text{SO}}^2 &= h^2(\mathbf{p})/\Lambda_{\text{SO}}^2 & (4.46) \\
 &= \sin(\mathbf{p}\boldsymbol{\delta}_1)\sin(\mathbf{p}\boldsymbol{\delta}_2) + \sin(\mathbf{p}\boldsymbol{\delta}_1)\sin(\mathbf{p}\boldsymbol{\delta}_3) + \sin(\mathbf{p}\boldsymbol{\delta}_2)\sin(\mathbf{p}\boldsymbol{\delta}_3) + \sum_{j=1,2,3} \sin^2(\mathbf{p}\boldsymbol{\delta}_j),
 \end{aligned}$$

which is shown in Fig. 4.8. The energy $E_0(\mathbf{p})$ vanishes at the four time-reversal-invariant momenta (TRIM)

$$\mathbf{p}_* \in \{\Gamma, M_1, M_2, M_3\}, \quad (4.47)$$

where Γ is the BZ center, and M_1, M_2, M_3 are at the centers of the BZ boundary, as shown in Figs. 4.7 and 4.8. Hamiltonian (4.45) is bilinear in the momentum and spin operators in the vicinity of the TRIM points

$$\frac{h(\mathbf{p} + \mathbf{p}_*^{(\Gamma)})}{\Lambda_{\text{SO}}} \approx \frac{\sqrt{3}}{2}(\sigma_x p_y - \sigma_y p_x), \quad (4.48)$$

$$\frac{h(\mathbf{p} + \mathbf{p}_*^{(M_3)})}{\Lambda_{\text{SO}}} \approx -\frac{\sqrt{3}}{2}\sigma_x p_y - \frac{1}{2\sqrt{3}}\sigma_y p_x - \frac{2\sqrt{2}}{\sqrt{3}}\sigma_z p_x. \quad (4.49)$$

Thus, the energy spectrum $E_0(\mathbf{p})$ has the shape of the Dirac cones in the vicinity of TRIM points, as shown in Fig. 4.8. It is important to distinguish the linear, Dirac-like, behavior of the off-diagonal term $t_1(\mathbf{p})$ in the vicinity of the BZ corners (K and K' points) and of the diagonal term $h(\mathbf{p})$ in the vicinity of the TRIM points, which are different sets of points in the BZ.

The bulk spectrum of Hamiltonian (4.41)

$$E^2(k, \mathbf{p}) = |t(k, \mathbf{p})|^2 + E_0^2(\mathbf{p}), \quad (4.50)$$

contains contributions from both the diagonal $h(\mathbf{p})$ and the off-diagonal $t(k, \mathbf{p})$ terms. The bulk spectrum becomes gapless when both contributions vanish for some momenta (k, \mathbf{p})

$$E_0(\mathbf{p}) = 0, \quad (4.51)$$

$$t(k, \mathbf{p}) = 0. \quad (4.52)$$

Given Eq. (4.42), Eq. (4.52) is equivalent to

$$|t_1(\mathbf{p})| = |t_2|, \quad (4.53)$$

which defines a contour line in Fig. 4.7. Conditions (4.51) and (4.52) can be satisfied simultaneously only for special values of the parameters t_1 and t_2 . The bulk spectrum becomes gapless, for $|t_2| = |t_1|$, when the contour line (4.53) passes through the TRIM points M_1, M_2, M_3 , and for $|t_2| = 3|t_1|$, when it passes through the Γ point.

	t_2 broken	t_1 broken	TI
$0 < t_2 < t_1 $	—	$M_{1,2,3}, \Gamma$	Weak
$ t_1 < t_2 < 3 t_1 $	$M_{1,2,3}$	Γ	Strong
$3 t_1 < t_2 $	$M_{1,2,3}, \Gamma$	—	Weak

Table 4.1: The table shows the points in the BZ where the surface states exist depending on the parameters of the model and which bond is broken at the surface. According to Fig. 4.8, the surface states have the Dirac cones at the corresponding points. Letters M_1, M_2, M_3, Γ denote positions of the TRIM points (4.47).

Hamiltonian (4.41) has the Shockley form, Eq. (4.30). Therefore all the conclusions of Secs. 4.2 and 4.3 apply here, including the criterion (4.19) for existence of the surface states. We find that the surface states have the dispersion $E_0(\mathbf{p})$ and exist for those in-plane momenta \mathbf{p} where the following condition is satisfied

$$|t_1(\mathbf{p})| < |t_2|. \quad (4.54)$$

The boundary of this domain is given by Eq. (4.53). When we change the parameter t_2 while keeping t_1 fixed, the Hamiltonian undergoes a transition between the phases

with odd and even numbers of surface Dirac cones, called the “strong” and “weak” TI phases in Ref. [20]. For small $|t_2| \ll |t_1|$, the contour lines given by Eq. (4.53) wind around the BZ corners K and K' (see Fig. 4.7 for $C = 0.5$), and criterion (4.54) is satisfied in the small area inside. The surface states do not include the Dirac cones of $E_0(\mathbf{p})$, shown in Fig. 4.8, because the TRIM points (red dots) are in the area where Eq. (4.54) is not satisfied. Thus, Hamiltonian (4.41) is in the “weak” TI phase in this case. For $|t_1| = |t_2|$, the contours (4.53) become straight lines passing through the TRIM points M_1, M_2, M_3 , as shown in Fig. 4.7 for $C = 1$. So, both Eqs. (4.51) and (4.53) are satisfied at the TRIM points, and the bulk spectrum, Eq. (4.50), becomes gapless. This marks a transition to the “strong” TI phase. When $|t_1| < |t_2| < 3|t_1|$, the contour forms a circle around the BZ center, see Fig. 4.7 for $C = 2$. Criterion Eq. (4.54) is satisfied in the exterior of the circle, and so the surface states contain the Dirac cones at the TRIM points M_1, M_2 and M_3 . When t_2 reaches the critical value $|t_2| = 3|t_1|$, the contour (4.53) shrinks to the single point Γ . The bulk spectrum becomes gapless, and this marks a transition to the “weak” TI phase again. For $|t_2| > 3|t_1|$, the Shockley criterion is satisfied everywhere in the BZ, so the surface states include the Dirac cones for all TRIM points (4.47).

As discussed above, the Shockley criterion (4.54) is written for the case where the t_2 bond is broken at the surface. If, on the other hand, the crystal termination is such that the t_1 bond is broken at the surface, the existence criterion for the surface

state becomes complementary to the criterion (4.54)

$$|t_1(\mathbf{p})| > |t_2|. \quad (4.55)$$

So, the surface states now exist for those momenta \mathbf{p} where they did not exist in the case of the broken bond t_2 and have the Dirac cones at the complementary TRIM points. This is summarized in Table 4.1, which shows the Dirac cones belonging to the surface states depending on whether t_1 or t_2 is broken at the surface. In the “strong” TI phase, there is an odd number of the Dirac cones in the surface states, so, at least, one surface Dirac cone always exists. In contrast, in the “weak” TI phase, there is an even number of the surface Dirac cones, so the surface states may disappear under certain conditions.

4.4.2 3D vortex lines

In the previous section, we showed that the 2D contour defined by Eq. (4.53) represents the boundary separating the domain in the 2D momentum space where the Shockley criterion is satisfied. On the other hand, the contour (4.53) is just the projection of the 3D vortex line, defined by Eq. (4.52)

$$t(k, \mathbf{p}) = t_1(\mathbf{p}) + t_2 e^{ik} = 0, \quad (4.56)$$

onto the 2D momentum space, as discussed in Sec. 4.3. Let us discuss evolution of these 3D vortex lines with the change of the parameters t_1 and t_2 . In the vicinity

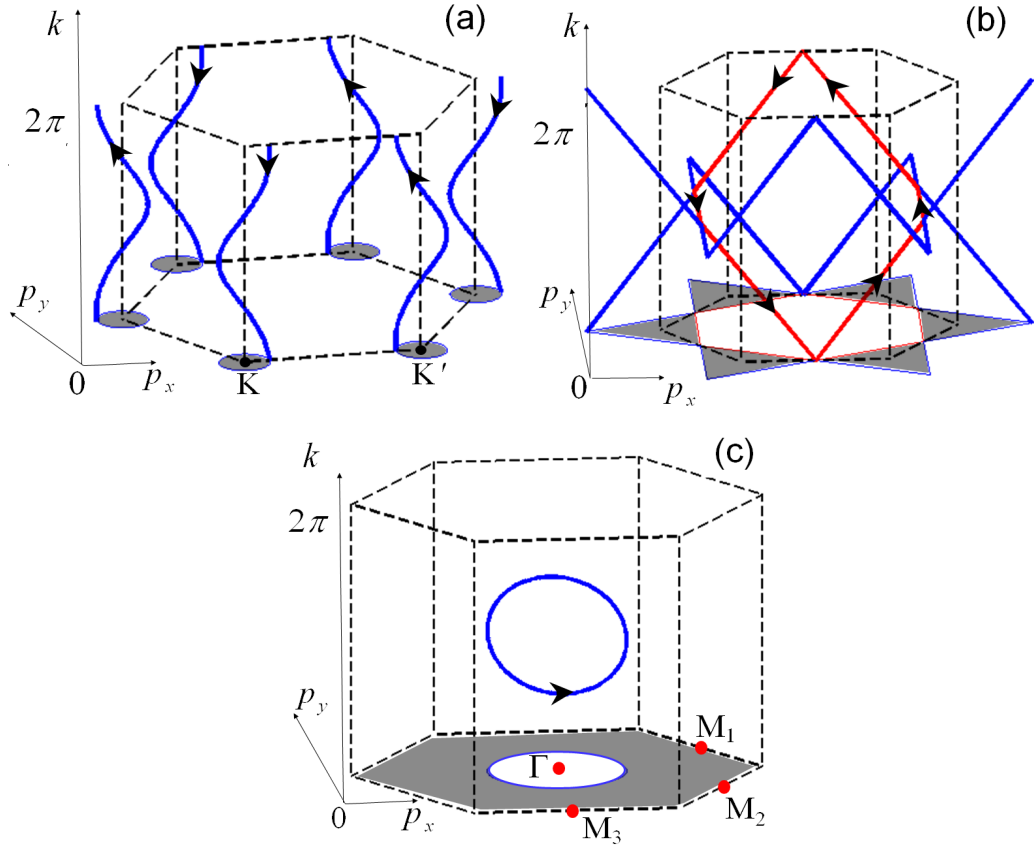


Figure 4.9: Vortex lines in the 3D momentum space defined by Eq. (4.56), and shown for different values of the parameters: (a) $|t_1| > |t_2|$, (b) $|t_1| = |t_2|$, and (c) $|t_1| < |t_2| < 3|t_1|$. The vortex lines are shown by the thick lines with the arrows representing vorticity. The thin lines show projections of the vortex lines, which encircle the shaded area in the 2D momentum space \mathbf{p} , where the Shockley criterion (4.54) is satisfied and the surface states exist. The dashed lines show the boundaries of the BZ. The part of the vortex lines residing in the first BZ is highlighted in red in panel (b). The three panels show the evolution of the vortex lines with the change of the parameters of the Hamiltonian. At $|t_1| = |t_2|$, the vortex lines reconnect at the TRIM points and change their topology from spirals for $|t_1| > |t_2|$ to the loop for $|t_1| < |t_2|$. The change of the vortex lines topology is responsible for a transition from the “weak” to “strong” TI phase in the Hamiltonian (4.41).

of the BZ corners $\mathbf{p}_0 = (\pm 4\pi/3, 0)$, K and K' points in Fig. 4.7, where the function $t_1(\mathbf{p})$ vanishes, Eq. (4.43) can be linearized

$$t_1(\mathbf{p}_0 + \mathbf{p}) \approx -\frac{\sqrt{3}}{2}t_1(\pm p_x + ip_y). \quad (4.57)$$

So, for $|t_2| \ll |t_1|$, Eq. (4.56) with $t_1(\mathbf{p})$ defined in Eq. (4.57) describes spirals in the 3D momentum space (k, \mathbf{p}) [89]

$$\begin{pmatrix} p_x \\ p_y \end{pmatrix} = \frac{2}{\sqrt{3}} \frac{t_2}{t_1} \begin{pmatrix} \pm \cos k \\ \sin k \end{pmatrix}, \quad (4.58)$$

as shown in Fig. 4.9(a). Projections of these spirals onto the 2D momentum space \mathbf{p} encircle the corners K and K' of the 2D BZ. With the increase of t_2 , the spirals grow until t_2 reaches the critical value $|t_2| = |t_1|$. At this point, the vortex lines reconnect as shown in Fig. 4.9(b) and transform into three families of straight lines obtained by intersections of the planes

$$\{\mathbf{p}\delta_1 = \pi + 2\pi n\} \cap \{\mathbf{p}\delta_3 = -k + 2\pi m\}, \quad (4.59)$$

$$\{\mathbf{p}\delta_2 = \pi + 2\pi n\} \cap \{\mathbf{p}\delta_3 = k + 2\pi m\}, \quad (4.60)$$

$$\{\mathbf{p}\delta_3 = \pi + 2\pi n\} \cap \{k = \pi + 2\pi m\}, \quad (4.61)$$

where n and m are independent integers. The part of these lines residing in the first BZ forms a loop highlighted in red for clarity in Fig. 4.9(b). With the further increase of t_2 , the vortex line detaches from the BZ boundary and becomes a closed

loop, as shown in Fig. 4.9(c). In the vicinity of the Γ point, the function $t_1(\mathbf{p})$ given by Eq. (4.43) can be expanded to the second order in \mathbf{p} , so the vortex line defined by Eq. (4.56) is given by the intersection of a cylinder and a plane in the 3D momentum space (k, \mathbf{p})

$$\left\{ p_x^2 + p_y^2 = \frac{2}{3} \left(9 - \frac{t_2^2}{t_1^2} \right) \right\} \cap \left\{ k = \pi + \sqrt{3} \frac{t_1}{t_2} p_y \right\}. \quad (4.62)$$

For the critical value $|t_2| = 3|t_1|$, the vortex line shrinks to the Γ point and then disappears for $|t_2| > 3|t_1|$.

So, we observe that the vortex lines change their topology at the critical values of the model parameters $|t_2| = |t_1|$ and $|t_2| = 3|t_1|$. These are the critical values where the transitions happen between the “weak” and “strong” TI phases. So, the configuration of the vortex lines (4.56) is directly related to the topological phase of the full Hamiltonian H , Eq. (4.41).

Now, let us illustrate that the vortex lines are gauge-dependent, i.e., different choice of phases in the tight-binding model leads to different vortex lines. Let us choose the elementary cell consisting of the A and B atoms connected via the vector \mathbf{a}_2 shown in Fig. (4.6), rather than \mathbf{a}_1 chosen in Eqs. (4.41)-(4.43). Then, Eq. (4.43) becomes $t_1(\mathbf{p}) = t_1 (1 + e^{-i\mathbf{p}\delta_3} + e^{i\mathbf{p}\delta_1})$, which is equivalent to the $2\pi/3$ rotation of $t_1(\mathbf{p})$ in Eq. (4.43) around the k axis. Since $t_1(\mathbf{p})$ defines the vortex lines via Eq. (4.56), the vortex lines are $2\pi/3$ rotated compared to the lines shown in Fig. 4.9. Notice, however, that the area where the surface states exist, shown by the shaded area in Fig. 4.9, is C_3 symmetric and thus remains the same for a different gauge choice.

We also point out that the Shockley Hamiltonian (4.41) and the vortex lines are constructed for a particular crystal termination and cannot be directly used to study surface states for other surfaces. For a different crystal termination, we need to redefine the in-plane \mathbf{p}' and the out-of-plane k' momenta relative to the “new” surface. Since the “new” momenta (k', p'_x, p'_y) are related to the “old” momenta (k, p_x, p_y) through some orthogonal transformation O : $(p_x, p_y, k)^T = O(p'_x, p'_y, k')^T$, the diagonal element of Hamiltonian (4.41) is generally a function of both k' and \mathbf{p}' : $h(\mathbf{p}) = h(k', \mathbf{p}')$. So, the Hamiltonian of the “new” surface does not have the Shockley form (4.41), which requires that $h(\mathbf{p}')$ is independent of k' , and the Shockley criterion is not directly applicable (see a discussion in the end of Sec. 4.3.1).

4.5 Shockley model description of Bi_2Se_3

4.5.1 General analysis

Despite its simplicity, the Shockley model may be directly relevant to the description of real materials, such as Bi_2Se_3 . The crystal of Bi_2Se_3 is formed by a sequence of quintuple layers [73, 74, 84, 86, 87]. Each quintuplet consists of five alternating layers of Bi and Se, as sketched in Fig. 4.10(a). Chemical bonding within the quintuplets is relatively strong, whereas the inter-quintuplet Van der Waals attraction is relatively weak. So, the natural cleavage plane lies between the quintuplets, as shown in Fig. 4.10(a).

For the relevant energy interval near the Fermi level, the electronic structure can be captured by considering the electronic orbitals localized near the outermost

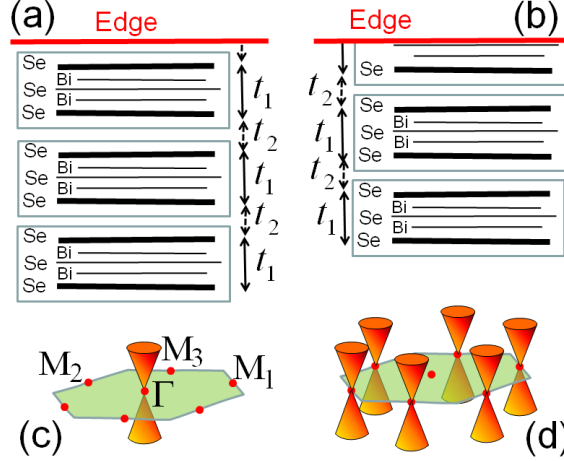


Figure 4.10: The crystal of Bi_2Se_3 is formed by quintuple layers, schematically shown by the blue boxes. Each quintuplet consists of the alternating layers Se-Bi-Se-Bi-Se. The tight-binding tunneling amplitudes t_1 and t_2 connect the orbitals of the outermost edges of the quintuplets. Then, depending on whether t_2 or t_1 is broken at the surface, as shown by the red line in panels (a) and (b), surface states occur in different regions of the 2D momentum space, as shown in Panels (c) and (d).

layers of Se within the quintuplets [84], as shown by the thick lines in Fig. 4.10(a). Then, the Shockley amplitudes t_1 and t_2 describe the intra- and inter-quintuplet tunneling between these orbitals, as shown in Fig. 4.10(a). The tunneling amplitudes t_1 and t_2 may depend on the in-plane momentum \mathbf{p} .

As shown in the previous section, the Shockley surface states strongly depend on how the crystal is terminated. When the crystal is cut between the quintuplets, and t_2 is broken on the surface as shown Fig. 4.10(a) and realized experimentally, a single Dirac cone is observed at the BZ center [85], as shown in Fig. 4.10(c). So, in terms of the Shockley model, the surface state existence criterion $|t_1(\mathbf{p})| < |t_2(\mathbf{p})|$ is satisfied at the BZ center and not satisfied at the BZ boundary.

In principle, the surface can also be introduced by cutting the quintuplet layer

and breaking the bond t_1 , as shown in Fig. 4.10(b). To the best of our knowledge, this type of surface has not been observed in Bi_2Se_3 . In the previous section, we found that, for alternative crystal terminations, the surface states have the Dirac cones at the complementary TRIM points of the 2D BZ. Thus, we conclude that, when the quintuplet is broken at the surface as in Fig. 4.10(b), the surface states should have Dirac cones at the boundary of the 2D BZ as shown in Fig. 4.10(d). A similar prediction was made for the $\text{Bi}_x\text{Sb}_{1-x}$ alloy in Ref. [88].

We can estimate the Shockley tunneling amplitudes $t_1(\mathbf{p})$ and $t_2(\mathbf{p})$ for \mathbf{p} close to the Γ point based on the band-structure calculations of Ref. [73]. As discussed in Sec. 4.2.1, the extreme values of the energy gap can be obtained from the off-diagonal matrix element $t(k) = t_1 + t_2 e^{ik} \Big|_{k=0,\pi} = t_1 \pm t_2$. We compare these values with the band structure along the direction $k \in (0, \pi)$ for the fixed in-plane momentum $\mathbf{p} = 0$, which is shown in Fig. 2(b) of Ref. [73]. From the set of equations $t_1 + t_2 = 0.28$ eV and $t_1 - t_2 = -0.6$ eV, we obtain the following estimate

$$t_1 = -0.16 \text{ eV}, \quad t_2 = 0.44 \text{ eV}. \quad (4.63)$$

Note that the geometric distance between the orbitals on the adjacent quintuplets is shorter than the distance between the orbitals within the quintuplet. Therefore, in the vicinity of the Γ point, the inter-quintuplet tunneling $|t_2|$ should be greater than the intra-quintuplet tunneling $|t_1|$, which is consistent with Eq. (4.63).

4.5.2 Continuous approximation

In previous sections, we have shown that, in the Shockley model, existence of the surface states relies explicitly on the tight-binding nature of the model. However, continuous models [73–77] are also widely used to describe the surface states in the TI models and in real materials, such as Bi_2Se_3 . A continuous approximation is obtained by expanding the Hamiltonian in the powers of the momentum k in the z direction. This is equivalent to disregarding the BZ periodicity for the momentum k and taking the limit where the size of the elementary cell in the z direction goes to zero. In this subsection, we examine the applicability of the continuous-limit approximation.

4.5.2.1 First-order expansion

Let us consider the Shockley Hamiltonian (4.30) for the fixed value of the in-plane momentum $\mathbf{p} = \mathbf{p}_*$, where the diagonal elements vanish

$$H(k) = \begin{pmatrix} 0 & t^*(k) \\ t(k) & 0 \end{pmatrix}, \quad (4.64)$$

$$t(k) = t_1 + t_2 e^{ik}. \quad (4.65)$$

Without loss of generality, let us make an assumption that $t_2 > 0$. If the energy gap $|t(k)|$ reaches minimum at $k = 0$, then $t_1 < 0$ as in Eq. (4.63). Then, we expand

$t(k)$ to the first order in k around $k = 0$

$$t(k) = t_1 + t_2 + it_2k. \quad (4.66)$$

The tight-binding boundary conditions (4.10) and (4.11) correspond the following boundary conditions [84] for the continuous approximation

$$\psi_a(z \rightarrow 0) \neq 0, \quad \psi_b(z \rightarrow 0) = 0, \quad (4.67)$$

$$\psi_{a,b}(z \rightarrow \infty) = 0. \quad (4.68)$$

Using these boundary conditions, we solve the Schrödinger equation $H\Psi = 0$ for Hamiltonian (4.64) with the continuous $t(k)$, Eq. (4.66), and obtain the surface state

$$\Psi_0(z) = \begin{pmatrix} 1 \\ 0 \end{pmatrix} e^{ik_0z}. \quad (4.69)$$

The exponential decay length in Eq. (4.69) is given by the parameter

$$k_0 = i \left(1 + \frac{t_1}{t_2} \right), \quad (4.70)$$

which is the root of the equation $t(k_0) = t_1 + t_2 + it_2k_0 = 0$. Boundary conditions (4.68) are satisfied if $\text{Im } k_0 > 0$ or equivalently $t_1 > -t_2$; otherwise, the surface state does not exist if $t_1 < -t_2$. So, the continuous model (4.66) with the appropriate boundary conditions (4.67) and (4.68) gives the surface state existence

criterion

$$|t_1| < |t_2|, \quad (4.71)$$

which coincides with the Shockley criterion (4.19). The continuous wave function (4.69) correctly approximates the discrete wave function (4.18) if the decay length is very long or equivalently $||t_1| - |t_2|| \ll |t_2|$. However, the estimated tunneling amplitudes t_1 and t_2 in Eq. (4.63) do not satisfy the latter condition for Bi_2Se_3 . Therefore, we conclude that the discrete Shockley model gives a more appropriate description of the surface states in Bi_2Se_3 , than a continuous approximation, because the difference between $|t_1|$ and $|t_2|$ is rather large.

4.5.2.2 Higher-order expansion

One may truncate the series for e^{ik} in Eq. (4.66) at a higher order in k

$$t(k) = t_1 + t_2 + t_2 \sum_{n=1}^N \frac{(ik)^n}{n!}. \quad (4.72)$$

However, such a truncation gives worse continuous description of the Shockley surface state. The equation $t(k) = 0$ now has N roots k_1, \dots, k_N . So, there are N independent coefficients c_n in a general solution $\Psi(z) = c_1 e^{ik_1 z} + \dots + c_N e^{ik_N z}$ to satisfy the boundary conditions (4.67) and (4.68). This gives rise to a large number of the unphysical surface state solutions, while the Shockley model predicts only one surface state. Most of the roots k_j have large imaginary parts $\text{Im } k_j \sim 1$. These solutions are spurious, because they correspond to the wave functions decaying over

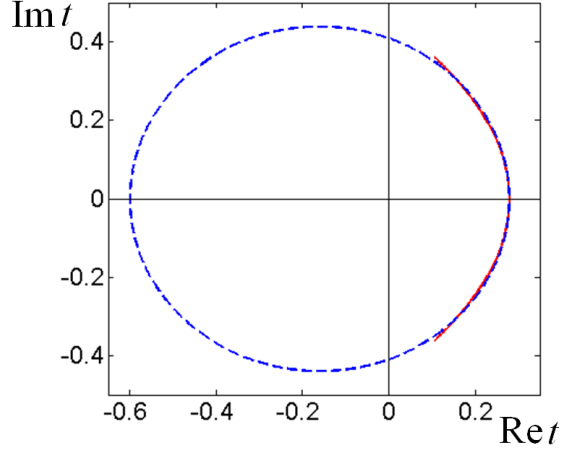


Figure 4.11: Plot of the function $t(k)$ in the complex plane of $(\text{Re } t, \text{Im } t)$. The second-order expansion for $t(k)$, given by Eq. (4.79) is plotted by the solid line for $-\pi/2 < k < \pi/2$. The function $t(k)$ in the Shockley model, given by Eq. (4.65) with the parameters t_1 and t_2 from Eq. (4.63), is plotted by the dashed line. The Shockley contour winds around the origin, which guarantees existence of the surface state.

a length shorter than the unit cell of the crystal. For example, for $N = 2$, Eq. (4.72)

is

$$t(k) = t_1 + t_2 + it_2k - t_2^2k^2/2. \quad (4.73)$$

Then, the equation $t(k) = 0$ has two roots

$$k_{1,2} = i \pm \sqrt{-1 + 2(1 + t_1/t_2)}. \quad (4.74)$$

In the limit $|1 + t_1/t_2| \ll 1$, the roots become $k_1 = i(1 + t_1/t_2)$ and $k_2 = 2i$. We observe that, while the first root k_1 reproduces the correct approximation Eq. (4.70), the second root k_2 has a large imaginary part and must be discarded. In another regime, when the expression under the square root in Eq. (4.74) is positive, both

roots have large imaginary parts $\text{Im } k_{1,2} = 1$, so the continuous approximation is not applicable. Moreover, as pointed out in Ref. [84], the continuous description does not distinguish between two possible ways of terminating the crystal shown in Fig. 4.10(a) and (b). A correct boundary condition should be chosen to distinguish between different possible surface terminations.

Despite these problems, the k^2 terms were kept in the effective description of Bi_2Se_3 in Ref. [74]

$$H = H_0 + H_1, \quad (4.75)$$

$$H_0 = \epsilon(k) + (M_0 + M_1 k^2) \tau_z + B_0 k \tau_y, \quad (4.76)$$

$$H_1 = A_0 \tau_x (\boldsymbol{\sigma} \times \mathbf{p}), \quad (4.77)$$

where $M_0 = -0.28 \text{ eV}$, $M_1 = 6.86 \text{ eV}\text{\AA}^2$, $B_0 = 2.26 \text{ eV}\text{\AA}$, $A_0 = 3.33 \text{ eV}\text{\AA}$; τ_y and τ_x are the Pauli matrices. In Eq. (4.77), H_1 represents spin-orbit interaction and explicitly depends on the spin operators $\boldsymbol{\sigma}$ and the in-plane momentum \mathbf{p} . H_0 depends on the out-of-plane momentum k and is responsible for the existence of the surface states. Following Ref. [74], we drop the term $\epsilon(k)$ in Eq. (4.76), because it is proportional to the unit matrix. Then we apply the unitary transformation $e^{-i\tau_y\pi/4}$,

which changes $\tau_z \rightarrow -\tau_x$ and $\tau_x \rightarrow \tau_z$. So, the Hamiltonian becomes $U^\dagger H_0 U \rightarrow H_0$

$$H_0 = \begin{pmatrix} h(\mathbf{p}) & t^*(k) \\ t(k) & -h(\mathbf{p}) \end{pmatrix}, \quad (4.78)$$

$$t(k) = -M_0 - M_1 k^2 + iB_0 k, \quad (4.79)$$

$$h(\mathbf{p}) = A_0(\boldsymbol{\sigma} \times \mathbf{p}). \quad (4.80)$$

Now, the Hamiltonian H_0 has the same form as in Eq. (4.30). Following Ref. [84], we infer that the basis for the Hamiltonian (4.78) corresponds to the basis of electron orbitals located at the outermost layers of the quintuplet. Then, the off-diagonal matrix element $t(k)$ in Eq. (4.79) corresponds to the second-order expansion of the off-diagonal element of the Shockley model (4.73), while $h(\mathbf{p})$ defines the in-plane dispersion.

To make explicit correspondence with the previous section, we change units for k : $ka \rightarrow k$, where $a = 1$ nm is the size of the elementary cell of Bi_2Se_3 in the z direction. So, we rewrite the parameters $M_1/a^2 \rightarrow M_1$, $B_0/a \rightarrow B_0$ in the energy units of eV

$$M_0 = -0.28 \text{ eV}, \quad M_1 = 0.07 \text{ eV}, \quad B_0 = 0.23 \text{ eV}.$$

Notice that $t(k)$, Eq. (4.79), parametrizes a parabola in the complex space ($\text{Re } t, \text{Im } t$) when k is changed. So we plot $t(k)$ defined by Eq. (4.79) for $-\pi/2 < k < \pi/2$ by the solid line in Fig. 4.11. Figure 4.11 also shows the plot $t(k)$ for the

discrete Shockley model (4.64) with the parameters (4.63) by the dashed line. We see that the continuous approximation to the Hamiltonian agrees with the Shockley model within a limited range of k with the continuous approximation. Nevertheless, the continuous approximation has serious deficiencies for construction of the wave functions, as described above, whereas the Shockley model provides a good overall description for the surface states in Bi_2Se_3 .

4.6 Generalized Shockley model

In this section, we generalize the Shockley model to include additional inter-cell tunneling amplitudes. To simplify notations, we present results for the 1D case. However, the results can be straightforwardly generalized to the 3D case by assigning dependence on $\mathbf{p} = (p_x, p_y)$ to the tunneling amplitudes, as discussed in Sec. 4.2.

4.6.1 Additional tight binding amplitude t_3

Let us consider a 1D Hamiltonian of the form given by Eq. (4.1) with

$$U = \begin{pmatrix} 0 & t_1^* \\ t_1 & 0 \end{pmatrix}, \quad V = \begin{pmatrix} 0 & t_2^* \\ t_3 & 0 \end{pmatrix}, \quad (4.81)$$

where the matrix V now contains an additional tight-binding amplitude t_3 . The 1D chain model corresponding to Eq. (4.81) is illustrated in Fig. 4.12. The amplitude t_1 describes tunneling between the A and B sublattices inside the unit cell, and the amplitudes t_2 and t_3 between the unit cells. The introduction of this tight-binding

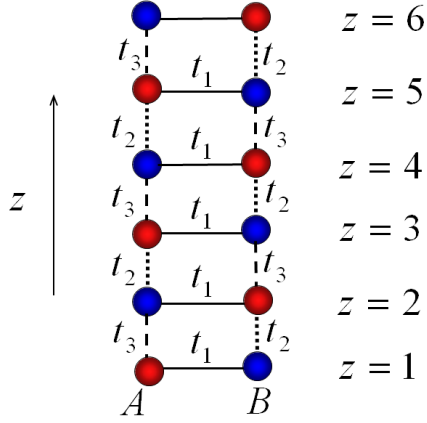


Figure 4.12: An illustration of the generalized Hamiltonian (4.82). The Hamiltonian describes a tight-binding model with the elementary cell comprised of the A and B sites, which are connected via the complex tight-binding amplitudes t_1 , t_2 and t_3 .

amplitude is motivated by the TI literature [9, 72] as well by the novel 1D models such as the superconducting Majorana chain [10, 90] and the Creutz ladder [91, 92]. This model is a natural mathematical generalization of the models considered in the previous sections. The Hamiltonian of the general model has the same form as in Eq. (4.5),

$$H(k) = \begin{pmatrix} 0 & t^*(k) \\ t(k) & 0 \end{pmatrix}, \quad (4.82)$$

with

$$t(k) = t_1 + t_2 e^{ik} + t_3 e^{-ik}. \quad (4.83)$$

As in Eqs. (4.12) and (4.13), the eigenstate equations for the wave functions on the A and B sublattices decouple at $E = 0$. (Appendix A.2 proves that the edge state can exist only for $E = 0$.) The zero-energy state on the A sublattice has the

complex momentum k obtained from the equation

$$t(k) = t_1 + t_2 e^{ik} + t_3 e^{-ik} = 0. \quad (4.84)$$

We substitute $q = e^{ik}$ and obtain an equation for the rational function $t(q)$

$$t(q) = t_1 + t_2 q + t_3 q^{-1} = 0, \quad (4.85)$$

which has two solutions

$$q_{1,2} = e^{ik_{1,2}} = \frac{1}{2t_2} \left(-t_1 \pm \sqrt{t_1^2 - 4t_2 t_3} \right), \quad (4.86)$$

with the complex momenta $k_{1,2}$. Using these momenta, we construct an edge state that satisfies the boundary conditions given by Eqs. (4.10) and (4.11). The edge state has the energy $E_0 = 0$ and is localized on the A sublattice

$$\Psi_0(z) = \begin{pmatrix} \psi_a^{(0)}(z) \\ 0 \end{pmatrix}, \quad E_0 = 0, \quad (4.87)$$

$$\psi_a^{(0)}(z) = q_1^z - q_2^z = e^{ik_1 z} - e^{ik_2 z}. \quad (4.88)$$

The wave function (4.88) satisfies the boundary condition (4.11) if $\text{Im } k_1 > 0$ and $\text{Im } k_2 > 0$ or, equivalently,

$$|q_1| < 1 \text{ and } |q_2| < 1. \quad (4.89)$$

Likewise, a zero-energy state on the B sublattice has the complex momenta k obtained from the equation

$$t^*(k) = t_1^* + t_2^* e^{-ik} + t_3^* e^{ik} = 0. \quad (4.90)$$

Notice that the symbol of complex conjugation $*$ applies only to the tunneling amplitudes in Eq. (4.90), so $t^*(k) \neq [t(k)]^*$ if $\text{Im } k \neq 0$. Equation (4.90) can be obtained by replacing $k \rightarrow k^*$ in Eq. (4.84). So, the two solutions $k'_{1,2}$ of Eq. (4.90) and the corresponding $q'_{1,2}$ can be obtained from Eq. (4.86)

$$k'_{1,2} = k_{1,2}^*, \quad q'_{1,2} = 1/q_{1,2}^*. \quad (4.91)$$

The edge state exists on the B sublattice

$$\Psi_0(z) = \begin{pmatrix} 0 \\ \psi_b^{(0)}(z) \end{pmatrix}, \quad E_0 = 0, \quad (4.92)$$

$$\psi_b^{(0)}(z) = (q'_1)^z - (q'_2)^z = e^{ik'_1 z} - e^{ik'_2 z} \quad (4.93)$$

if $\text{Im } k'_1 > 0$ and $\text{Im } k'_2 > 0$ or, equivalently,

$$|q_1| > 1 \text{ and } |q_2| > 1. \quad (4.94)$$

To summarize, the edge state (4.88) exists on the A sublattice if both roots of Eq. (4.85) are inside the unit circle, as in Eq. (4.89) and in Fig. 4.13(a). The edge

state (4.93) exists on the B sublattice if both roots of Eq. (4.85) are outside the unit circle, as in Eq. (4.94). The edge state does not exist if one of the roots is inside and another root is outside the unit circle

$$|q_1| > 1 \text{ and } |q_2| < 1, \quad (4.95)$$

as shown in Fig. 4.13(b). Obviously, the conditions (4.89) and (4.94) cannot be met simultaneously, so edge state cannot exist on both sublattices simultaneously.

Like in Sec. 4.2.1, the criterion for the edge states existence can be formulated in terms of the winding number of the complex function $t(q)$ along the unit circle $C = \{|q| = 1\}$

$$W = \frac{1}{2\pi i} \oint_{|q|=1} dq \frac{d}{dq} \ln [t(q)]. \quad (4.96)$$

The criteria given by Eqs. (4.89), (4.94), and (4.95) are summarized in the following

$$W = \begin{cases} 1, & \text{edge state } \psi_a^{(0)}(z) \text{ exists,} \\ 0, & \text{edge state does not exist,} \\ -1, & \text{edge state } \psi_b^{(0)}(z) \text{ exists.} \end{cases} \quad (4.97)$$

To prove it, we use Cauchy's argument principle

$$W = Z - P, \quad (4.98)$$

which relates the winding number W of a complex function $t(q)$ on a contour C with the number of zeros Z and the number of poles P inside the contour C . Since

$t(q)$ given by Eq. (4.85) has a pole at $q = 0$, as shown by the thick black dot in Fig. 4.13(a) and (b), the number of poles is $P = 1$. The edge state exists on the A sublattice if $|q_{1,2}| < 1$, in which case $W = Z - P = 2 - 1 = 1$. The edge state exists on the B sublattice if $|q_{1,2}| > 1$, in which case $W = Z - P = 0 - 1 = -1$. The edge state does not exist for $|q_1| > 1$ and $|q_2| < 1$, in which case $W = Z - P = 1 - 1 = 0$.

In other words, according to Eq. (4.97), the edge state exists if the closed contour

$$C' = \{t(k), k \in (0, 2\pi)\} \quad (4.99)$$

winds around the origin, as shown in Fig. 4.13(c). The direction of winding of $t(k)$ defines the sublattice on which the edge state is localized. An analogous criterion was proposed in Ref. [9].

For the tunneling amplitudes t_1 , t_2 , and t_3 connecting the nearest unit cells, Eq. (4.99) defines an ellipse

$$t(k) = t_1 + (t_2 + t_3) \cos k + i(t_2 - t_3) \sin k, \quad (4.100)$$

which is shifted by t_1 from the origin. In case where the tunneling amplitudes are real, the ellipse in Eq. (4.100) encloses the origin if

$$|t_1| < |t_2 + t_3|. \quad (4.101)$$

Eq. (4.101) represents the generalized Shockley rule of a stronger bond: The edge state exists if the broken inter-cell bond $t_2 + t_3$ is stronger than the intra-cell bond

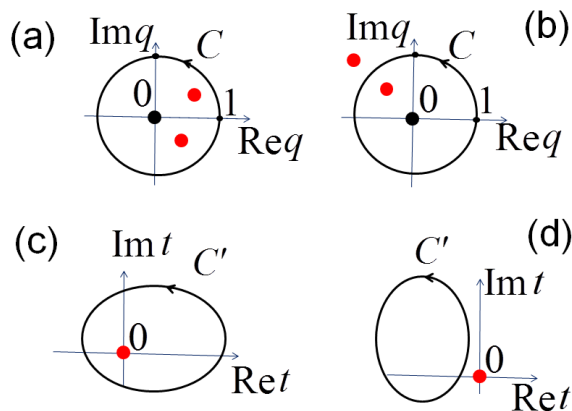


Figure 4.13: Topological formulation of the Shockley criterion. The roots $q_{1,2}$ of Eq. (4.85) are shown in panels (a) and (b) by red dots. An edge state exists if the roots are on the same side of the unit circle $C = \{q = e^{ik}, k \in (0, 2\pi)\}$, as shown in panel (a). No edge state exists if the roots are on the opposite sides of the unit circle, as shown in panel (b). The thick black dot at the origin is the pole of Eq. (4.85). An alternative formulation in terms of the winding number (4.97) is shown in panels (c) and (d). An edge state exists if the contour $C' = \{t(k), k \in (0, 2\pi)\}$ winds around the origin, as shown in panel (c). No edge state exists if the contour C' does not wind around the origin, as shown in panel (d).

t_1 .

Our consideration does not include tunneling amplitudes connecting sites on the same sublattices in different unit cells. Including such terms would make h in Eq. (4.30) depend on k . When these tunneling amplitudes connect only the nearest neighboring unit cells, the problem can still be solved as shown in Ref. [9].

4.6.2 Arbitrary periodic function $t(k)$

In the most general form, Hamiltonian (4.82) can be written as

$$H(k) = \begin{pmatrix} 0 & t^*(k) \\ t(k) & 0 \end{pmatrix}, \quad (4.102)$$

where

$$t(k) = \sum_{n=-N}^N t_n e^{ikn}. \quad (4.103)$$

This model describes a 1D tight-binding chain, where each unit cell is coupled to N preceding and N successive unit cells. Therefore, for a half-infinite system at $z \geq 1$, the boundary conditions require that the wave function vanishes at the fictitious N sites adjacent to the boundary

$$\Psi(-N+1) = 0, \quad \dots, \quad \Psi(-1) = 0, \quad \Psi(0) = 0, \quad (4.104)$$

similarly to Eq. (4.10). As in the previous section, let us substitute $q = e^{ik}$ and rewrite Eq. (4.103) in the polynomial form

$$t(q) = \sum_{n=-N}^N t_n q^n. \quad (4.105)$$

This polynomial has $2N$ roots. Suppose, the number of roots N_1 with $|q_j| < 1$, $j = 1, \dots, N_1$, is greater than N : $N_1 > N$. In this case, we can construct a trial

wave function

$$\Psi(z) = \sum_{j=1}^{N_1} \alpha_j q_j^z, \quad (4.106)$$

which vanishes at $z \rightarrow \infty$. The coefficients α_j in Eq. (4.104) are obtained by solving a set of N boundary condition equations (4.104). Therefore, in general, there are $N_1 - N$ linearly independent solutions for the edge states localized on the sublattice A. The same result can be formulated using the winding number in Eq. (4.96). Indeed, the function (4.105) has a pole of the N -th order at $q = 0$ and N_1 zeros at $|q_j| < 1, j = 1, \dots, N_1$. Therefore, using Cauchy's argument principle (4.98), we obtain

$$W = Z - P = N_1 - N. \quad (4.107)$$

Thus, the winding number W of the function $t(k)$ gives the number of the edge states. On the other hand, if $W < 0$, then there are $|W|$ degenerate edge states localized on the sublattice B. The edge states cannot exist simultaneously on both sublattices A and B. There are no edge states for $W = 0$. Finally, in the limit $N \rightarrow \infty$, the winding criterion applies to an arbitrary complex function $t(k)$ periodic in k .

4.7 Symmetries

In this section, we discuss the symmetries of the Shockley model. Let us first consider the case $h(\mathbf{p}) = 0$ in the generalized Shockley Hamiltonian (4.30)

$$H(k, \mathbf{p}) = \begin{pmatrix} 0 & t^*(k, \mathbf{p}) \\ t(k, \mathbf{p}) & 0 \end{pmatrix}. \quad (4.108)$$

In this case, the A and B sublattices have equal on-site energies, which is reflected by a chiral symmetry of the Hamiltonian: $\tau_z H(k, \mathbf{p}) \tau_z = -H(k, \mathbf{p})$, where $\boldsymbol{\tau} = (\tau_x, \tau_y, \tau_z)$ are the Pauli matrices acting in the AB sublattice space. Therefore, Hamiltonian (4.108) belongs to the class AIII of chiral Hamiltonians [28]. As a consequence of chiral symmetry, the energy spectrum is symmetric: if Ψ is an eigenstate $H\Psi = E\Psi$, then $\tau_z\Psi$ is also an eigenstate corresponding to the opposite energy $H\tau_z\Psi = -E\tau_z\Psi$. Therefore, if a non-degenerate eigenstate with $E = 0$ exists, it should be an eigenstate of $\tau_z\Psi = \lambda\Psi$, $\lambda = \pm 1$. So, the $E = 0$ state must be localized on one of the sublattices, consistently with Eq. (4.18). The winding number $W \in Z$ of the vector $\mathbf{d}(k, \mathbf{p})$, defined in Eq. (4.29), gives the number of surface states for a fixed \mathbf{p} .

In Sec. 4.2.2, we generalized the Shockley model by including the diagonal element $h(\mathbf{p})$

$$H(k, \mathbf{p}) = \begin{pmatrix} h(\mathbf{p}) & t^*(k, \mathbf{p}) \\ t(k, \mathbf{p}) & -h(\mathbf{p}) \end{pmatrix}. \quad (4.109)$$

The Hamiltonian (4.109) does not have a chiral symmetry, but it has another sublattice symmetry $(i\tau_y K) H (i\tau_y K) = H$, where K is the operator of complex conjugation. This symmetry exchanges the sublattices, $i\tau_y K (\psi_A, \psi_B)^T = (\psi_B^*, -\psi_A^*)^T$, and makes the bulk spectrum symmetric (there is an opposite energy counterpart $i\tau_y K \Psi$ for every eigenstate Ψ). However, this symmetry is broken at the boundary of the crystal, where one of the sublattices is exposed at the surface, as shown in Fig. 4.3. As a result, the surface state gains the dispersion $E_0(\mathbf{p}) = h(\mathbf{p})$, whereas the opposite-energy counterpart of the surface state is localized at the opposite sur-

face. The number of the surface states is still given by the winding number $W \in \mathbb{Z}$ of the vector $\mathbf{d}(k, \mathbf{p})$ as a function k for a fixed \mathbf{p} .

In this work, we discussed Hamiltonians with the time-reversal symmetry in the presence of spin-orbit coupling, which belong to the class AII of topological insulators classification [28]. The spin-orbit coupling and the time-reversal symmetry require the term $h(\mathbf{p})$ to have the 2D Dirac-type form, as discussed in Sec. 4.3.2. However, the Shockley Hamiltonian (4.109) is applicable in a more general case, where the term $h(\mathbf{p})$ is an arbitrary Hermitian matrix not necessarily respecting the time-reversal symmetry. So, the Shockley Hamiltonian (4.109) can describe the quantum Hall states, which belong to the class A of topological insulators classification [28]. In addition, the Shockley model can describe superconducting systems, in which case Eq. (4.109) should be understood as a Bogolyubov-de Gennes Hamiltonian [11, 82, 83, 93], and $i\tau_y K$ represents the particle-hole symmetry.

4.8 Conclusions

We explore a tight-binding theory of the surface states in topological insulators. We show that the surface states can be understood using the simple and well-known Shockley model [1, 3], a 1D model with the A and B atoms per unit cell, connected via alternating tunneling amplitudes. We generalize the 1D Shockley model to the 3D case described by the 2×2 Hamiltonian (4.30) with the diagonal element $h(\mathbf{p})$ and the off-diagonal element $t(k, \mathbf{p})$. The diagonal element $h(\mathbf{p})$ defines the energy dispersion of the surface states, while the complex-valued off-diagonal element $t(k, \mathbf{p})$

defines the domain of existence of the surface states. The surface states exist for those in-plane momenta \mathbf{p} where the phase winding of $t(k, \mathbf{p})$ along $k \in (0, 2\pi)$ is non-zero. The sign of the winding number gives the sublattice A or B, on which the surface states are localized. Equation $t(k, \mathbf{p}) = 0$ defines a vortex line in the 3D momentum space [78, 82, 83], and projection of the vortex line onto the 2D space of \mathbf{p} is the boundary of the domain where the surface states exist. We apply this approach to the TI model on the diamond lattice [20]. We show how the evolution of the vortex lines is responsible for transitions between the “weak” and “strong” TI phases. We discuss why the discrete Shockley model is better than continuous models for the description of the edge states in real materials, such as Bi_2Se_3 . The tight-binding model demonstrates that different types of surface states are formed depending on how crystal is terminated [84]. The surface states have the Dirac cone at the center of the Brillouin zone when the crystal is cut between the quintuple layers of Bi_2Se_3 , but, when the crystal is terminated inside the quintuple layer, the surface states have three Dirac cones on the boundary of the Brillouin zone. We also generalize the Shockley model to an arbitrary complex function $t(k)$ periodic in k , which includes the long-range inter-cell tunneling amplitudes. We prove the validity of the winding number criterion in this general case as well.

Chapter 5: Thin film of a topological insulator in a parallel magnetic field

5.1 Introduction.

As discussed in previous Chapter, the three-dimensional (3D) topological insulators have the helically-spin-polarized surface states with the two-dimensional (2D) Dirac dispersion, which are observed experimentally [85, 94–96]. Experiments show that the Fermi level is often lifted to the conduction band, thus making the topological surface states less relevant for the properties of real materials [97]. In part, this motivated the study of the thin films of TIs, where the Fermi level, bulk gap and the hybridization between the opposite surface states can be tuned [98–100]. A number of intriguing effects for the TI films were predicted in the case where the top and bottom surfaces interact [101]. In the ultra-thin limit, a gap opens in the surface states electronic spectrum due to hybridization between the opposite surfaces [75, 99, 102, 103].

While most papers study the in-plane transport properties of the surface states, here we study the tunneling conductance G per unit area across the ultra-thin TI film in the presence of a parallel magnetic field B_y (see Fig. 5.1). The in-plane

magnetic field results in a relative shift of the Dirac cones of the surface states in momentum space, as discussed in related works on graphene bilayer [104]. However, unlike the spectrum of graphene, the spectrum of the TI thin film remains gapped until a critical value of the magnetic field is achieved [105]. Motivated by the original measurements of G vs B_y for a GaAs bilayer by Eisenstein et al. [106], here we calculate the tunneling conductance for a TI film as a function of the parallel magnetic field. In contrast to other systems, the spin structure of the electronic spectrum for the surface states of TI results in unusual dependence of the tunneling conductance on B_y . In a recent experiment [107], the authors observed a strong B_y dependence of the out-of-plane current in a film of Bi_2Te_3 . The predicted theoretical dependence G vs B_y is in qualitative agreement with the experimental curve. In addition, we predict that the spin polarization of the tunneling current is proportional to the magnetic field. The 100% spin polarization can be achieved for an experimentally accessible strength of the magnetic field.

5.2 Model.

Let us consider a film of TI, which has two states ψ_1 and ψ_2 localized at the opposite surfaces of the film, as shown in red and blue in Fig. 5.1. While the wave functions are localized in the z direction, electrons are free to move parallel to the surface, so the in-plane momentum $\mathbf{p} = (p_x, p_y)$ is a good quantum number. For clarity of consideration, we model the surface states by the simple Rashba

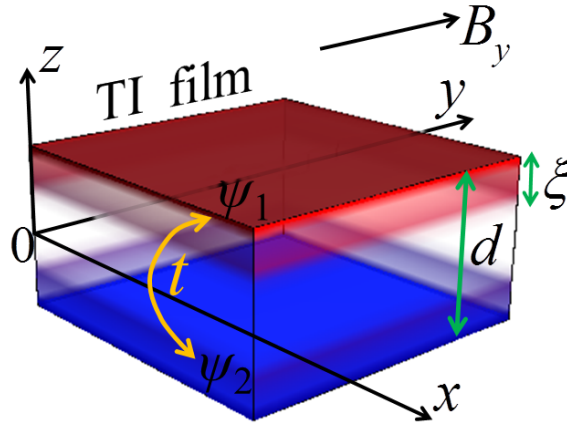


Figure 5.1: Thin film of a topological insulator of thickness d in a parallel magnetic field B_y . The surface states ψ_1 and ψ_2 shown in red and blue overlap and couple when the thickness d is comparable with the decay length ξ of the surface state.

Hamiltonians

$$h_{\psi_1, \psi_2} = \pm h(\mathbf{p}), \quad (5.1)$$

$$h(\mathbf{p}) = v \hat{\mathbf{z}}(\hat{\boldsymbol{\sigma}} \times \mathbf{p}) = v(\hat{\sigma}_x p_y - \hat{\sigma}_y p_x). \quad (5.2)$$

Different signs \pm correspond to the surface states ψ_1 and ψ_2 and describe the unit Rashba vectors $\pm \hat{\mathbf{z}}$ (see Fig. 5.1 of Chapter 4), which are collinear with the normals to the corresponding surfaces. The variable v has dimensions of velocity, and $\hat{\sigma}_\alpha = (\hat{1}, \hat{\boldsymbol{\sigma}})$ denotes a full set of the operators acting in the spin space, where $\hat{1}$ is a 2×2 unit matrix and $\hat{\boldsymbol{\sigma}} = (\hat{\sigma}_x, \hat{\sigma}_y, \hat{\sigma}_z)$ are the Pauli matrices. Hamiltonian (5.2) has the

following eigenstates and eigenenergies

$$|\mathbf{p}, \pm\rangle = \frac{1}{\sqrt{2}} \begin{pmatrix} 1 \\ \pm e^{-i \arctan(p_x/p_y)} \end{pmatrix}, \quad E_0(\mathbf{p}) = \pm v|\mathbf{p}|, \quad (5.3)$$

where the spectrum has a well-known form of the 2D Dirac cone. The spinors in Eq. (5.3) describe the helical spin-momentum locking with the spin polarization perpendicular to the momentum

$$\mathbf{S}(\mathbf{p}) = \langle \mathbf{p}, \pm | \hat{\boldsymbol{\sigma}} | \mathbf{p}, \pm \rangle = \pm \frac{(\mathbf{p} \times \hat{\mathbf{z}})}{|\mathbf{p}|}, \quad (5.4)$$

so the helicity (5.4) is opposite for the $|\mathbf{p}, +\rangle$ and $|\mathbf{p}, -\rangle$ bands. Because of the minus sign for h_{ψ_2} in Eq. (5.1), the bands $|\mathbf{p}, \pm\rangle$ are energetically-inverted, and, so, the helicities for the opposite surface states ψ_1 and ψ_2 are opposite for a fixed energy. The wave functions of the surface states ψ_1 and ψ_2 decay into the bulk and have a finite decay length ξ , as illustrated in Fig. 5.1. So, when the thickness of the film d becomes comparable with the decay length $d \sim \xi$, there is a finite coupling between the surface states t , which we assume to be proportional to the unit matrix in the spin space. So, the TI film can be modeled by a 4×4 Hamiltonian $H(\mathbf{p})$, which acts on the 4-component wave function Ψ

$$H(\mathbf{p}) = \begin{pmatrix} h(\mathbf{p}) & t \\ t & -h(\mathbf{p}) \end{pmatrix}, \quad \Psi = \begin{pmatrix} \psi_1 \\ \psi_2 \end{pmatrix}. \quad (5.5)$$

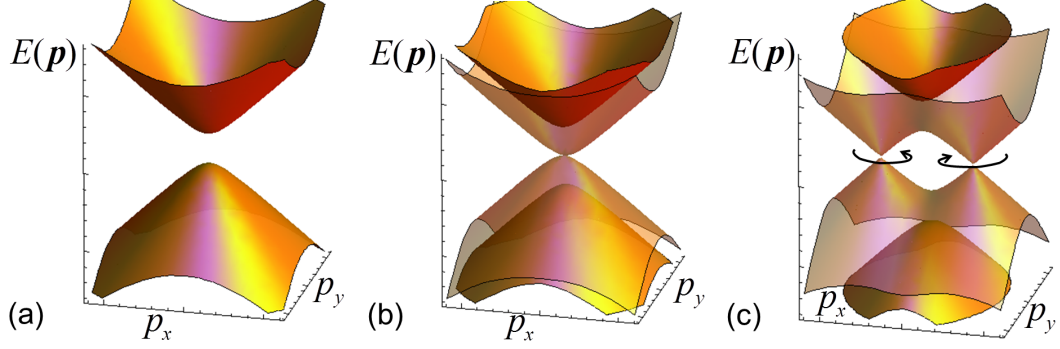


Figure 5.2: The spectrum (5.7) of Hamiltonian (5.6) for different values of magnetic shift: (a) $q = 0$, (b) $q = 2t$, (c) $q = 4t$.

This Hamiltonian was also used in Ref. [105] for description of a thin film. Even though the bulk bands usually contribute to the electronic properties of the real materials [97], we ignore a possible bulk effect in order to highlight the contribution of the surface states. Hamiltonian (5.5) has the spectrum $E(\mathbf{p}) = \pm\sqrt{v^2p^2 + t^2}$, where the energy gap is determined by the tunneling element t . Experimentally, gap varies from 0.25 eV for the ultra-thin 2 nm film to 0.05 eV for the 5 nm film of Bi_2Se_3 [102].

5.3 Spectrum in a parallel field.

Let us now discuss the spectrum of the TI thin film in a parallel magnetic field $\mathbf{B} = B_y \hat{\mathbf{y}}$. In the Landau gauge $\mathbf{A} = zB_y \hat{\mathbf{x}}$, the Peierls substitution $\mathbf{p} \rightarrow \mathbf{p} - e\mathbf{A}$ transforms the Hamiltonian (5.5) into

$$H(\mathbf{p}) = \begin{pmatrix} h(\mathbf{p} - \mathbf{q}/2) & t \\ t & -h(\mathbf{p} + \mathbf{q}/2) \end{pmatrix}, \quad \mathbf{q} = eB_y d \hat{\mathbf{x}}. \quad (5.6)$$

As discussed in Chapters 2 and 3 the in-plane magnetic field leads to a shift of the in-plane momenta q on the opposite surfaces. The Zeeman term can be included in the definition of q ¹. The spectrum of Hamiltonian (5.6) is [105]

$$E(\mathbf{p}) = \pm \left\{ v^2 p_y^2 + \left[(t^2 + v^2 p_x^2)^{1/2} \pm \frac{vq}{2} \right]^2 \right\}^{1/2}. \quad (5.7)$$

The evolution of the spectrum for growing magnetic field q is shown in Fig. 5.2. For zero magnetic field $q = 0$, the spectrum is gapped [Fig. 5.2(a)]. For small magnetic field, the double generate bands split into two bands. For critical magnetic field $q = 2t$, the gap closes [Fig. 5.2(b)], and the two Dirac cones are created at positions $\mathbf{p} = \sqrt{q^2/4 - t^2}$ [Fig. 5.2(c)] with growth of the magnetic field. Compare, the spectrum of a graphene bilayer shown in Fig. 2.2 (Chapter 2) with a spectrum of TI film shown above. In case of the TI film, finite magnetic field $q = 2t$ is needed to close the gap, and only then the Dirac cones are created. In contrast, the bare spectrum of a graphene bilayer is gapless, and therefore the spectrum splits into the two Dirac cones already for infinitesimal field q . Below, we shall be interested in the limit $t \rightarrow 0$, where the spectrum is given merely by the two shifted Dirac cones.

$$E(\mathbf{p}) = \pm v \left| \mathbf{p} \pm \frac{\mathbf{q}}{2} \right|, \quad (5.8)$$

¹In the presence of the Zeeman term, the magnetic shift becomes $q = B_y(ed - 2g\mu_B/v)$, where μ_B is the Bohr magneton, $v = 5 \times 10^5$ m/s, and $g \sim 1$ is the g -factor. The Zeeman contribution is comparable to the orbital contribution only for a small thickness $d = 2g\mu_B/ev \sim 0.2$ nm. So, the Zeeman contribution can be neglected for the films used in experiments, where $d > 1$ nm.

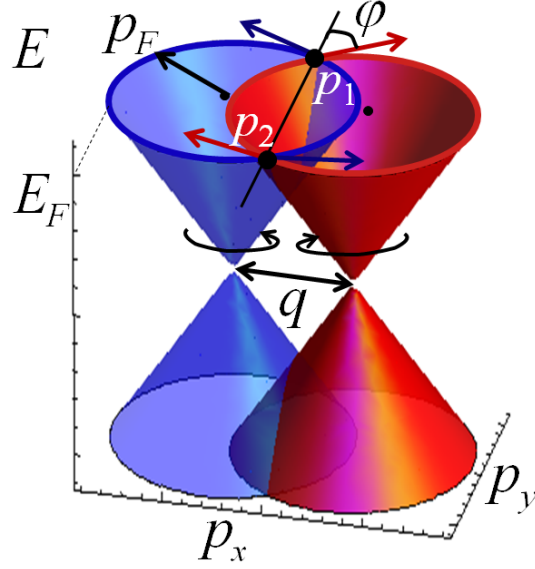


Figure 5.3: Electronic spectrum (5.8) of the thin film consists of the two Dirac cones spin-polarized in the opposite directions as shown with circulating arrows. The Dirac cones are shifted by q_x due to the parallel magnetic field B_y . Tunneling between the Dirac cones is dominated by the electrons with momenta \mathbf{p}_1 and \mathbf{p}_2 where the shifted Fermi circles $|\mathbf{p} \pm \mathbf{q}/2| = p_F$ intersect.

as shown in Fig. 5.3. A similar shift of the Dirac cones was discussed for a twisted graphene bilayer [63].

5.4 Tunneling current in a parallel field.

When a small potential difference V is applied between the opposite surfaces of the film, the out-of-plane tunneling current per unit area

$$j_\alpha = (j_0, \mathbf{j}) = it \left(\psi_1^\dagger \hat{\sigma}_\alpha \psi_2 - \psi_2^\dagger \hat{\sigma}_\alpha \psi_1 \right) \quad (5.9)$$

flows between the opposite surfaces, where ψ_1 and ψ_2 are the annihilation operators on the corresponding surface states. Here, we put $\hbar = 1$ for simplicity and reestablish the correct units in the end of calculation. So, the tunneling current is written in a convenient four-component form, such that $e j_0$ and $\frac{\hbar}{2} \mathbf{j}$ are the charge and spin currents. Using the linear-response theory for w as a perturbation [108], the tunneling conductances per unit area $G_\alpha = \lim_{V \rightarrow 0} \langle j_\alpha \rangle / V$ can be expressed through the spectral functions $A_{1,2}(E, \mathbf{p})$ evaluated at the Fermi energy E_F as

$$G_\alpha = \frac{w^2 e}{2\pi} \int d^2 p \operatorname{Tr} \left[\hat{\sigma}_\alpha A_1 \left(E_F, \mathbf{p} + \frac{\mathbf{q}}{2} \right) A_2 \left(E_F, \mathbf{p} - \frac{\mathbf{q}}{2} \right) \right]. \quad (5.10)$$

Here, $G_\alpha = (G_0, \mathbf{G})$ has four components, where $e G_0$ and $\frac{\hbar}{2} \mathbf{G}$ correspond to the tunneling conductance for charge and spin currents. The spectral functions $A_{1,2}$ are given in the momentum space

$$A_{1,2} \left(E_F, \mathbf{p} \pm \frac{\mathbf{q}}{2} \right) = \delta \left(v \left| \mathbf{p} \mp \frac{\mathbf{q}}{2} \right| - E_F \right) \left| \mathbf{p} \mp \frac{\mathbf{q}}{2}, \pm \right\rangle \left\langle \mathbf{p} \mp \frac{\mathbf{q}}{2}, \pm \right|, \quad (5.11)$$

where the opposite signs correspond to the opposite surfaces ψ_1 and ψ_2 , and the spinors $|\mathbf{p}, \pm\rangle$ are defined in Eq. (5.3). Using Eqs. (5.10) and (5.11), let us first calculate the tunneling conductance G_0 for the charge current

$$G_0 = \frac{w^2 e}{2\pi v^2} \int d^2 p \delta \left(\left| \mathbf{p} - \frac{\mathbf{q}}{2} \right| - p_F \right) \delta \left(\left| \mathbf{p} + \frac{\mathbf{q}}{2} \right| - p_F \right) f(\mathbf{p}),$$

$$f(\mathbf{p}) = \left| \left\langle \mathbf{p} - \frac{\mathbf{q}}{2}, + \right| \left| \mathbf{p} + \frac{\mathbf{q}}{2}, - \right\rangle \right|^2, \quad (5.12)$$

where $p_F = E_F/v$ is the Fermi momentum. According to Eq. (5.12), the tunneling current is carried by the electrons that have the in-plane momenta \mathbf{p}_1 and \mathbf{p}_2 corresponding to the intersection points of the shifted Fermi circles $|\mathbf{p} \pm \mathbf{q}/2| = p_F$, as shown by the thick dots in Fig. 5.3. In addition, there is a contribution $f(\mathbf{p})$ due to the non-trivial scalar product between the spinors (5.3) corresponding to the Fermi circles.

As a warm up, let us first consider the case where there is no spin-momentum locking, so $f(\mathbf{p}) = 1$ and Eq. (5.12) gives

$$G_0^{(1)}(q) = \frac{2t^2 e p_F^2}{\pi \hbar^3 v^2 q \sqrt{4p_F^2 - q^2}}. \quad (5.13)$$

The tunneling conductance $G_0^{(1)}$ diverges at $q = 0$ and $q = 2p_F$, as shown by the dashed line in Fig. 5.4(a). For a small magnetic field $q \ll 2p_F$, the tunneling conductance is large because of the large overlap between the two Fermi circles shown in the left part of Fig. 5.4(b). For an intermediate magnetic field $q \sim p_F$, the Fermi circles intersect only at two points \mathbf{p}_1 and \mathbf{p}_2 , so the tunneling conductance decreases. For $q \sim 2p_F$, the two points \mathbf{p}_1 and \mathbf{p}_2 come together, so the Fermi circles overlap at the locally flat regions as shown in the right part of Fig. 5.3(b), and the tunneling conductance is large again. Once $q > 2p_F$, the two Fermi circles separate, and the tunneling conductance drops to zero. The experimental curve of the tunneling conductance for a GaAs bilayer [106] shows behavior similar to Eq. (5.13), but the divergences at $q = 0$ and $q = 2p_F$ are smeared out due to a finite scattering time τ .

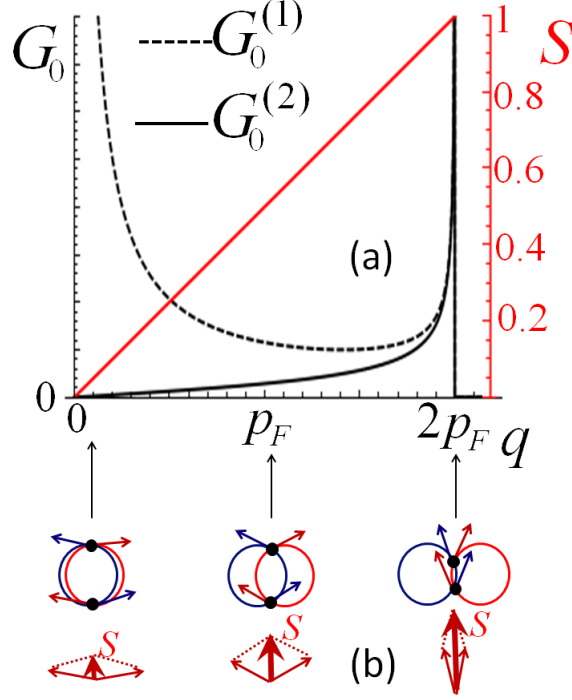


Figure 5.4: (a) The tunneling conductances for spin-unpolarized $G_0^{(1)}$, Eq. (5.13), and spin-polarized $G_0^{(2)}$, Eq. (5.14), Fermi circles are shown by the dashed and solid black lines, respectively. The latter curve $G_0^{(2)}$ corresponds to the negative magnetoresistance. The red curve is the spin polarization (5.16) of the tunneling current, and the right vertical axis shows its value, where 1 corresponds to 100% spin polarization. (b) Schematic views of the shifted Fermi circles $|\mathbf{p} \pm \mathbf{q}/2| = p_F$ for the corresponding values of q . The tunneling is allowed for the momenta \mathbf{p}_1 and \mathbf{p}_2 where the Fermi circles intersect, also shown in Fig. 5.3. The spin polarizations for these momenta are shown by the blue and red arrows corresponding to the ψ_1 and ψ_2 surfaces. The vector sum of the arrows of the same color defines the net spin polarization of the tunneling current, which grows with the increase of q as illustrated in the bottom of panel (b).

Now, let us consider the form-factor $f(\mathbf{p})$ in Eq. (5.12) arising from the spinor eigenstates (5.3) of the Rashba Hamiltonian (5.2). As discussed above, the surface states have opposite spin polarizations. In Figs. 5.3 and 5.4, the polarizations corresponding to the different Fermi circles are shown by the blue and red arrows intersecting at the angle ϕ , the value of which follows from simple trigonometry: $\cos \phi = q/2p_F$. The form-factor $f(\mathbf{p})$ in Eq. (5.12) takes into account an overlap between the spinors on the different Fermi circles and is equal to $f(\mathbf{p}_{1,2}) = \cos^2 \phi$. So, the tunneling conductance (5.12) is multiplied by a factor of $q^2/4p_F^2$ relative to Eq. (5.13)

$$G_0^{(2)}(q) = \frac{t^2 e q}{2\pi \hbar^3 v^2 \sqrt{4p_F^2 - q^2}}. \quad (5.14)$$

The tunneling conductance given by Eq. (5.14) is plotted by the solid line in Fig. 5.4(a). In contrast to $G_0^{(1)}$, the tunneling conductance $G_0^{(2)}$ is suppressed as $q \rightarrow 0$, because spin polarizations of the Fermi circles are opposite at the points \mathbf{p}_1 and \mathbf{p}_2 , as shown in Fig 5.4(b) on the left. This is a signature of the opposite spin helicity of the Fermi circles and thus may be used as a way to detect it. For q near $2p_F$, however, the spin configurations are almost aligned, as shown in Fig. 5.4(b), so, $G_0^{(1)}$ and $G_0^{(2)}$ become equal.

The non-trivial spin structure of the Fermi circles not only modifies the tunneling current, but also makes it spin-polarized. Let us define spin polarization as the ratio of the spin current over the charge current

$$\mathbf{S} = \frac{\langle \mathbf{j} \rangle}{\langle j_0 \rangle} = \frac{\mathbf{G}}{G_0}, \quad (5.15)$$

where the second equation follows from the definition of the conductance. Using the property that the eigenstates (5.3) have the well-defined spin orientation (5.4), we obtain from Eq. (5.10)

$$\mathbf{S} = \frac{\mathbf{S}(\mathbf{p}_1 - \mathbf{q}/2) + \mathbf{S}(\mathbf{p}_2 - \mathbf{q}/2)}{2} = \cos \phi \hat{\mathbf{y}} = \frac{ed}{2p_F} \mathbf{B}. \quad (5.16)$$

So, the spin polarization of the tunneling current is determined by the vector sum of the spin directions at the momenta \mathbf{p}_1 and \mathbf{p}_2 . Indeed, in the process of tunneling, the electrons with the in-plane momenta \mathbf{p}_1 and \mathbf{p}_2 move from the “blue” to “red” Fermi circle, carrying the total spin, which is a vector sum of the spins at the momenta \mathbf{p}_1 and \mathbf{p}_2 , in agreement with Eq. (5.16). The helical spin configuration (5.4) is such that the net spin polarization \mathbf{S} is parallel and proportional to \mathbf{B} , as illustrated in Fig. 5.4(b). At $q = 0$, the spins at the points \mathbf{p}_1 and \mathbf{p}_2 are opposite, and the spin polarization of the tunneling current vanishes. At $q = 2p_F$, the spins at the points \mathbf{p}_1 and \mathbf{p}_2 are collinear and the tunneling current is fully spin-polarized. Also, notice that the electron tunneling at \mathbf{p}_1 changes the spin polarization from the “blue” to “red” arrow, thus creating a torque $\mathbf{S}(\mathbf{p}_1 + \mathbf{q}/2) - \mathbf{S}(\mathbf{p}_1 - \mathbf{q}/2)$ in $\hat{\mathbf{x}}$ direction. However, the torque is opposite at \mathbf{p}_2 , so the net torque is zero.

5.5 Experimental relevance.

Let us estimate the critical magnetic field B_y where the Fermi circles almost detach, i.e., where $q = 2p_F$. We take the realistic value $v = 5 \times 10^5$ m/s, assume $d = 5$ nm (5 quintuple layers of Bi_2Se_3) and carrier concentration corresponding to

$E_F = 30$ meV. Using Eq. (5.6) for q , we estimate the critical value of the field as $B_y = 20$ T. This value is experimentally accessible and can be further reduced by either increasing the thickness d or decreasing the Fermi momentum p_F .

An intriguing strong negative magnetoresistance effect was reported for the Sn-doped films of Bi_2Te_3 in Ref. [107]. A weak in-plane magnetic field less than 1 T causes a large drop of the out-of-plane resistance R_{zz} as shown in Fig. 4(c) of Ref. [107]. Since $R_{zz} \propto 1/G_0$, a decrease in resistance R_{zz} corresponds to an increase in conductance G_0 , which qualitatively agrees with plot of $G_0^{(2)}$ vs q shown in Fig. 5.4(a). In addition, the effect of Sn doping was studied in Ref. [107]. The Sn doping leads to a decrease of carrier concentration and p_F , which is corroborated by an increase of resistance R_{zz} in the experiment. At the same time, the magnitude of negative magnetoresistance increases dramatically with doping, as shown in Fig. 4(a,b) of Ref. [107]. This observation is consistent with Eq. (5.14), where the conductance $G_0^{(2)}$ increases when p_F decreases (for $q < 2p_F$). However, our idealized model may be not fully applicable to the experiment [107], where polycrystalline films were studied. Grain boundaries and defects may host topological states [109, 110], which can contribute considerably to the tunneling current.

Equation (5.14) was obtained for an idealized situation where the temperature T and the inverse scattering time $1/\tau$ are much lower than the Fermi energy E_F . For realistic TI materials, the scattering rate $1/\tau$ is finite due to impurities or other mechanisms. When $1/\tau$, T , and fluctuations of chemical potential [111] become comparable with E_F , the predicted effects would be smeared out. However, the majority of TIs are not strongly-correlated systems, so the effects of interactions

between electrons should not alter the predicted effects considerably.

While the isotropic Dirac cone approximation is valid for small energies in Eq. (5.3), it is not exact for higher energies, where energy spectrum has hexagonal warping anisotropy, and spin polarization has an out-of-plane component. In this case, the analytic formula (5.14) is not applicable, but can be easily generalized. The appropriate spectrum $E(\mathbf{p})$ and spinors $|\mathbf{p}, \pm\rangle$ should be substituted into Eq. (5.11), and the tunneling conductance obtained from Eq. (5.10). In general, the tunneling conductance may depend on the in-plane orientation of the magnetic field \mathbf{B} due to anisotropy of the surface state dispersion. This effect can be utilized to obtain information about hexagonal warping experimentally.

5.6 Conclusions.

We have theoretically studied tunneling conductance between the opposite surface states in a thin film of TI when a parallel magnetic field is applied. The helical spin polarization and the overlap between the Fermi circles result in the unusual spin polarization of the tunneling current. Our theoretical results are qualitatively consistent with the experiment [107]. However, further experimental verifications are needed. First, magnetoresistance in Ref. [107] was measured for a relatively weak magnetic field $B < 1$ T. We predict *non-monotonous* behavior of magnetoresistance for a large magnetic field: the conductance (resistance) could sharply decrease (increase) when the magnetic field exceed the condition $B > 2p_F/ed$. Second, a measurement of the spin polarization of the tunneling current is desirable.

This effect may be important for spintronic applications and may pave the way to observation of spin-polarized currents in TIs.

Chapter 6: Chiral structure in the pseudogap phase of cuprates

6.1 Introduction.

The nature of the pseudogap phase in underdoped cuprate superconductors has been a long-standing problem [112]. A series of optical measurements [113–116] revealed gyrotropy in this state. It was observed that the polarizations of incident and reflected light differ by a small angle θ_K , called the polar Kerr angle. Initially, these experiments were interpreted as the evidence for spontaneous time-reversal symmetry breaking. Theoretical models [117–120] derived optical gyrotropy from the anomalous Hall effect. In these scenarios, the order parameter is equivalent to an intrinsic magnetic field perpendicular to the layers, which permeates the system and points inward and outward at the opposite surfaces of a crystal. Therefore, the Kerr angle should have opposite signs at the opposite surfaces of the crystal.

However, recent reports [121, 122] found that the Kerr angle has the same sign at the opposite surfaces of a sample. Therefore, the observed gyrotropy is not consistent with the time-reversal-symmetry breaking due to a magnetic order and should be interpreted as the evidence for natural optical activity due to chiral symmetry breaking [123]. Systems with helical structures, such as cholesteric liquid crystals and some organic molecules, typically exhibit optical gyrotropy and the

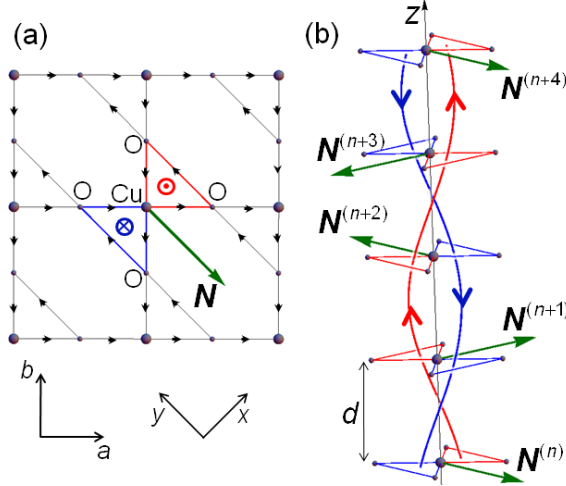


Figure 6.1: (a) Loop-current order in a CuO_2 plane. Black arrows show directions of microscopic persistent currents between copper and oxygen atoms. Green arrow shows the anapole moment \mathbf{N} . (b) Chiral order constructed on a series of parallel CuO_2 planes. The vector \mathbf{N} rotates by the angle $\pi/2$ from one layer to another, and the period of the structure is fourfold. The blue and red curves are the two magnetic field lines that intertwine in a double helix.

polar Kerr effect. It is important that the sign of the Kerr angle in this case is the same at the opposite surfaces of the system, in contrast to the gyrotropy produced by a magnetic order (see Chaps. 11 and 12 in Ref. [123]).

Theoretical scenarios for appearance of chiral order in cuprates were proposed in Refs. [122, 124]. Three possible orders were studied phenomenologically in Ref. [122]: 3-plane rotation of distorted Fermi circles, 4-plane rotation of a structure with an in-plane ferroelectric moment, and 4-plane rotation of an in-plane density wave with period 3. A formula for gyrotropy of a chiral metal was derived in Ref. [124] in terms of the Berry curvature in momentum space. However, Ref. [125] questioned applicability of the implied assumption of coherent electron

motion between the layers in Ref. [124]. X-ray circular dichroism due to chiral order was discussed in Ref. [126].

6.2 Helical order of the anapole moments.

Here, we propose a novel chiral state, which could account for the polar Kerr effect in cuprates without requiring coherent electron motion between the layers. The starting point for our construction is the model of persistent loop currents by Simon and Varma [127] shown in Fig. 6.1(a). The configuration of persistent currents is such that the total magnetic flux through the lattice unit cell vanishes. The anomalous Hall effect is zero [128], and this state does not exhibit magnetic gyrotropy. The loop-current order [129] is characterized by the anapole moment \mathbf{N} [130, 131], shown by the green arrow in Fig. 6.1(a) and defined as

$$\mathbf{N} = \int d^2r [\mathbf{m}(\mathbf{r}) \times \mathbf{r}] = \frac{1}{2c} \int d^2r \mathbf{r}^2 \mathbf{j}(\mathbf{r}). \quad (6.1)$$

Here $\mathbf{m}(\mathbf{r})$ and $\mathbf{j}(\mathbf{r})$ are the microscopic densities of the magnetic moment and electric current, and the integral is taken over the unit cell. The square symmetry of the lattice allows four possible orientations [132] for the vector \mathbf{N} , which can be obtained by progressive $\pi/2$ rotations of the configuration shown in Fig. 6.1(a).

We propose a novel chiral state where the anapole moments $\mathbf{N}^{(n)}$ in consecutive CuO_2 layers labeled by the integer number n are rotated by $\pi/2$, so that they trace out a helix, as shown in Fig. 6.1(b). This arrangement is somewhat similar to

cholesteric liquid crystals¹. This spiral structure breaks three-dimensional inversion symmetry and can be qualitatively visualized as follows. The in-plane triangular loop currents in Fig. 6.1(a) produce perpendicular magnetic fields of the opposite signs shown by the circled red dot and blue cross at the centers of the loops. When the anapole moments $\mathbf{N}^{(n)}$ are arranged in the spiral structure in Fig. 6.1(b), the red and blue magnetic field lines, propagating from one layer to another, form a double helix due to twisting of $\mathbf{N}^{(n)}$.

The chiral structure is characterized by a pseudoscalar order parameter Ξ changing sign upon inversion

$$\Xi = \langle \hat{\mathbf{z}} \cdot [\mathbf{N}^{(n)} \times \mathbf{N}^{(n+1)}] \rangle, \quad (6.2)$$

where $\hat{\mathbf{z}}$ is the unit vector along the z axis. If the anapole vector $\mathbf{N}^{(n)}$ is static, Eq. (6.2) does not need the brackets for averaging. However, if the vector $\mathbf{N}^{(n)}$ fluctuates, the brackets in Eq. (6.2) represent thermodynamic and, possibly, quantum [133] averaging. The chiral order parameter Ξ is a local correlation function of the orientations of $\mathbf{N}^{(n)}$ in the neighboring layers and does not require long-range order in $\mathbf{N}^{(n)}$. Spontaneous chiral symmetry breaking is known for other systems [134,135]. The configuration with $\pi/2$ rotations in Fig. 6.1(b) maximizes Ξ for a given absolute value of N . Notice that Eq. (6.2) is similar to the Dzyaloshinskii-

¹However, the director in cholesterics does not have an arrow, whereas the vector \mathbf{N} does. For a director without an arrow, the structure in Fig. 6.1(b) would have two layers in the unit cell and would not be chiral. Since the anapole moment \mathbf{N} does have an arrow, the structure in Fig. 6.1(b) has four layers in the unit cell and is chiral, because it breaks three-dimensional inversion symmetry.

Moriya interaction for spins and to the Lifshitz invariant $\mathbf{N} \cdot [\nabla \times \mathbf{N}]$ with $\nabla = \hat{z} \partial_z$ in the continuous limit.

6.3 Electrodynamics of gyrotropic media

In electrodynamics of media [123], natural optical activity arises when inversion symmetry is broken and the expansion of the dielectric tensor $\varepsilon_{\mu\nu}(\omega, \mathbf{k})$ in powers of the wave vector \mathbf{k} has a nonvanishing first-order term

$$\varepsilon_{\mu\nu}(\omega, \mathbf{k}) = \varepsilon_{\mu\nu}(\omega, 0) + i\gamma(\omega)\epsilon_{\mu\nu z}k_z. \quad (6.3)$$

Here $\epsilon_{\mu\nu\lambda}$ is the antisymmetric tensor, and k_z is the wave vector of an electromagnetic wave propagating along the z axis. The second term in Eq. (6.3) represents a nonlocal effect along the z axis and is responsible for gyrotropic properties of the medium. The polar Kerr angle θ_K is determined by the following formula [136] to the first order in the coefficient γ in Eq. (6.3)

$$\tan \theta_K(\omega) = \frac{\omega}{c} \mathcal{I}m \left[\frac{\gamma(\omega)}{1 - \varepsilon(\omega)} \right]. \quad (6.4)$$

It is clear that nonzero Kerr angle requires an imaginary part, i.e., dissipation, either in $\varepsilon(\omega)$ or $\gamma(\omega)$. Below, we derive the second term in Eq. (6.3) for the spiral structure in Fig. 6.1(b).

6.4 Magnetoelectric effect in a single CuO₂ plane.

First let us consider a single CuO₂ plane with loop currents in Fig. 6.1(a). Integration of the electron field, schematically shown in the left diagram in Fig. 6.2(a), gives an effective action for the electromagnetic field with a magnetoelectric term [123, 137]. By symmetry, it has the form [129]

$$S_{\text{ME}} = \int d\omega d^2r \beta(\omega) B_z(-\omega) [\mathbf{N} \times \mathbf{E}(\omega)]_z. \quad (6.5)$$

Here $\mathbf{E} = (E_x, E_y)$ is the in-plane electric field, B_z is the out-of-plane magnetic field, and $\mathbf{N} = (N_x, N_y)$ is the in-plane anapole moment. Given Eq. (6.1), the anapole moment \mathbf{N} is the time-reversal-odd and parity-odd vector, so Eq. (6.5) has the correct symmetry structure. It is represented graphically by the right diagram in Fig. 6.2(a). Equation (6.5) is written in the frequency representation for the electromagnetic fields, whereas \mathbf{N} is taken to be static, i.e. having zero frequency, and $\beta(\omega)$ is a frequency-dependent coefficient. The effective action in Eq. (6.5) is written in the continuous, long-wavelength limit by averaging the electromagnetic fields over distances longer than the unit cell of the lattice.

By taking a variation of Eq. (6.5), we find that an in-plane electric field induces an out-of-plane magnetization

$$M_z(\omega) = \frac{\delta S_{\text{ME}}}{\delta B_z(-\omega)} = \beta(\omega) [\mathbf{N} \times \mathbf{E}(\omega)]_z. \quad (6.6)$$

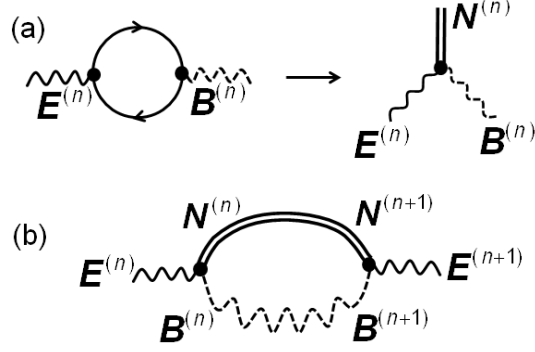


Figure 6.2: (a) Left: Feynman diagram for the effective action of electromagnetic fields (wavy lines), obtained by integrating out the electron field (solid lines with arrows). Right: The magnetoelectric term in the effective action, Eq. (6.5), where the double line represents the anapole moment \mathbf{N} . (b) Coupling between the magnetoelectric terms at the neighboring layers produces the effective action for the electric field in Eq. (6.9). The dashed wavy line represents the magnetic field propagator, and the double solid line represents the interlayer correlator of the anapole moments in Eq. (6.2).

Physical interpretation is clear by symmetry in Fig. 6.1(a). An in-plane electric field $\mathbf{E} \perp \mathbf{N}$ promotes electron transfer from one triangular loop to another, thus breaking symmetry and making one loop current stronger, which results in the net perpendicular magnetization.

Similarly, an out-of-plane magnetic field induces an in-plane electric polarization

$$\mathbf{P}(\omega) = \frac{\delta S_{\text{ME}}}{\delta \mathbf{E}(-\omega)} = \beta(\omega) [\mathbf{N} \times \mathbf{B}_z(\omega)]. \quad (6.7)$$

The perpendicular magnetic field B_z lowers the energy for one loop current and increases for another in Fig. 6.1(a), which results in electron transfer between the loops and the in-plane electric polarization $\mathbf{P} \perp \mathbf{N}$.

6.5 Interlayer coupling and the gyrotropic term.

Now let us consider many parallel layers labeled by the integer number n . In this case, we expect a magnetic coupling between magnetizations at the neighboring layers

$$S_{\text{MM}} = - \int d\omega d^2r \sum_n \Lambda M_z^{(n)}(\omega) M_z^{(n+1)}(-\omega). \quad (6.8)$$

This term should be derived microscopically from the distribution of electric currents inside the unit cell comparable to the interlayer distance d . Here we simply write Eq. (6.8) by symmetry for the long-wavelength fields M_z with a phenomenological coefficient Λ . We assume that the interlayer coupling between magnetizations is instantaneous; i.e., Λ is frequency independent. This assumption is valid when the interlayer distance d is much smaller than the wavelength of light: $d \ll \lambda = 2\pi/k_z$.

Substituting Eq. (6.6) into Eq. (6.8), we obtain an effective action for the electric fields in the multilayer system

$$S_{\text{EE}} = - \int d\omega d^2r |\beta(\omega)|^2 \sum_n \Lambda [\mathbf{N}^{(n)} \times \mathbf{E}^{(n)}(\omega)]_z [\mathbf{N}^{(n+1)} \times \mathbf{E}^{(n+1)}(-\omega)]_z, \quad (6.9)$$

where we used the standard relation $\beta(-\omega) = \beta^*(\omega)$ for a linear response function. Figure 6.2(b) illustrates this calculation diagrammatically. By coupling the magnetoelectric vertices shown in Fig. 6.2(a) and integrating out the magnetic field propagator shown by the dashed wavy line, we obtain the effective action for the electric field in Eq. (6.9). The double solid line represents the interlayer correlator of the anapole moments in Eq. (6.2).

Let us choose the x and y axes along the crystallographic direction $\mathbf{a} + \mathbf{b}$ and $\mathbf{b} - \mathbf{a}$ in Fig. 6.1, so that the vectors $\mathbf{N}^{(n)} = -\mathbf{N}^{(n+2)}$ are along x for odd n and y for even n . Expanding the vector products in Eq. (6.9), we find two terms in the sum, for odd and even n . Changing the variable $n \rightarrow n - 1$ in the latter sum, we find

$$S_{\text{EE}} = \int d\omega d^2r |\beta(\omega)|^2 \sum_{n \text{ odd}} \Lambda N_x^{(n)} N_y^{(n+1)} E_y^{(n)}(\omega) [E_x^{(n+1)}(-\omega) - E_x^{(n-1)}(-\omega)]. \quad (6.10)$$

Using Eq. (6.2), taking the continuous limit $z = nd$, where $E_x^{(n+1)} - E_x^{(n-1)} = 2d(\partial E_x/\partial z)$ and $2d \sum_{n \text{ odd}} = \int dz$, and integrating by parts in z , we get

$$S_{\text{EE}} = -\frac{\Xi\Lambda}{2} \int d\omega d^3r |\beta(\omega)|^2 \hat{\mathbf{z}} \cdot \left[\mathbf{E}(\omega) \times \frac{\partial \mathbf{E}(-\omega)}{\partial z} \right], \quad (6.11)$$

or, equivalently,

$$S_{\text{EE}} = \frac{\Xi\Lambda}{2} \int d\omega d^3r |\beta(\omega)|^2 \mathbf{E}(\omega) \cdot [\nabla_z \times \mathbf{E}(-\omega)]. \quad (6.12)$$

Comparing Eq. (6.11) with the standard expression

$$S = \frac{1}{8\pi} \int d\omega d^3k \varepsilon_{\mu\nu}(\omega, \mathbf{k}) E_\mu(\omega, \mathbf{k}) E_\nu(-\omega, -\mathbf{k}), \quad (6.13)$$

we obtain the coefficient γ in the second term in Eq. (6.3)

$$\gamma(\omega) = 4\pi\Xi\Lambda|\beta(\omega)|^2. \quad (6.14)$$

Equation (6.14) shows that the gyrotropic coefficient $\gamma(\omega)$ is determined by the chiral order parameter Ξ , the interlayer magnetic coupling Λ , and the magnetoelectric coefficient $\beta(\omega)$. The sign of γ depends on the sign of Ξ .

The above derivation was presented for equally spaced CuO_2 layers. However, many cuprates have the bilayer structure, where the interlayer distances alternate between $d \mp \Delta d$. In this case, the interlayer coupling coefficient in Eq. (6.8) is $\Lambda^{(n)} = \Lambda \pm \zeta$ for even and odd n . As a result, we find an additional term, which is similar to Eq. (6.10), but with $\Lambda \rightarrow -\zeta$ and $E_x^{(n+1)} - E_x^{(n-1)} \rightarrow E_x^{(n+1)} + E_x^{(n-1)} = 2E_x$. This term contributes an off-diagonal symmetric term to the dielectric tensor $\varepsilon_{xy} = \varepsilon_{yx} = -4\pi\Xi\zeta|\beta(\omega)|^2/d$, which becomes diagonal in the crystallographic basis of \mathbf{a} and \mathbf{b}

$$\varepsilon_{aa} = -\varepsilon_{bb} = 4\pi\Xi\zeta|\beta(\omega)|^2/d. \quad (6.15)$$

Thus, we find that the helical structure in the presence of bilayers produces nematicity, i.e. anisotropy between the crystallographic directions \mathbf{a} and \mathbf{b} . This is clear by symmetry in Fig. 6.1(b), where the pairs of layers $(n, n+1)$ have the preferred direction $\mathbf{N}^{(n)} + \mathbf{N}^{(n+1)}$ along \mathbf{a} . Equations (6.14) and (6.15) generate circular and linear dichroism. If $\Lambda \sim \zeta$, the linear dichroism is much stronger than the circular one because $d \ll \lambda = 2\pi/k_z$.

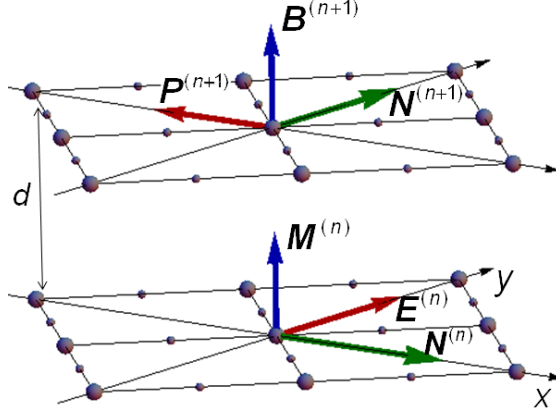


Figure 6.3: Schematic illustration of the rotation of electric polarization for the chiral state shown in Fig. 6.1(b). The electric field $\mathbf{E}^{(n)}$ at the bottom layer induces the magnetization $\mathbf{M}^{(n)}$, which couples to the top layer and induces the electric polarization $\mathbf{P}^{(n+1)} \perp \mathbf{E}^{(n)}$ because of the twist in the anapole moments $\mathbf{N}^{(n)} \perp \mathbf{N}^{(n+1)}$.

Figure 6.3 illustrates these results graphically. The electric field component $\mathbf{E}^{(n)} \perp \mathbf{N}^{(n)}$ generates a magnetization $M_z^{(n)}$ at the bottom layer via the magneto-electric effect in Eq. (6.6). The magnetization $M_z^{(n)}$ produces a magnetic field $B_z^{(n+1)}$ in the same direction at the top layer via Eq. (6.8). This magnetic field induces an electric polarization $\mathbf{P}^{(n+1)} \perp \mathbf{N}^{(n+1)}$ at the top layer via the magnetoelectric effect in Eq. (6.7). Taking into account the third layer $n + 2$ (not shown), we find that $\mathbf{P}^{(n+1)} \propto \hat{\mathbf{z}} \times [c_2 \mathbf{E}^{(n+2)} - c_1 \mathbf{E}^{(n)}]$ with some coefficients c_1 and c_2 . For equally spaced layers with $c_1 = c_2$, we get Eq. (6.11). For bilayers with $c_1 \neq c_2$, we get the additional nematic term in Eq. (6.15).

6.6 Experimental relevance.

Let us discuss possible experimental evidence for the proposed chiral order in cuprates. Neutron scattering measurements [138–140] provide support for the loop currents shown in Fig. 6.1(a). However, the NMR experiments [141] find no evidence for the local magnetic fields predicted by this model. So, the experimental situation remains controversial. A survey of experimental evidence supporting loop currents is presented in Ref. [142].

Although the loop-current order in Fig. 6.1(a) breaks rotational symmetry in the plane as specified by the vector \mathbf{N} , the neutron scattering measurements [138–140] always observe the full rotational symmetry. This may be due to domains with different \mathbf{N} , but the spiral order shown in Fig. 6.1(b) also provides a natural explanation. While the system has the tendency to break rotational symmetry in each CuO_2 layer, we argue that it tries to restore macroscopic symmetry by orienting the vectors \mathbf{N} orthogonally in the neighboring layers, which is consistent with the spiral structure.

Moreover, Refs. [138, 139] concluded that the microscopic magnetic moments are not perpendicular to the layers, as expected from the loop currents in Fig. 6.1(a), but have an in-plane component. This effect can be explained by the spiral order in Fig. 6.1(b) [143]. Since the magnetic field lines are twisted in a double-helix structure, they are naturally tilted with an in-plane component. In the presence of \mathbf{N} , the energy of the system contains the term $\mathbf{N} \cdot [\nabla \times \mathbf{B}] = \mathbf{B} \cdot [\nabla \times \mathbf{N}]$ [131]. Since it is linear in \mathbf{B} , whereas magnetic energy goes as \mathbf{B}^2 , the system develops

an equilibrium in-plane magnetic field $\mathbf{B} \propto [\nabla \times \mathbf{N}]$ parallel to \mathbf{N} in Fig. 6.1(b), in qualitative agreement with Refs. [138, 139]. Moreover, the total energy decreases as $-|\nabla \times \mathbf{N}|^2$, which favors the spiral structure.

Finally, the recent x-ray measurements [144–146] found doubling of the unit cell in $\text{YBa}_2\text{Cu}_3\text{O}_{7-x}$ in the z direction². Given the bilayer structure of $\text{YBa}_2\text{Cu}_3\text{O}_{7-x}$, the new unit cell contains four CuO_2 layers. The fourfold period is consistent with the spiral order shown in Fig. 6.1(b).

For bilayer materials, the spiral structure in Fig. 6.1(b) naturally produces nematicity, where the oxygen atoms to the left and right of the copper atom in Fig. 6.1(a) are not equivalent to the oxygen atoms above and below. This nematic symmetry is in qualitative agreement with the pattern observed in the scanning tunneling measurements [147], although the same pattern was observed experimentally in bilayer and single-layer cuprates.

6.7 Conclusion.

We propose a fourfold chiral state for cuprates obtained by twisting Varma’s loop-current order by $\pi/2$ in consecutive CuO_2 layers. We show that this state exhibits natural optical activity and derive the gyrotropic coefficient. For bilayer compounds, we also find nematicity and linear dichroism. Our model is based on magnetic coupling between the CuO_2 layers and does not require coherent electron tunneling between the layers and long-range order in the chiral structure. Other

²Experiments [144–146] also found the biaxial in-plane wave vectors $(q_x, 0)$ and $(0, q_y)$ for the structure. Here we study the conceptually simplest case where the order parameter is uniform in the plane with $q_x = q_y = 0$. Generalization to nonzero q_x and q_y requires a separate study.

models for the polar Kerr effect in cuprates invoked magnetoelectric effects [148] and coupling between loop currents with different \mathbf{N} [128], but considered only a single layer, rather than the spiral multilayer structure.

Chapter A: Appendix

A.1 Edge states in the original Shockley model

In Sec. 4.2, the Schrödinger equation for the wave function $\Psi(z)$ was given in a recursive form for the integer coordinate $z \geq 1$. The main question is whether the recursion generates a decaying function $\Psi(z) \rightarrow 0$ as $z \rightarrow \infty$, which represents an edge state, or an increasing function $\Psi(z) \rightarrow \infty$ as $z \rightarrow \infty$, which is unphysical. Below, we use the generating function method to find convergence criterion for the edge-state solution $\Psi(z)$. The Schrödinger equation for the original Shockley model (4.1) is

$$V\Psi(z) + (U - E)\Psi(z + 1) + V^\dagger\Psi(z + 2) = 0, \quad (\text{A.1})$$

$$V = \begin{pmatrix} 0 & t_2 \\ 0 & 0 \end{pmatrix}, \quad U = \begin{pmatrix} 0 & t_1 \\ t_1 & 0 \end{pmatrix}, \quad (\text{A.2})$$

where $\Psi(z) = [\psi_a(z), \psi_b(z)]^T$ and $z \geq 1$, whereas the boundary condition is

$$(U - E)\Psi(1) + V^\dagger\Psi(2) = 0. \quad (\text{A.3})$$

Let us multiply the z -th Eq. (A.1) by the $(z - 1)$ -th power of an auxiliary complex variable q and take a sum for $z \geq 1$

$$\sum_{z=1}^{\infty} q^{z-1} [V\Psi(z) + (U - E)\Psi(z + 1) + V^\dagger\Psi(z + 2)] = 0. \quad (\text{A.4})$$

Introducing the generating function

$$G(q) = \sum_{z=1}^{\infty} q^{z-1} \Psi(z), \quad (\text{A.5})$$

Eq. (A.4) can be written as

$$[q^2V + q(U - E) + V^\dagger]G(q) = V^\dagger\Psi(1), \quad (\text{A.6})$$

where we utilized the boundary condition (A.3). From Eq. (A.6), we obtain the generating function in terms of $\Psi(1)$

$$G(q) = [q^2V + q(U - E) + V^\dagger]^{-1} V^\dagger \Psi(1), \quad (\text{A.7})$$

In order to investigate convergence of $\Psi(z)$, we use the following proposition

Proposition 1. *A rational generating function $G(q)$ corresponds to an edge state, i.e. $\Psi(z) \rightarrow 0$ as $z \rightarrow \infty$, if and only if all poles $q_{j=1,2,3,\dots}$ of $G(q)$ have the absolute values greater than one, $|q_j| > 1$.*

Indeed, a rational function with the poles q_j can be transformed to the form $G(q) = \sum_j \frac{f_j(q)}{(q - q_j)^{n_j}}$, where $f_j(q)$ is a polynomial function, and n_j is the order of

the pole q_j . Consider a simple example of the first-order pole $G(q) = \frac{q_1}{q_1 - q} = \sum_z (q/q_1)^z$, which corresponds to the geometric progression. According to Eq. (A.5), the expansion coefficients give the wave function $\Psi(z) = 1/q_1^{z-1}$. Then, the absolute values of the pole $|q_1| < 1$, $|q_1| = 1$, and $|q_1| > 1$ correspond, respectively, to an un-physical growing solution $\Psi(z) \rightarrow \infty$ at $z \rightarrow \infty$, a bulk state $\Psi(z) = e^{ikz}$, and a decaying edge state $\Psi(z) \rightarrow 0$ as $z \rightarrow \infty$. The case of a more complicated $G(q)$ can be reduced to the above simple consideration.

Now let us use Proposition 1 to investigate convergence of $\Psi(z)$. Using Eq. (A.7) and the expressions for U and V in Eq. (A.2), we find

$$G(q) = \frac{\psi_a(1) t_2}{(t_1 + t_2 q)(t_2 + t_1 q) - E^2 q} \begin{pmatrix} t_1 + t_2 q \\ E q \end{pmatrix}. \quad (\text{A.8})$$

The poles of Eq. (A.8) are given by the zeros q_1 and q_2 of the denominator, unless they are canceled out by zeros in the numerator. Using Vieta's formulas for the quadratic equation in the denominator, we obtain $q_1 q_2 = 1$. So, if q_1 is greater than one, $|q_1| > 1$, then q_2 is less than one, $|q_2| < 1$. Using Proposition 1, we conclude that there is no edge state if the generating function $G(q)$ in Eq. (A.8) has two poles. In order to obtain an edge state, we need to reduce the number of poles of the generating function $G(q)$. Notice that, if we put $E = 0$, one pole is canceled out, and $G(q)$ greatly simplifies

$$G(q) = \frac{1}{1 + (t_1/t_2)q} \begin{pmatrix} 1 \\ 0 \end{pmatrix}, \quad (\text{A.9})$$

and the edge state exists if

$$|t_2/t_1| > 1. \quad (\text{A.10})$$

A.2 Energy of the edge states in the generalized Shockley model

In this section, we use the generating function method to prove that an edge eigenstate for Hamiltonian (4.27) can exist only for the eigenenergy $E = 0$. Like in the previous section, Hamiltonian (4.27) can be given in a recursive form Eq. (A.1) with the following U and V

$$V = \begin{pmatrix} 0 & t_2^* \\ t_3 & 0 \end{pmatrix}, \quad U = \begin{pmatrix} 0 & t_1^* \\ t_1 & 0 \end{pmatrix}. \quad (\text{A.11})$$

Using Eq. (A.7) we obtain the generating function

$$G(q) = \frac{N(q)}{D(q)}, \quad (\text{A.12})$$

where the numerator

$$N(q) = \begin{pmatrix} Eq & \beta(q) \\ \alpha(q) & Eq \end{pmatrix} \begin{pmatrix} \psi_1 \\ \psi_2 \end{pmatrix} \quad (\text{A.13})$$

and denominator

$$D(q) = \alpha(q) \beta(q) - E^2 q^2 \quad (\text{A.14})$$

are defined through the polynomials

$$\alpha(q) = t_3 q^2 + t_1 q + t_2, \quad (\text{A.15})$$

$$\beta(q) = t_2^* q^2 + t_1^* q + t_3^*. \quad (\text{A.16})$$

In Eq. (A.13), the following notation is used for brevity

$$\begin{pmatrix} \psi_1 \\ \psi_2 \end{pmatrix} = V^\dagger \begin{pmatrix} \psi_a(1) \\ \psi_b(1) \end{pmatrix}. \quad (\text{A.17})$$

According to Proposition 1, the poles of Eq. (A.12) determine whether $G(q)$ corresponds to an edge state. The potential poles of $G(q)$ are given by zeros of the quartic polynomial $D(q)$ in the denominator. Thus, let us find the structure of zeros of $D(q)$. Suppose, q_1 is a solution of the quartic equation $D(q_1) = 0$. Then, since $[D(1/q^*)]^* = D(q)/q^2$, $1/q_1^*$ is also a solution of the quartic equation $D(1/q_1^*) = 0$. So, in the most general case, the polynomial $D(q)$ has zeros q_1 and q_2 , as well as $1/q_1^*$ and $1/q_2^*$. Thus, according to Proposition 1, the only way to build an edge state is to have the smallest poles $|q_1| < 1$ and $|q_2| < 1$ canceled out by the zeros of the numerator $N(q)$. So, both components of the vector

$$N(q) = \begin{pmatrix} t_2^* \psi_2 q^2 + [t_1^* \psi_2 + E \psi_1] q + t_3^* \psi_2 \\ t_3 \psi_1 q^2 + [t_1 \psi_1 + E \psi_2] q + t_2 \psi_1 \end{pmatrix} \quad (\text{A.18})$$

must be proportional to $(q - q_1)(q - q_2)$ and, thus, be linearly dependent. Hence, the coefficients in front of the terms q^2 and q^0 should also be linearly dependent and so

$$\psi_1\psi_2(|t_2|^2 - |t_3|^2) = 0. \quad (\text{A.19})$$

If $|t_2| \neq |t_3|$, then $\psi_1\psi_2 = 0$, so the substitution of $\psi_1 = 0$ and $\psi_2 \neq 0$ (or vice versa) in Eq. (A.18) and the requirement, that both components of $N(q)$ are proportional, lead to $E = 0$. The case $|t_2| = |t_3|$ is trivial, because Vieta's formulas for Eq. (A.18) require that $|q_1q_2| = |t_2/t_3| = 1$, which contradicts to the initial assumption that $|q_1| < 1$ and $|q_2| < 1$. Thus, we have proved that the edge states of Hamiltonian (4.27) can only exist for $E = 0$, and there are no other edge states.

A.3 Tight-binding model of Varma's loop-current order

Below, we show that the energy spectrum of Varma's loop-current order has Dirac cones due to a special toroidal symmetry of the problem. We use the three-band Emery Hamiltonian for the CuO_2 lattice tight-binding model shown in Fig. A.1(a)

$$H_E(\mathbf{p}) = \begin{bmatrix} E_c & -2it \sin \frac{p_x}{2} & 2it \sin \frac{p_y}{2} \\ \text{c.c.} & 0 & -4t_1 \sin \frac{p_x - \chi}{2} \sin \frac{p_y - \chi}{2} \\ \text{c.c.} & \text{c.c.} & 0 \end{bmatrix}. \quad (\text{A.20})$$

The Hamiltonian is given in the momentum space and acts on a spinor wave-function $\Psi = [\psi_c \ \psi_x \ \psi_y]^T$ with components corresponding to Cu, O_x and O_y orbitals. The Copper and Oxygen orbitals are separated by the charge-transfer gap $E_c = 3$ eV in

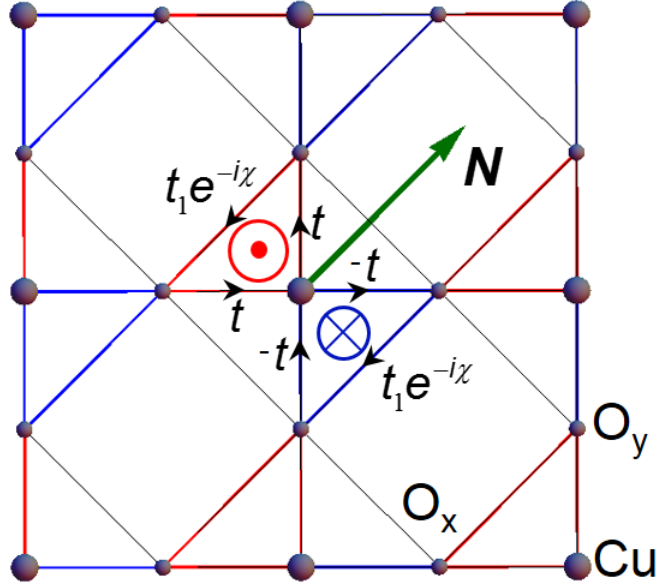


Figure A.1: Tight-binding model of the loop-current order in a CuO_2 plane. The phase χ describes the alternating magnetic fluxes triangles.

energy. The tunneling amplitudes $t = 1$ eV and $t_1 = 0.5$ eV describe the Copper-Oxygen and Oxygen-Oxygen hopping. The sign of t_1 amplitudes is chosen to satisfy the overlap of the Oxygen p orbitals and Copper d orbitals as shown in Ref. [149].

In order to obtain an effective two-band Hamiltonian we write the eigenstate equation for the Hamiltonian (A.20) as

$$E_c \psi_c + T \psi = \lambda \psi_c, \quad (\text{A.21})$$

$$T^\dagger \psi_c + h_{xy} \psi = \lambda \psi. \quad (\text{A.22})$$

Here, we introduce the matrices

$$h_{xy} = \begin{bmatrix} 0 & -4t_1 \sin \frac{p_x - \lambda}{2} \sin \frac{p_y - \lambda}{2} \\ \text{c.c.} & 0 \end{bmatrix}, \quad (\text{A.23})$$

$$T = \begin{bmatrix} -2it \sin \frac{p_x}{2} & 2it \sin \frac{p_y}{2} \end{bmatrix}, \quad (\text{A.24})$$

to explicitly separate the wave-functions on Copper ψ_c and Oxygen orbitals

$$\psi = \begin{bmatrix} \psi_x \\ \psi_y \end{bmatrix}. \quad (\text{A.25})$$

From Eq. (A.21), we solve for

$$\psi_c = -\frac{1}{E_c - \lambda} T \psi, \quad (\text{A.26})$$

and substitute ψ_c in Eq. (A.22)

$$\left(h_{xy} - \frac{1}{E_c - \lambda} T^\dagger T \right) \psi = \lambda \psi. \quad (\text{A.27})$$

For $E_c \gg \lambda \sim t$, it is valid to neglect λ in the denominator in Eq. (A.27), and we obtain an effective two-band Hamiltonian

$$H = h_{xy} - \frac{1}{E_c} T^\dagger T. \quad (\text{A.28})$$

So, using definitions (A.23) and (A.24) we write Eq. (A.28) as

$$H = h_0(\mathbf{p})I + \mathbf{h}(\mathbf{p}) \cdot \boldsymbol{\sigma}, \quad (\text{A.29})$$

where $(I, \sigma_x, \sigma_y, \sigma_z)$ are the identity and Pauli matrices acting in the space of Oxygen orbitals (A.25). The coefficients h are

$$h_0 = -2t_2 \left(\sin^2 \frac{p_x}{2} + \sin^2 \frac{p_y}{2} \right), \quad (\text{A.30})$$

$$h_x = 4 \left(t_2 \sin \frac{p_x}{2} \sin \frac{p_y}{2} - t_1 \sin \frac{p_x - \chi}{2} \sin \frac{p_y - \chi}{2} \right), \quad (\text{A.31})$$

$$h_y = 0, \quad (\text{A.32})$$

$$h_z = -2t_2 \left(\sin^2 \frac{p_x}{2} - \sin^2 \frac{p_y}{2} \right), \quad (\text{A.33})$$

and $t_2 = t^2/E_c = 0.33$ eV.

Let us discuss the implications of the toroidal symmetry \mathcal{TP} . The time-reversal operation transforms the Hamiltonian (A.29) as

$$\mathcal{T} H(\mathbf{p}) = H^*(-\mathbf{p}), \quad (\text{A.34})$$

whereas the inversion operation transforms the Hamiltonian as

$$\mathcal{P} H(\mathbf{p}) = H(-\mathbf{p}), \quad (\text{A.35})$$

Since, the loop-current order has the combined \mathcal{TP} symmetry, the Hamiltonian

should be invariant under the operation of both symmetries

$$H(\mathbf{p}) = \mathcal{TP} H(\mathbf{p}) = H^*(\mathbf{p}). \quad (\text{A.36})$$

We apply condition (A.36) to Hamiltonian (A.29). Since, the Pauli matrix σ_y changes sign under the complex conjugation, the condition (A.36) constrains

$$h_y(\mathbf{p}) = 0 \quad (\text{A.37})$$

in agreement with Eq. (A.32). As discussed in , h_y component of vector \mathbf{h} vanishes, i.e. $h_y(\mathbf{p}) = 0$. The electronic energy spectrum of Hamiltonian (A.29) has two bands

$$\begin{aligned} \varepsilon_{\pm}(\mathbf{p}) &= h_0(\mathbf{p}) \pm |\mathbf{h}(\mathbf{p})| = \\ &= h_0(\mathbf{p}) \pm \sqrt{h_x^2(\mathbf{p}) + h_z^2(\mathbf{p})}. \end{aligned} \quad (\text{A.38})$$

Notice that, the equation $\mathbf{h}(\mathbf{p}) = [h_x(\mathbf{p}), 0, h_y(\mathbf{p})] = 0$ generally has non-trivial solutions in two-dimensions $\mathbf{p} = (p_x, p_y)$, since the number of equations matches the numbers of variables. Therefore, we expect to find accidental degeneracies $\varepsilon_-(\mathbf{p}) = \varepsilon_+(\mathbf{p})$ in the energy spectrum (A.38), where $\mathbf{h}(\mathbf{p}) = 0$. We plot spectrum (A.38) for various values of χ in Fig. A.2. Indeed, we observe that the degeneracies consistently occur as we change parameter χ from 0 to π . For $\chi = 0$, the two bands touch parabolically in the center of the Brillouin zone, as shown in Fig. A.38(a). With a slight increase of the parameter to $\chi = \pi/3$, we observe the appearance of the four

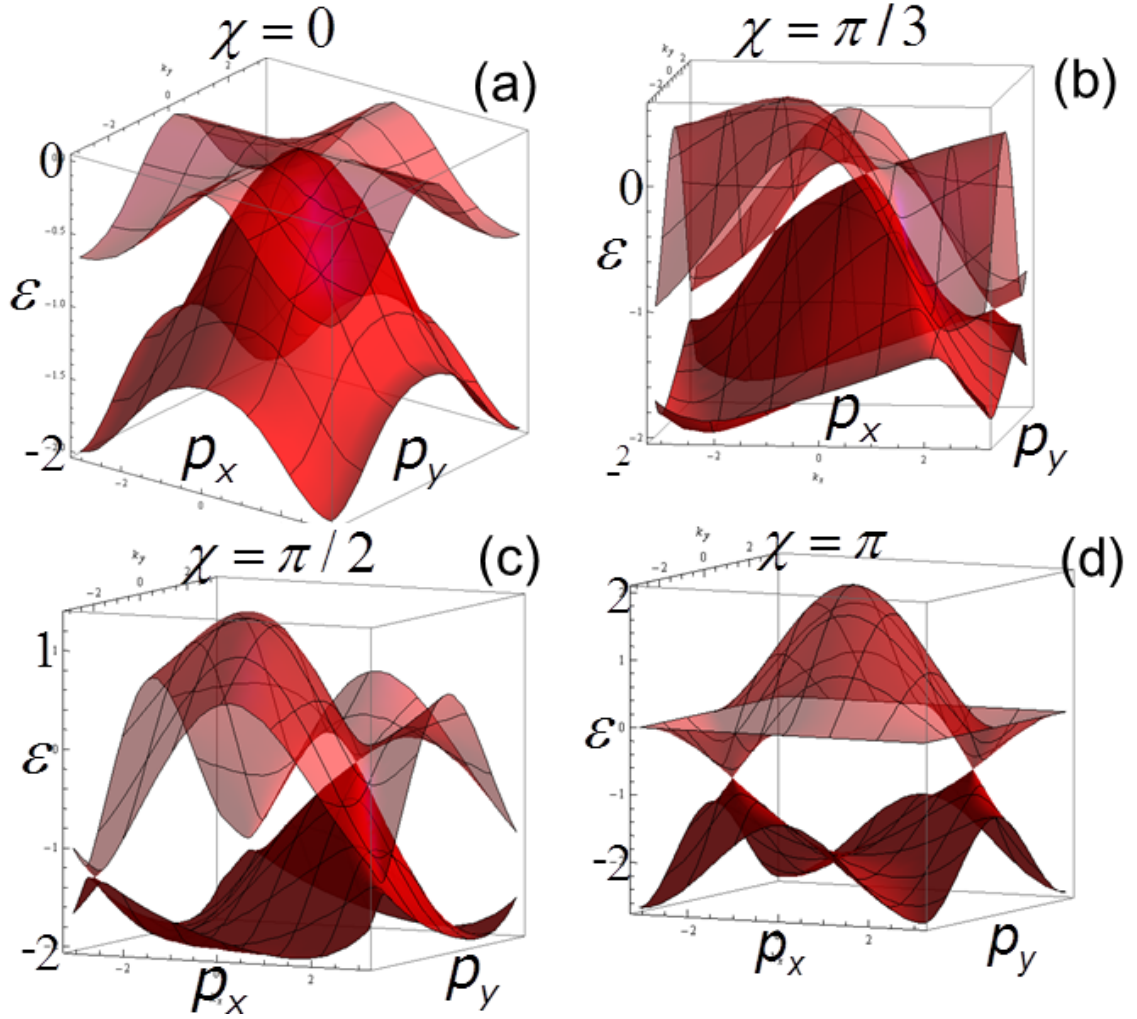


Figure A.2: Electronic spectrum (A.38) of Hamiltonian (A.29) for various values of parameter χ : (a) $\chi = 0$, (b) $\chi = \pi/3$, (c) $\chi = \pi/2$, (d) $\chi = \pi$. The energy axis ε is given in eV, whereas the momenta run across the Brillouin zone, i.e. $|p_x| < \pi$ and $|p_y| < \pi$.

degeneracies. As shown in Fig. A.2(b), the degeneracies have a shape of deformed and tilted Dirac cones. For $\chi = \pi/2$, the energy spectrum contains two Dirac cones offset in energy and momentum, as shown in Fig. A.2(c). For $\chi = \pi$, the Dirac cones have the same energy as shown in Fig. A.2(d).

List of publications

Current thesis is based on the following publications

1. **S. S. Pershoguba**, K. Kechedzhi, and V. M. Yakovenko, “Proposed Chiral Texture of the Magnetic Moments of Unit-Cell Loop Currents in the Pseudogap Phase of Cuprate Superconductors”, *Phys. Rev. Lett.* **111**, 047005 (2013)
2. Yu. I. Latyshev, A. P. Orlov, P. Monceau, D. Vignolles, **S. S. Pershoguba**, V. M. Yakovenko, “Interlayer tunneling spectroscopy of graphite at high magnetic field oriented parallel to the layers”, *Eur. Phys. J. Special Topics* **222**, 1257 (2013).
3. **S. S. Pershoguba** and V. M. Yakovenko, “Spin-polarized tunneling current through a thin film of topological insulator in a parallel magnetic field”, *Phys. Rev. B* **86**, 165404 (2012).
4. **S. S. Pershoguba** and V. M. Yakovenko, “Shockley model description of surface states in topological insulators”, *Phys. Rev. B.* **86**, 075304 (2012).
5. **S. S. Pershoguba** and V. M. Yakovenko, “Energy spectrum of graphene multilayers in a parallel magnetic field”, *Phys. Rev. B* **82**, 205408 (2010).

Other publications by Sergii Pershoguba

1. **S. S. Pershoguba**, Yu. V. Skrypnyk, and V. M. Loktev, “Numerical simulation evidence of spectrum rearrangement in impure graphene” *Phys. Rev. B* **80**, 214201 (2009).
2. L. A. Falkovsky and **S. S. Pershoguba**, “Optical far-infrared properties of a graphene monolayer and multilayer”, *Phys. Rev. B* **76**, 153410 (2007).

List of presentations

Talks

1. I gave 6 contributed talks at APS March meetings during 2010-2014.
2. “Kerr effect as an evidence of the Chiral order in the Pseudogap phase of cuprates.”, Winter School “Topological Phases of Condensed Matter.”, Tallahassee FL, January (2014).
3. “Evidence of the chiral order in the pseudogap phase of cuprates.”, CNAM student seminar, College Park MD, February (2013).
4. “Thin films of topological insulators in a parallel or tilted magnetic field.”, CMTTC symposium, College Park MD, October (2012).
5. “Spin-polarized tunneling current through a thin film of a topological insulator.”, Victor Galitski’s group meeting, College Park MD, March (2012).
6. “Thin films of topological insulators in a parallel or tilted magnetic field.”, CNAM student seminar, College Park MD, November (2011); **Award for the “Best CNAM student presentation”**.
7. “Shockley-model description of the edge states in topological insulators.”, CMTTC symposium, College Park MD, September (2011).
8. “Why to pursue a career in science?”, **talk at a high school**, Cherkassy, Ukraine, May (2011).
9. “Effect of the tilted magnetic field on the topological insulator spectrum.”, CNAM student seminar, College Park MD, March (2011).
10. “Numerical simulation evidence of spectrum rearrangement in impure graphene.”, Michael Fuhrer’s group meeting, College Park MD, July (2010).

Posters

1. “Spectrum of graphene multilayer in a parallel magnetic field.”, Summer school, Rio de Janeiro, Brazil, July (2010).
2. “Spectrum of graphene multilayer in a parallel magnetic field.”, Graphene Week at UMD, College Park MD, April (2010).

Attendance of conferences and schools

1. “Topological Phases of Condensed Matter.”, Winter School, Tallahassee FL, January (2014).
2. “An open world of physics: A celebration of Sankar Das Sarma’s research career on his 60th birthday”, Conference, College Park MD, USA, March (2013).
3. “Materials & Mechanisms of Superconductivity”, Conference, Washington DC, USA, August (2012).
4. “The Princeton Summer School for Condensed Matter Physics”, Summer School, Princeton NJ, USA, July (2012).
5. “Computational Approaches for Electronic/Magnetic Materials”, Winter School, Tallahassee FL, USA, January (2012).
6. “New Phenomena in Quantum Matter”, Summer school, Rio de Janeiro, Brazil, July (2010).

Bibliography

- [1] W. Shockley, Phys. Rev. **56**, 317 (1939).
- [2] W. P. Su, J. R. Schrieffer, and A. J. Heeger, Phys. Rev. Lett. **42**, 1698 (1979).
- [3] S. G. Davison and M. Steslicka, *Basic Theory of Surface States* (Oxford University Press, 1996).
- [4] R. Jackiw and C. Rebbi, Phys. Rev. D **13**, 3398 (1976).
- [5] B. A. Volkov and O. A. Pankratov, JETP Lett. **42**, 178 (1985).
- [6] O. A. Pankratov, JETP Lett. **45**, 103 (1987).
- [7] A. J. Heeger, Rev. Mod. Phys. **73**, 681 (2001).
- [8] P. Delplace, D. Ullmo, and G. Montambaux, Phys. Rev. B **84**, 195452 (2011).
- [9] R. S. K. Mong and V. Shivamoggi, Phys. Rev. B **83**, 125109 (2011).
- [10] A. Y. Kitaev, Phys. Usp. **44**, 131 (2001).
- [11] M. Wimmer, A. R. Akhmerov, M. V. Medvedyeva, J. Tworzydło, and C. W. J. Beenakker, Phys. Rev. Lett. **105**, 046803 (2010).
- [12] K. S. Novoselov *et al.*, Science **306**, 666 (2004).
- [13] K. S. Novoselov *et al.*, Nature **438**, 197 (2005).
- [14] A. H. Castro Neto, F. Guinea, N. M. R. Peres, K. S. Novoselov, and A. K. Geim, Rev. Mod. Phys. **81**, 109 (2009).
- [15] S. Das Sarma, S. Adam, E. H. Hwang, and E. Rossi, Rev. Mod. Phys. **83**, 407 (2011).
- [16] L. A. Falkovsky and S. S. Pershoguba, Phys. Rev. B **76**, 153410 (2007).

- [17] V. P. Gusynin and S. G. Sharapov, Phys. Rev. Lett. **95**, 146801 (2005).
- [18] C. L. Kane and E. J. Mele, Phys. Rev. Lett. **95**, 226801 (2005).
- [19] C. L. Kane and E. J. Mele, Phys. Rev. Lett. **95**, 146802 (2005).
- [20] L. Fu, C. L. Kane, and E. J. Mele, Phys. Rev. Lett. **98**, 106803 (2007).
- [21] L. Fu and C. L. Kane, Phys. Rev. B **76**, 045302 (2007).
- [22] B. A. Bernevig, T. L. Hughes, and S. C. Zhang, Science **314**, 1757 (2006).
- [23] B. A. Bernevig and S. C. Zhang, Phys. Rev. Lett. **96**, 106802 (2006).
- [24] X. L. Qi, T. L. Hughes, and S. C. Zhang, Phys. Rev. B **78**, 195424 (2008).
- [25] J. E. Moore and L. Balents, Phys Rev B. **75**, 121306 (2007).
- [26] R. Roy, Phys. Rev. B **79**, 195322 (2009).
- [27] R. Roy, Phys. Rev. B **79**, 195321 (2009).
- [28] A. P. Schnyder, S. Ryu, A. Furusaki, and A. W. W. Ludwig, Phys. Rev. B **78**, 195125 (2008).
- [29] S. Ryu, A. P. Schnyder, A. Furusaki, and A. W. W. Ludwig, New J. Phys. **12**, 065010 (2010).
- [30] M. Z. Hasan and C. L. Kane, Rev. Mod. Phys. **82**, 3045 (2010).
- [31] M. Z. Hasan and J. E. Moore, Annu. Rev. Cond. Mat. Phys. **2**, 55 (2011).
- [32] X. L. Qi and S. C. Zhang, Rev. Mod. Phys. **83**, 1057 (2011).
- [33] F. D. M. Haldane, Phys. Rev. Lett. **61**, 2015 (1988).
- [34] C.-Z. Chang *et al.*, Science **340**, 167 (2013).
- [35] A. K. Geim and I. V. Grigorieva, Nature **499**, 419 (2013).
- [36] M. Yankowitz *et al.*, Nat. Phys. **8**, 382 (2012).
- [37] A. A. Burkov and L. Balents, Phys. Rev. Lett. **107**, 127205 (2011).
- [38] T. Das and A. V. Balatsky, Nat. Commun. **4**, 1972 (2013).
- [39] Y. Zhang, Y.-W. Tan, H. L. Stormer, and P. Kim, Nature **438**, 201 (2005).
- [40] M. L. Sadowski, G. Martinez, M. Potemski, C. Berger, and W. A. de Heer, Phys. Rev. Lett. **97**, 266405 (2006).
- [41] Z. Jiang *et al.*, Phys. Rev. Lett. **98**, 197403 (2007).

- [42] E. McCann and V. I. Fal'ko, Phys. Rev. Lett. **96**, 086805 (2006).
- [43] M. Inoue, J. Phys. Soc. Jpn. **17**, 808 (1962).
- [44] G. Dresselhaus, Phys. Rev. B **10**, 3602 (1974).
- [45] G. Li and E. Y. Andrei, Nat. Phys. **3**, 653 (2007).
- [46] P. Plochocka *et al.*, Phys. Rev. Lett. **100**, 087401 (2008).
- [47] M. Orlita *et al.*, Phys. Rev. Lett. **102**, 166401 (2009).
- [48] K.-C. Chuang, A. M. R. Baker, and R. J. Nicholas, Phys. Rev. B **80**, 161410 (2009).
- [49] A. F. Garcia-Flores, H. Terashita, E. Granado, and Y. Kopelevich, Phys. Rev. B **79**, 113105 (2009).
- [50] M. Koshino and T. Ando, Phys. Rev. B **77**, 115313 (2008).
- [51] F. Guinea, A. H. C. Neto, and N. M. R. Peres, Phys. Rev. B **73**, 245426 (2006).
- [52] Y. Kopelevich, P. Esquinazi, J. H. S. Torres, and S. Moehlecke, J. Low Temp. Phys. **119**, 691 (2000).
- [53] H. Kempa, H. C. Semmelhack, P. Esquinazi, and Y. Kopelevich, Solid State Commun. **125**, 1 (2003).
- [54] Y. Iye, M. Baxendale, and V. Z. Mordkovich, J. Phys. Soc. Jpn. **63**, 1643 (1994).
- [55] M. V. Kartsovnik, P. A. Kononovich, V. N. Laukhin, and I. F. Schegolev, JETP Lett. **48**, 541 (1988).
- [56] K. Kajita *et al.*, Solid State Commun. **70**, 1189 (1989).
- [57] V. M. Yakovenko and B. K. Cooper, Physica E **34**, 128 (2006).
- [58] E. H. Hwang and S. Das Sarma, Phys. Rev. B **80**, 075417 (2009).
- [59] V. M. Yakovenko, Europhys. Lett. **3**, 1041 (1987).
- [60] V. M. Yakovenko and H. S. Goan, Phys. Rev. B **58**, 8002 (1998).
- [61] A. G. Lebed, Phys. Rev. Lett. **95**, 247003 (2005).
- [62] J. M. B. Lopes dos Santos, N. M. R. Peres, and A. H. Castro Neto, Phys. Rev. Lett. **99**, 256802 (2007).
- [63] G. Li *et al.*, Nat. Phys. **6**, 109 (2009).

- [64] L. Onsager, *Philos. Mag.* **43**, 1006 (1952).
- [65] V. M. Krasnov, A. E. Kovalev, A. Yurgens, and D. Winkler, *Phys. Rev. Lett.* **86**, 2657 (2001).
- [66] Y. I. Latyshev, P. Monceau, S. Brazovskii, A. P. Orlov, and T. Fournier, *Phys. Rev. Lett.* **95**, 266402 (2005).
- [67] Y. I. Latyshev, A. P. Orlov, D. Vignolles, W. Escoffier, and P. Monceau, *Physica B* **407**, 1885 (2012).
- [68] S. K. Lyo *et al.*, *Physica E* **34**, 425 (2006).
- [69] L. Britnell *et al.*, *Nano Lett.* **12**, 1707 (2012).
- [70] L. Britnell *et al.*, *Nat. Commun.* **4**, 1794 (2013).
- [71] A. P. Orlov, Y. I. Latyshev, A. M. Smolovich, and P. Monceau, *JETP Lett.* **84**, 89 (2006).
- [72] P. Hosur, S. Ryu, and A. Vishwanath, *Phys. Rev. B* **81**, 045120 (2010).
- [73] H. Zhang *et al.*, *Nat. Phys.* **5**, 438 (2009).
- [74] C. X. Liu *et al.*, *Phys. Rev. B* **82**, 045122 (2010).
- [75] J. Linder, T. Yokoyama, and A. Sudbo, *Phys. Rev. B* **80**, 205401 (2009).
- [76] W. Y. Shan, H. Z. Lu, and S. Q. Shen, *New J. Phys.* **12**, 043048 (2010).
- [77] H. Z. Lu, W. Y. Shan, W. Yao, Q. Niu, and S. Q. Shen, *Phys. Rev. B* **81**, 115407 (2010).
- [78] T. T. Heikkila and G. E. Volovik, *JETP Lett.* **93**, 59 (2011).
- [79] T. T. Heikkila, N. B. Kopnin, and G. E. Volovik, *JETP Lett.* **94**, 233 (2011).
- [80] S. Ryu and Y. Hatsugai, *Phys. Rev. Lett.* **89**, 077002 (2002).
- [81] V. Gurarie, *Phys. Rev. B* **83**, 085426 (2011).
- [82] B. Béri, *Phys. Rev. B* **81**, 134515 (2010).
- [83] A. P. Schnyder and S. Ryu, *Phys. Rev. B* **84**, 060504 (2011).
- [84] T. Hsieh and L. Fu, *Phys. Rev. Lett.* **108**, 107005 (2012).
- [85] D. Hsieh *et al.*, *Nature* **460**, 1101 (2009).
- [86] J. G. Analytis *et al.*, *Phys. Rev. B* **81**, 205407 (2010).
- [87] Y. S. Hor *et al.*, *Phys. Rev. Lett.* **104**, 057001 (2010).

- [88] J. C. Y. Teo, L. Fu, and C. L. Kane, Phys. Rev. B **78**, 045426 (2008).
- [89] D. P. Arovas and F. Guinea, Phys. Rev. B **78**, 245416 (2008).
- [90] A. Bermudez, L. Amico, and M. A. Martin-Delgado, New J. Phys. **12**, 055014 (2010).
- [91] M. Creutz and I. Horvath, Phys. Rev. D **50**, 2297 (1994).
- [92] A. Bermudez, D. Patane, L. Amico, and M. A. Martin-Delgado, Phys. Rev. Lett. **102**, 135702 (2009).
- [93] C. Beenakker, Annu. Rev. Con. Mat. Phys. **4**, 113 (2013).
- [94] D. Hsieh *et al.*, Science **323**, 919 (2009).
- [95] Y. L. Chen *et al.*, Science **325**, 178 (2009).
- [96] Y. H. Wang *et al.*, Phys. Rev. Lett. **107**, 207602 (2011).
- [97] N. P. Butch *et al.*, Phys. Rev. B **81**, 241301 (2010).
- [98] D. Kim *et al.*, Nat. Phys. **8**, 460 (2012).
- [99] S. Cho *et al.*, Nano Lett. **11**, 1925 (2011).
- [100] C. Brüne *et al.*, Phys. Rev. Lett. **106**, 126803 (2011).
- [101] B. Seradjeh, J. E. Moore, and M. Franz, Phys. Rev. Lett. **103**, 066402 (2009).
- [102] Y. Zhang *et al.*, Nat. Phys. **6**, 584 (2010).
- [103] A. A. Taskin, S. Sasaki, K. Segawa, and Y. Ando, Phys. Rev. Lett. **109**, 066803 (2012).
- [104] M. Y. Choi, Y. H. Hyun, and Y. Kim, Phys. Rev. B **84**, 195437 (2011).
- [105] A. A. Zyuzin, M. D. Hook, and A. A. Burkov, Phys. Rev. B **83**, 245428 (2011).
- [106] J. P. Eisenstein, T. J. Gramila, L. N. Pfeiffer, and K. W. West, Phys. Rev. B **44**, 6511 (1991).
- [107] H. B. Zhang *et al.*, Adv. Mater. **24**, 132 (2012).
- [108] P. Moses and R. H. McKenzie, Phys. Rev. B **60**, 7998 (1999).
- [109] Y. Ran, Y. Zhang, and A. Vishwanath, Nat. Phys. **5**, 298 (2009).
- [110] J. C. Y. Teo and C. L. Kane, Phys. Rev. B **82**, 115120 (2010).
- [111] H. Beidenkopf *et al.*, Nat. Phys. **7**, 939 (2011).
- [112] M. R. Norman, D. Pines, and C. Kallin, Adv. Phys. **54**, 715 (2005).

- [113] J. Xia *et al.*, Phys. Rev. Lett. **100**, 127002 (2008).
- [114] A. Kapitulnik, J. Xia, E. Schemm, and A. Palevski, New J. Phys. **11**, 055060 (2009).
- [115] R.-H. He *et al.*, Science **331**, 1579 (2011).
- [116] H. Karapetyan *et al.*, Phys. Rev. Lett. **109**, 147001 (2012).
- [117] S. Tewari, C. Zhang, V. M. Yakovenko, and S. D. Sarma, Phys. Rev. Lett. **100**, 217004 (2008).
- [118] P. Kotetes and G. Varelogiannis, Europhys. Lett. **84**, 37012 (2008).
- [119] K. Sun and E. Fradkin, Phys. Rev. B **78**, 245122 (2008).
- [120] Y. He, J. Moore, and C. M. Varma, Phys. Rev. B **85**, 155106 (2012).
- [121] Y. Lubashevsky, L. Pan, T. Kirzhner, G. Koren, and N. P. Armitage, Phys. Rev. Lett. **112**, 147001 (2014).
- [122] P. Hosur, A. Kapitulnik, S. A. Kivelson, J. Orenstein, and S. Raghu, Phys. Rev. B **87**, 115116 (2013).
- [123] L. D. Landau, E. M. Lifshitz, and L. P. Pitaevskii, *Electrodynamics of Continuous Media* (Pergamon Press, Oxford, 1984).
- [124] J. Orenstein and J. E. Moore, Phys. Rev. B **87**, 165110 (2013).
- [125] S. Chakravarty, Phys. Rev. B **89**, 087101 (2014).
- [126] M. R. Norman, Phys. Rev. B **87**, 180506 (2013).
- [127] M. E. Simon and C. M. Varma, Phys. Rev. Lett. **89**, 247003 (2002).
- [128] V. Aji, Y. He, and C. M. Varma, Phys. Rev. B **87**, 174518 (2013).
- [129] A. Shekhter and C. M. Varma, Phys. Rev. B **80**, 214501 (2009).
- [130] Y. B. Zel'dovich, J. Exp. Theor. Phys. **33**, 1531 (1957).
- [131] V. M. Dubovik and V. V. Tugushev, Phys. Rep. **187**, 145 (1990).
- [132] V. Aji, A. Shekhter, and C. M. Varma, Phys. Rev. B **81**, 064515 (2010).
- [133] Y. He and C. M. Varma, Phys. Rev. B **85**, 155102 (2012).
- [134] R. Viswanathan, J. A. Zasadinski, and D. K. Schwartz, Nature **368**, 440 (1994).
- [135] J. Ishioka *et al.*, Phys. Rev. Lett. **105**, 176401 (2010).

- [136] A. R. Bungay, Y. P. Svirko, and N. I. Zheludev, *Phys. Rev. B* **47**, 1173 (1993).
- [137] I. E. Dzyaloshinskii, *J. Exp. Theor. Phys.* **37**, 331 (1959).
- [138] B. Fauqué *et al.*, *Phys. Rev. Lett.* **96**, 197001 (2006).
- [139] Y. Li *et al.*, *Nature* **455**, 372 (2008).
- [140] S. D. Almeida-Didry *et al.*, *Phys. Rev. B* **86**, 020504 (2012).
- [141] S. Strässle, B. Graneli, M. Mali, J. Roos, and H. Keller, *Phys. Rev. Lett.* **106**, 097003 (2011).
- [142] P. Bourges and Y. Sidis, *C. R. Physique* **12**, 461 (2011).
- [143] C. Weber, A. Lauchli, F. Mila, and T. Giamarchi, *Phys. Rev. Lett.* **102**, 017005 (2009).
- [144] J. Chang *et al.*, *Nat. Phys.* **8**, 871 (2012).
- [145] G. Ghiringhelli *et al.*, *Science* **337**, 821 (2012).
- [146] A. J. Achkar *et al.*, *Phys. Rev. Lett.* **109**, 167001 (2012).
- [147] Y. Kohsaka *et al.*, *Science* **315**, 1380 (2007).
- [148] J. Orenstein, *Phys. Rev. Lett.* **107**, 067002 (2011).
- [149] E. Arrigoni, M. Aichhorn, M. Daghofer, and W. Hanke, *New J. Phys.* **11**, 055066 (2009).